Colección de Estudios de Física 76

Magnetic properties of mesoscopic-size materials: From molecules to nanowires

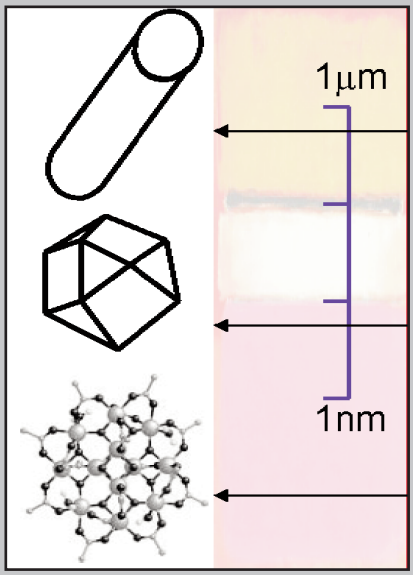

Román López Ruiz

Magnetic properties of mesoscopic-size materials: From molecules to nanowires

Colección de Estudios de Física
Vol. 76

Esta colección recoge las tesis presentadas en el Departamento de Física de la Materia Condensada de la Universidad de Zaragoza desde su constitución en 1987.

Colección de Estudios de Física Vol. 76

Magnetic properties of mesoscopic-size materials: From molecules to nanowires

Román López Ruiz

Prensas Universitarias de Zaragoza

FICHA CATALOGRÁFICA

LÓPEZ RUIZ, Román
Magnetic properties of mesoscopic-size materials : from molecules to nanowires / Román López Ruiz. — Zaragoza : Prensas Universitarias de Zaragoza, 2009
XI, 167 p. ; 24 cm. — (Colección de Estudios de Física ; 76)
Tesis-Universidad de Zaragoza
ISBN 978-84-92521-78-4
1. Nanoestructuras–Propiedades magnéticas–Tesis doctorales. I. Universidad de Zaragoza. II. Título. III. Serie: Colección de Estudios de Física (Prensas Universitarias de Zaragoza) ; 76
539.24:537.622(043.2))

1.ª edición, 2009

Prensas Universitarias de Zaragoza. Edificio de Ciencias Geológicas, c/ Pedro Cerbuna, 12, 50009 Zaragoza, España. Tel.: 976 761 330. Fax: 976 761 063
puz@unizar.es http://puz.unizar.es

Impreso en España
Imprime: Servicio de Publicaciones. Universidad de Zaragoza
D.L.: Z-417/2009

A mi madre

Contents

1

Introduction

1.1 What is mesoscopic?

Mesoscopic is the region of size in between the microscopic and macroscopic worlds. It is usually nanometric. A way to understand the level of reduction associated with this region is thinking that 1 nm equals to 10 Å. Since Ångström is directly associated with the dimension of the atomic bond, we are *very near the atomic level.* The miniaturization of the materials to this mesoscopic level gives rise to interesting changes on their physical properties, which sometimes become very different from the typical bulk behavior. For instance, molecules, nanoparticles or nanowires offer the opportunity [Shi 1996] to study how the magnetic properties vary as we travel around the mesoscopic level. It is also possible to study the transition from quantum to classical behavior [Zurek 2003][Leggett 2002].

The capacity of manipulation of material structures in this range opens also new possibilities for engineering or materials science. We are developing a new fascinating field: *Nanotechnology.* Nowadays, applications in composites like paints, sun creams or advanced-application polymers are giving rise to a large number of patents. Also, the reduced-dimension materials are of importance for the increase of memory storage density in computing and electronic devices [White 2000]. In medicine, ultra-sensitive sensors of tumor markers based on silicon nanowires, which provide a qualitative jump in the diagnostic field, are under development [Patolsky 2006b].

1.2 Molecules, particles and nanowires

As in mesoscopic level we are very near the atomic scale, the first magnetic complex body we can investigate are molecules. The next level of complexity are the nanometric particles. If we denote this *nanoparticle* as a fragment of a bulk magnetic metal, we can investigate not only zero dimensional (0D) spheres, but also nanowires, where the size is restricted only in 2 of the 3 dimensions of space.

As a consequence of the restriction in size, these magnetic materials behave as single domain structures [Kittel 1949]. An special crystal environment, surface effects or shape can induce an anisotropy which gives rise to a double well landscape for the potential energy (see Fig. 1.1). The magnetization will be stable unless some perturbation forces it to overcome the energy barrier U_0 imposed by the anisotropy. As the magnetic moment of the particle, responsible of the magnetization, is coupled to the environmental degrees of freedom of the host material, like phonons, nuclear spins, or conducting electrons, the behavior of the magnetic particles tends to be dominated by *thermal* fluctuations. Consequently, both molecular or nanoparticle materials show essentially a *super*paramagnetic behavior characteristic of nanoscale solids or clusters with a large net spin ($S \sim 10^1$–10^4). Here, the prefix *Super* refers to the large spin values, as compared with conventional paramagnetic salts.

For molecules and very small nanoparticles, quantum fluctuations can play a very important role, by e.g. enabling the spin to tunnel across the anisotropy barrier. In the following, I introduce the mesoscopic materials that have been subject of study at the present thesis work in order of increasing size.

Mn_{12}: A prototypical Single-Molecule Magnet

The most studied single-molecule magnet is Mn_{12}. It can be seen as a metal-organic cluster containing a magnetic core of 12 Manganese atoms surrounded by a shell of organic ligands which isolates the clusters from one another [Blundell 2004]. They form molecular crystals in which all molecules are nearly identical. For Mn_{12} single-molecule magnets, the spin reversal may also occur by tunnelling whenever the magnetic field brings into resonance quantum states located at the sides of the anisotropy barrier [Friedman 1996][Thomas 1996][Hernandez 1996].

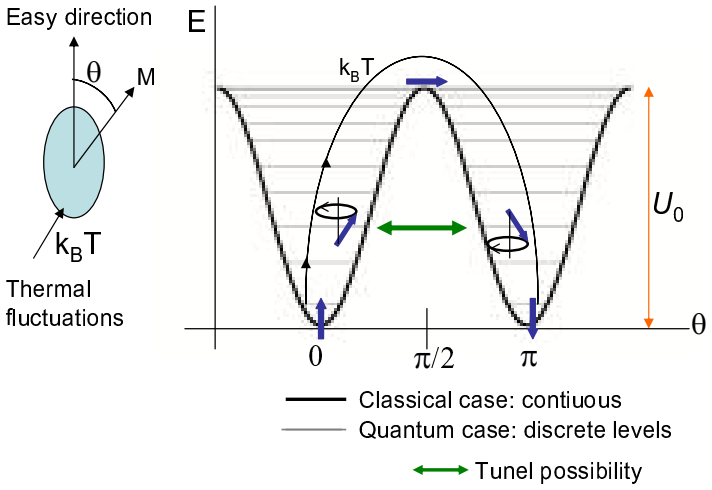

Fig. 1.1. Energy of a single-domain particle with uniaxial anisotropy as a function of the angle between the magnetization and the easy direction. U_0 is the energy barrier when $H = 0$.

Via a *bottom-up* route, single crystals of these Mn_{12} cores can be obtained [Lis 1980][Takeda 2002]. They provide a model system to carry out the study of quantum phenomena at the mesoscopic scale. In this thesis we have studied the nonlinear magnetic response of such single-molecule magnets. Indeed, the magnetic susceptibility may be expanded as a field-dependent polynomial function whose linear and quadratic coefficients give the χ_2 and χ_3 nonlinear susceptibilities respectively. We have found a quantum contribution to χ_3, which confers to this quantity a extreme sensibility to detecting quantum phenomena; χ_3 allows us to get information about coherence and enables studying the quantum-to-classical transition [Garcia-Palacios 2000b]. While single-molecule magnets such as Mn_{12} constitute a model system to study quantum mechanics at a mesoscopic level, magnetic nanoparticles provide a natural classical limit.

Cobalt nanoparticles: bigger than a molecule

Travelling towards the macroscopic world, the next level of complexity corresponds to magnetic nanoparticles. Following a top-down strategy, such as the sputtering technique, an almost hexagonal array of cobalt nanoparticles can be fabricated [Babonneau 2000][Maurice 1999].

Nanoparticles are polyhedra [Kitakami 1997], which are embedded in an easy controllable medium.

The conventional magnetic characterization shows that nanoparticles of cobalt obey the mentioned superparamagnetic behavior and show an anisotropy larger than the bulk material due to surface affects [Luis 2002b][Luis 2006]. In other words, the anisotropy is determined by the special conditions of the external atoms, thus providing a system in which the anisotropy can be controlled by the environment. We can monitor this by the measurement of χ_3 [Garcia-Palacios 2000a]. Furthermore, these arrays are suitable materials in order to extend the study of χ_3 to systems with classical spin dynamics.

However, in a collection of structures, also the interactions play an important role. In a well-defined array, the magnetic clusters are coupled via dipolar interactions and magnetic properties can be affected.

The role of the interactions: Magnetic memory effects

The magnetic behavior of interacting magnetic nanoparticles, such as the arrays of cobalt clusters described above, go beyond the picture of magnetic relaxation of individual spins [Luis 2002c]. They are complex systems where dipolar interactions might give rise to magnetic memory effects, such as "aging", similar to those encountered in spin-glasses [Jonsson 2004][Sasaki 2005][Chen 2005][Petracic 2006]. We can study these phenomena by ZFC protocols, i.e. by measuring the susceptibility after cooling the sample in a zero magnetic field. When a pause is made at a temperature below the superparamagnetic blocking temperature, a "hole" is burnt in the susceptibility measurement with respect to a non-paused Zero Field Cooled (ZFC) [Mathieu 2001a]. From the size of the hole it is possible, in a clever way, to estimate the magnetic correlations established between neighboring spins induced by the inter-particle interactions. Because of the good control over microstructural parameters [Maurice 1999], our study represents a qualitative jump towards a better fundamental knowledge of nanoparticle systems showing slow magnetic dynamics, and to the question of whether a true "super spin-glass" phase occurs in these systems.

Nanowires: we can play with dimensions

Also in this miniature level it is possible to play with one-dimensional structures. A nanowire provides a natural limit to the superparamagnetism, in a sense that its volume is large enough not to be influenced by thermal fluctuations and does not show a superparamagnetic

behavior [Morrish 1965]. Furthermore, the shape anisotropy makes every nanowire to behave as a single magnetic domain irrespective of their length.

We have prepared a set-up to fabricate arrays of metallic nanowires via a *bottom-up* template-assisted method, i.e. electroplating a magnetic metal as nickel into a porous anodized aluminium foil. For a general overview of the nanowires synthesis see [He 2003]. The nanowire organization and the single domain behavior of each wire confers to these arrays a large technological interest since such systems could maximize the storage magnetic information [White 2000]. It is important to extract some information about the nature of the magnetization reversal process (along the wire) [Frei 1957][Aharoni 2000][Jacobs 1955] and about the influence that extrinsic effects, like mechanical stresses, might have on their magnetic properties.

The number of publications dealing with the study of nanowires is increasing exponentially. Far from the topics studied in this thesis, let us explain by means of a visual example the huge importance of these nano-elements. Is the bionic man possible? The question can be answered if an external device such as a mechanical arm can receive the electrical signal of the brain surface that controls the person's mobility. Far from the possibility to live in a "Matrix movie" world, nanowires will perform a very important task by interacting with neurons, as the possibility to connect axons and dendrites is already proved [Patolsky 2006a]. The nanoworld that exists inside our cells could then interact in the future with the nanotechnological world created by us. Maybe in the 22nd century?

1.3 Outline

PhD thesis is divided in six chapters. The reader will be first introduced (**Chapter 1**) to a general vision about nanometer-size materials treated in this thesis, and the mesoscopic level.

The synthesis and magnetic properties of Nickel nanowires are studied in **Chapter 2**. The shape-controlled nanowires electrochemical synthesis is described. Later, a magnetic study of wires with different aspect ratios is carried out. Basic anisotropy and magnetization reversal mechanisms are investigated. Also a study of the size dependence on the Curie temperature is performed.

The next chapter, (**Chapter 3**) is dedicated to Mn_{12} single-molecule magnets. A non-linear magnetic susceptibility of Mn_{12} acetate and Mn_{12} benzoate study performed on single-crystals and powder is reported. Our goals are to study the spin tunnelling and anisotropy effects on the cited quantity. Determination of environment effect, or "damping" on the spin dynamics lets us estimate a bound for the decoherence time due to the coupling to the phonon bath.

In **Chapters 4 and 5**, different magnetic properties of sputtered cobalt nanoparticles are investigated. **Chapter 4** is dedicated to a nonlinear magnetic susceptibility research (similar to that on Mn_{12}). The goal is to study the possibility of spin reversal by tunnelling and the effect of surrounding media on the anisotropy and the spin dynamics. In **Chapter 5**, magnetic memory effects in cobalt nanoparticles are investigated in order to determine its collective magnetic behavior.

Finally, the main conclusions of this thesis are summarized in **Chapter 6**.

2

Electrochemical synthesis and characterization of nanowires

2.1 Electrochemical synthesis of metallic nanowires

Nanowires are materials of potential interest for applications as ultra high-density magnetic recording media [White 2000], electronic devices [Capasso 1990], optics [Agarwal 2006] or biological chip-based sensors [Patolsky 2006b]. In particular, ordered arrays of ferromagnetic nanowires offer the opportunity to study magnetism at the mesoscopic level [Paulus 1999]. A relatively simple procedure to fabricate arrays of metallic nanowires is to start from nanoporous materials and fill the pores with a ferromagnetic metal by electrochemical methods. Track-etched polymer membranes, anodized aluminium films or silica are commonly used as templates. The advantage of the porous anodized aluminium films, besides low fabrication cost, is that under certain conditions the 2D lattice formed by the nanopores can be very regular with ordered domains of hundreds of nanometers [Keller 1952].

2.1.1 Porous alumina membrane as a template: Introduction

Nanowires are produced by a template-assisted method [He 2003]. Thus, quality and shape parameters of a 2D array of nanowires are directly conditioned by the morphology of the alumina template. In this section, synthesis protocols and microscopy characterization of Al_2O_3 porous alumina membranes (PAM) are described.

Alumina Al_2O_3 is known as a porous material for more than 50 years [Keller 1952]. Several studies have been made in order to understand the growing processes and to control it [Thompson 1978] [Ebihara 1982]. Although disordered porous alumina membranes are

used as host for magnetic materials [Huysmans 1988], a breakthrough occurred when Masuda [Masuda 1995] proved, in 1995, the possibility of arranging regular nanoporous structures in alumina under certain conditions.

Alumina structure

The synthetic method consists of a thermally controlled current-forced aluminium oxidation (anodization), usually applying a constant voltage, in acid solutions. The morphology of alumina anodic films mainly depends on the anodization solution (electrolyte) [Despic 1983]. Neutral solutions form barrier films, but in acidic conditions, when $pH < 2.6$, alumina becomes partially soluble and the oxide film forms a porous structure. In this pH range and certain experimental conditions [Nielsch 2002], the porous membrane shows a typical honeycomb structure (Fig. 2.1). It consists of a packed array of hexagonal columns, each containing a pore at its center and separated from the aluminium metal by a scalloped spherical oxide barrier layer.

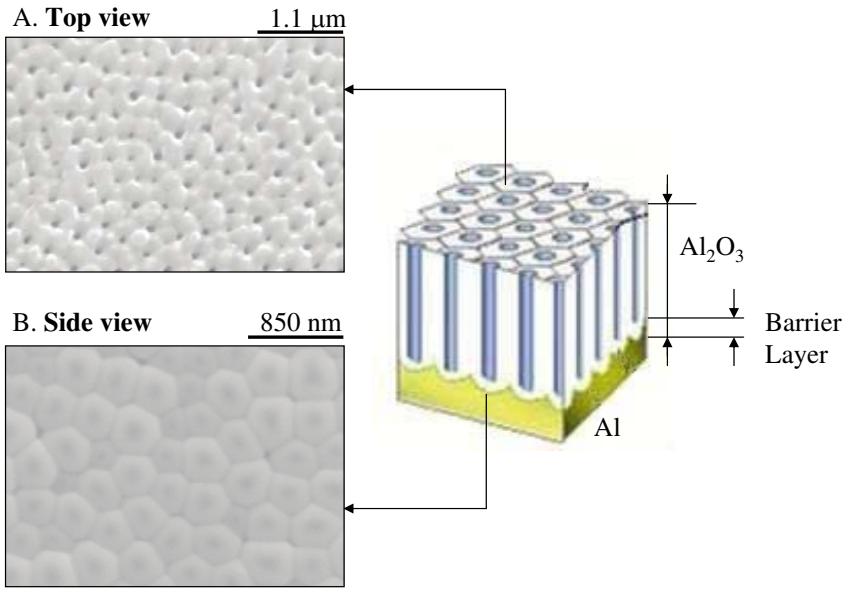

Fig. 2.1. Schematic drawing of the nanoporous alumina structure as obtained as a result of anodic oxidation. Example of the top view (A) and the side view after aluminium removal (B) of a sample synthesized at 160 V during 2 hours in H_3PO_4 1%.

The arrangement and shape of alumina pores are determined by the applied voltage, temperature, and type and concentration of the electrolyte.

Film growth

Film growth involves some self-assembly processes and different stages in the alumina film growth which can be monitored by e.g. maintaining a constant voltage regime and registering current versus time evolution (Fig. 2.2).

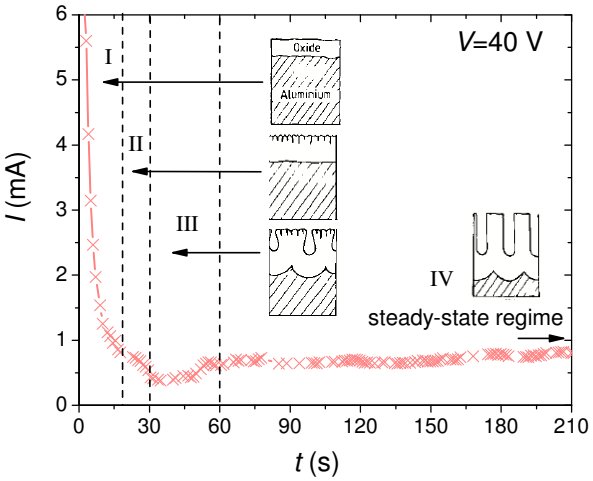

Fig. 2.2. Current-time curve during the anodization under a potentiostatic regime V=40 V in a $H_2C_2O_4$ electrolyte. Different growth regions are indicated.

Initially, a non-porous barrier film is formed. The alumina is an electronic insulator but a good ionic conductor. At the beginning of the insulator film formation, the electronic resistance increases drastically and therefore the current drops rapidly (zone I). After a certain time, the film develops cracks and the pores begin to nucleate at random positions (zone II). This results in an increase of the electrode surface and thus the current goes up (zone III) until it reaches a constant value ascribed to the steady-state growth of pores (zone IV).

When the ternary system Electrolite/Oxide/Metal arrives at the steady-state regime, the width of the alumina barrier layer remains constant during the pore growth. The reaction rate depends on the rates of ionic migration through the alumina barrier: Al^{+3} towards

the solution and O^{-2}, OH^{-} towards aluminium substrate. Under this regime, the field-assisted alumina solution at the electrolyte-oxide interface (bottom of the pore) is compensated by oxide growth at the oxide-metal interface [Parkhutik 1992]. The pores grow downwards arranging themselves in a regular array. The process is not yet fully understood and other explanations have been proposed [O'sullivan 1970][MacDonald 1989]. [Jessensky 1998] suggest that the mechanical stress, which is associated with the expansion of the aluminium during oxide formation is the cause of repulsive forces between neighboring pores during the oxidation process and lead to self-organized formation of hexagonal pore arrays. The origin of this mechanical stress lies in the fact that the atomic density of aluminium in alumina is twice lower than in metallic aluminium. Since the oxidation is located in the entire Oxide/Metal simultaneously, the only way to expand the material is along the vertical direction.

Self-ordering definition

By convention, a porous array is considered to be self-organized when, in a radial distribution, the hexagonal order extends beyond the shell of the nearest neighbors. With this definition, nowadays it's possible to fabricate self-ordered porous alumina with cell diameters (D_{cell}) 50, 60, 100, 420, 500 and 600 nm [Nielsch 2002]. Alumina templates with cell diameter between 100 and 420 nm might be achieved via a previous pre-patterning methods such as imprint lithography [Choi 2003] or e-beam lithography. The conditions to arrange a well-defined self-ordering structure in "soft" (low-voltage conditions) regime are well-known and are summarized in table 2.1.

Electrolyte (mol/l)	V(V)	$D_{\text{cell}}(nm)$	T °C	Literature
H_2SO_4 (2)	18.7	50	1	[Jessensky 1998]
H_2SO_4 (0.3)	25	60	0	[Masuda 1997]
$H_2C_2O_4$ (0.3)	40	100	1	[Masuda 1995]
H_3PO_4 (1)	160	420	10	[Li 1998]
H_3PO_4 (0.1)	195	500	10	[Masuda 1998]
$C_6H_8O_7$ (2)	240	600	20	[Ono 2004]

Table 2.1. Self-ordering conditions ($C_6H_8O_7$ denotes the citric acid).

2.1.2 Experimental details

As mentioned above, the arrangement and shape of alumina pores are determined by the applied anodization voltage, the temperature, and the pH of the solution, which is determined by the type of electrolyte and concentration. The experimental protocol used by us to fabricate porous alumina membranes consisted of: (1) Aluminium surface preparation, (2) Double-step anodization and electroplating, (3) Post-treatment: layer etching, which are described in detail in what follows.

(1) Aluminium surface preparation

Because electrolytic reactions take part at the electrodic surface, proceedings to adequately prepare the aluminium surface are obviously very important.

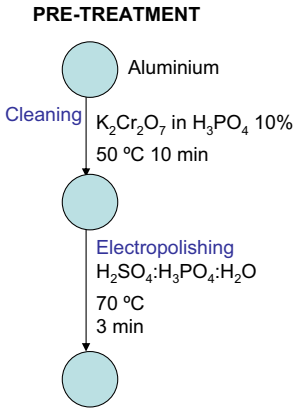

Fig. 2.3. Synthesis flow of nanowires: Aluminium pre-treatment.

Aluminium normal potential is -1.66 V. In contact with air, aluminium surface is spontaneously covered by a thin film of aluminium oxide. Typical oxide layer thicknesses lie between 3 and 10 nm. Furthermore, other impurities like metallic oxides and grease can be present at the surface. In order to clean the aluminium surface, the aluminium film is immersed in 0.08 M ($K_2Cr_2O_4$) chromic acid solution in 1 M phosphoric acid at 50 °C during 10 minutes.

To reduce the surface roughness, the aluminium substrate is electropolished in a 4:4:2 in weight H_2SO_4:H_3PO_4:H_2O solution at 70 °C during 3 minutes. The anode is connected to aluminium and the cathode is connected to a lead bar. Under these conditions, aluminium is dissolved. As is well known, because of the lightning rod effect, the electric field becomes larger at sharp surfaces, thus also the rate of solution process is strongest at the "hills". As a result, a polished and stripped substrate is achieved. The process reduces the number of possible breakdown centers due to local over-heating during the anodization and eliminates the surface metallic centers coming from the industrial aluminium foil production, preventing important interferences in magnetic measurements.

(2) Double-step anodization and electroplating

The aluminium disc is then mounted on an anodically connected copper plate and a selected region is exposed to the acidic electrolyte in a thermally isolated electrolytic cell specially-designed by us (Fig. 2.4). A lead bar is used as a cathode. The circular area of aluminium exposed to the electrolyte was 0.4 mm^2. The potentiostatic regime is maintained by a programmable Chroma power source and a Nestlab 120 external recirculated refrigerator is used to maintain the temperature stable.

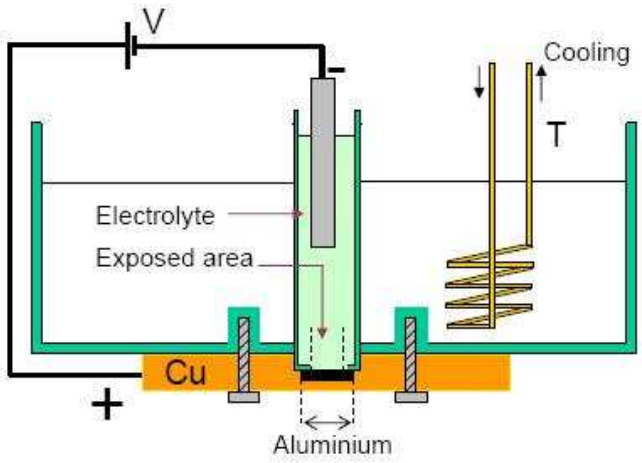

Fig. 2.4. Schematic drawing of electrolytic cell.

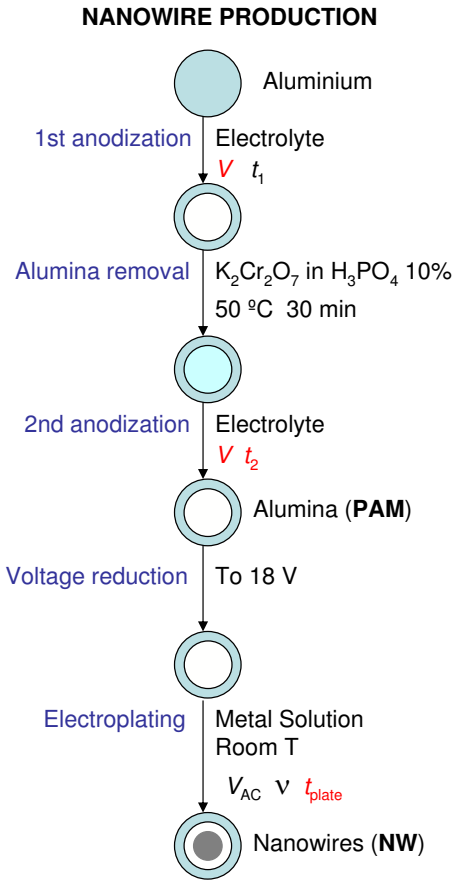

Fig. 2.5. Synthesis flow of nanowires: Anodization and electroplating process. In red are the parameters we will vary in order to achieve a determined wire morphology.

The double-step anodization protocol and further template electroplating is presented in Fig. 2.5. In order to achieve a better pore ordering, two consecutive anodizations were done. During the first anodization of the aluminium electropolished surface, pores nucleate and begin to grow at random positions. With time, self organization is arranged at the bottom. After this first anodization, the alumina layer is removed with a mixture of chromic acid and phosphoric acid solution at 50 °C during 30 minutes. A pattern structure of "hills and valleys" is marked in the aluminium (Fig. 2.6). In a second anodization, for the same applied voltage, the aluminium is therefore already pre-patterned

and the nucleation takes place preferentially in the valleys, improving the distance homogeneity and the arrangement of the pores.

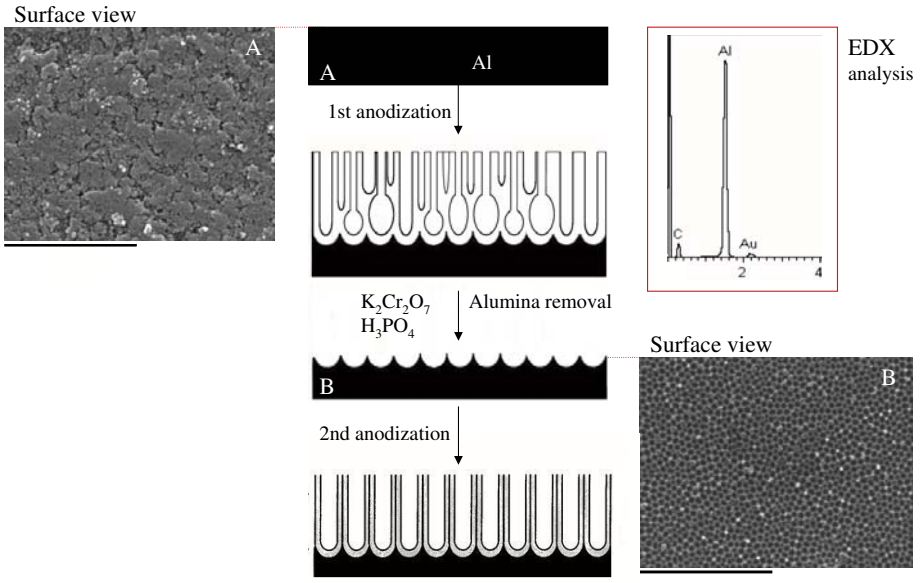

Fig. 2.6. Surface view SEM images A.- Aluminium substrate after electropolishing; B.- Aluminium template after first anodization and alumina removal. Sample B was placed 30 minutes in $K_2Cr_2O_7$ after anodization applying 60 V during 120 minutes. Scale bar length is 3 μm. EDX spectrum is analogous for samples A and B.

Thus, the aluminium is anodized twice, controlling essential parameters: time (t_1 and t_2 refers to the first and second anodization times respectively), voltage (V), temperature (T) and acid concentration. The anodization parameters employed by us, were chosen to fit the best "soft" regime conditions table 2.1. They are summarized in the table 2.2. Note the difference in the H_3PO_4 concentration depending on the applied voltage. Above 140 V, the concentration acid must be reduced, otherwise a strong fizzing and a large emission of heat is observed due to a strong reaction rate. In other words, we change to a "hard" regime or "burning" [Lee 2006] that gives rise to a new phenomenology that goes beyond the investigation of this thesis.

Electrolyte	Voltage range (V)	Temperature (°C)
H_2SO_4 (1M)	0-40	0
$H_2C_2O_4$ (0.3M)	40-80	0
H_3PO_4 (4%)	80-140	10
H_3PO_4 (1%)	140-180	10

Table 2.2. Table of general anodization conditions.

Electroplating

AC electroplating has been used to fill alumina templates at room temperature. During this process, the aluminium/alumina specimen is used as cathode whereas a lead sheet is used as anode. The schematic set-up is illustrated in Fig. 2.7. The electrolyte consists of a sulphate salt containing the metal that we want to deposit into the pores, namely a solution of $NiSO_4 \cdot 7H_2O$ (50 g/l), H_3BO_3 (25 g/l), glycerin (20 g/l). During the process, metallic cations reduce and deposit inside the pores and nanowires grow from bottom to top.

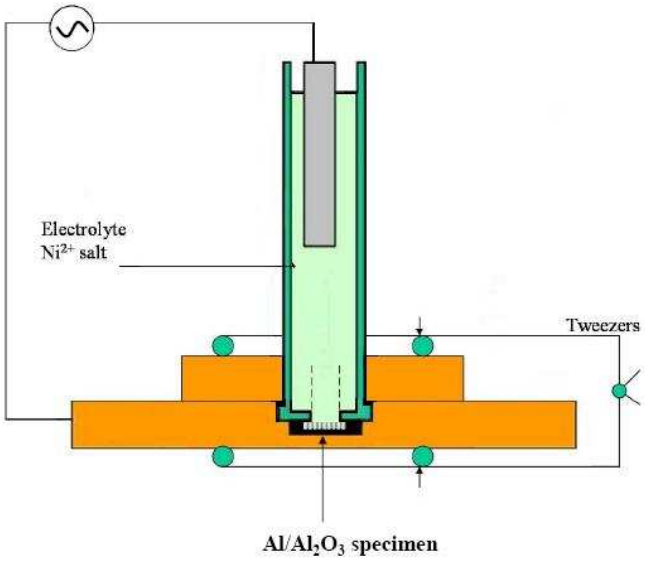

Fig. 2.7. Schematic drawing of electrodeposition cell.

Prior to any filling, voltage reduction is necessary in order to reduce the insulator barrier layer thickness [Furneaux 1989]. The anodization voltage is reduced gradually in 5% steps until it approximately reaches 18 V. Every step is performed when the current fluxing through the sample reaches a nearly constant steady-state value (usually every three minutes). At the bottom of the pores, a tree-root pattern of pores develops and the insulator barrier becomes thin enough to allow electronic transport during the electroplating. Although the voltage reduction makes this barrier thinner, DC electroplating becomes very unstable and an uniform filling cannot be achieved. AC electric current is used to avoid the electrical charging of the structure. In our case, electrodeposition was carried out always at V_{AC} =15 V and a frequency ν =100 Hz [Friedman 2007]. Different plating times (t_{plate}) were used in order to monitor the wire's growth.

(3) Post-treatment: layer etching

The specific-side anodization results in an Al_2O_3 film supported by the aluminium substrate. Aluminium layer can be removed with a 0.2 M $CuCl_2$ in HCl 7 M solution. After the aluminium removal, an Al_2O_3 barrier layer at the bottom of the pores is present. By chemical etching with a 10% (in weight) H_3PO_4 solution, pores can be opened.

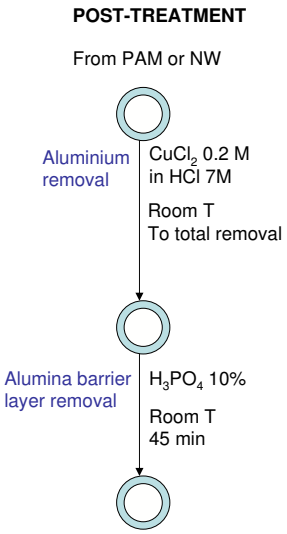

Fig. 2.8. Synthesis flow of nanowires: Sample post-treatment.

2.1.3 Characterization of porous alumina membranes

We have determined the influence in our templates that different parameters, such as anodization voltage, time and temperature have on the morphology of the membranes and the sizes of the pores. Sizes were measured by scanning electron microscopy. Measurements were carried out using Jeol JMS-6400 Scanning Microscope (SEM) and Hitachi H4300FE Field Emission Scanning Microscope (FE-SEM). The image analysis was performed by a software called *ADimag* developed at the *Servicio Digital de Imagen* of the University of Zaragoza.

Reproducibility study

Nine samples synthesized under analogous conditions were studied in order to evaluate the reproducibility of the preparation method. In particular, the conditions of our study were V=60 V, in oxalic acid 0.3 M, T=0 °C, t_1=30 min for the first anodization and t_2=120 min for the second one. After the sample was prepared, the aluminium layer was removed from the bottom and the cell diameter was evaluated graphically (See an example in Fig. 2.1). The analysis of the SEM images reveals a gaussian distribution of cell's diameters. Results are shown in Fig. 2.9.

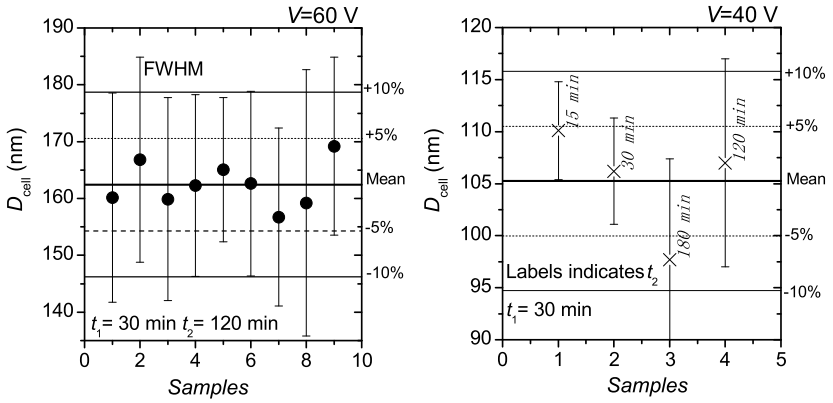

Fig. 2.9. LEFT: reproducibility study at: V=60 V, $H_2C_2O_4$ 0.3 M, T=0 °C, t_1=30 min t_2=120 min. RIGHT: cell diameter variation when t_2 is varied for samples produced at V=40 V and t_1=30 min.

This reproducibility study shows that the mean cell diameter has a confidence better than 5% and FWHM rarely exceeds 10%. Fixing anodization voltage (V=40 V), the t_2 variation reveals that anodization time has no influence in cell or pore diameter.

Voltage influence: Controlling the pore size

To study the influence of the anodization voltage on the size of the pores, the temperature and the electrolyte were fixed, as is detailed in table 2.2. Also, the first anodization was carried out during t_1=30 min, the second anodization time was t_2=120 min. During both anodization processes the voltage was kept constant. Voltage reduction steps were not applied.

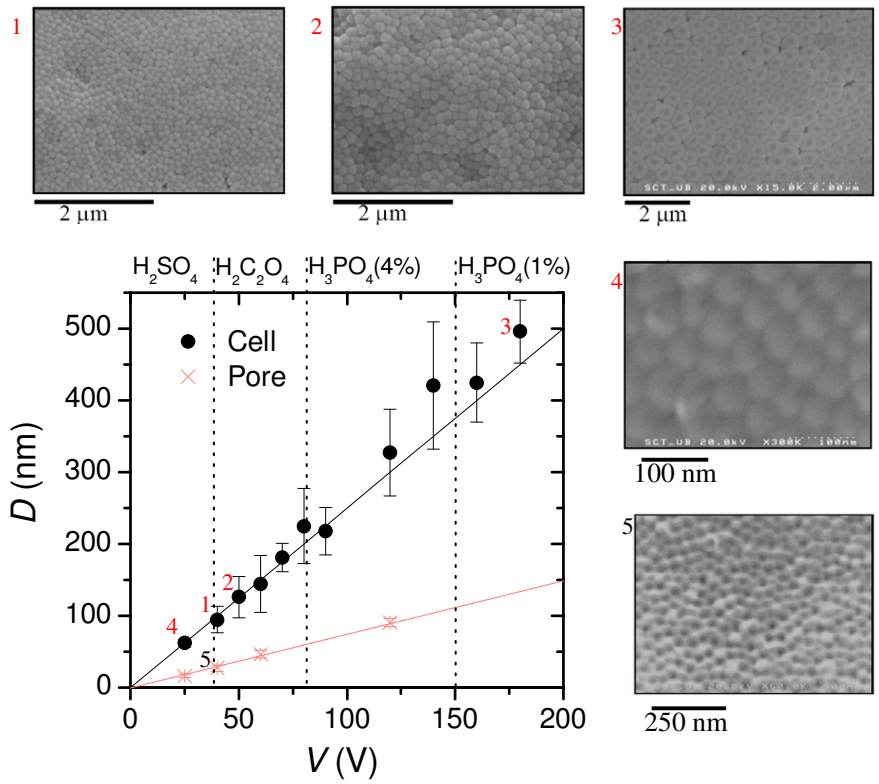

Fig. 2.10. Voltage influence on cell and pore diameter. Temperatures and electrolytes used are described in table 2.2 and marked in superior scale. For all samples: t_1=30 min and t_2=120 min. Black and red lines are linear fits for cell and pore diameters respectively.

Samples produced at different voltages were studied by SEM or FE-SEM. Top view images give access to measuring the pore diameter, while the bottom views, after aluminium removal, reveal the cell diameter. In good agreement with the results reported in the literature [Ebihara 1983][Pavlovic 1986][Czokan 1980][Thompson 1983], a linear relation is found between cell diameter and voltage. As it's well known:

$$D_{\text{cell}} = KV, \qquad K = 2.5 \text{ nm/V} \tag{2.1}$$

In Fig. 2.10 this linear dependence is represented by a solid line. Furthermore, the average diameter of the pores varies also linearly with voltage, following:

$$D = kV, \qquad k = 0.748 \text{ nm/V} \tag{2.2}$$

The k value differs from $k = 1.2$ nm/V determined in [Paulus 1999]. The porosity value of the samples is about 9%. Within the experimental uncertainties, porosity values are in agreement with the 10% predicted in [Nielsch 2002] for perfectly arranged pore arrays.

Anodization time influence: Controlling the pore length

To achieve this study, samples were prepared for a cross-section view: They were embedded in a resin and polished mechanically. An illustrative example, showing the sharp interface between the aluminium substrate and the alumina layer is shown in Fig. 2.11. Different chemical compositions are distinguished and corroborated by EDX analysis as it can be seen in Fig. 2.11. To analyze the influence that the second anodization time has on the thickness of the alumina layer length, all samples were prepared at $V = 40$ V in a 0.3 M $H_2C_2O_4$ solution. The temperature was kept at $T = 0$ °C and the first anodization time was t_1=30 min.

As we can see in Fig. 2.11 thickness increases linearly with anodization time. The low error bars reveal that the alumina layer grows very uniformly over the surface of aluminium. The Pores posses a big aspect ratio (L/D) with a length of microns and some nanometers in diameter. Furthermore, as we have shown in the last two sections, we can control both length and diameter independently.

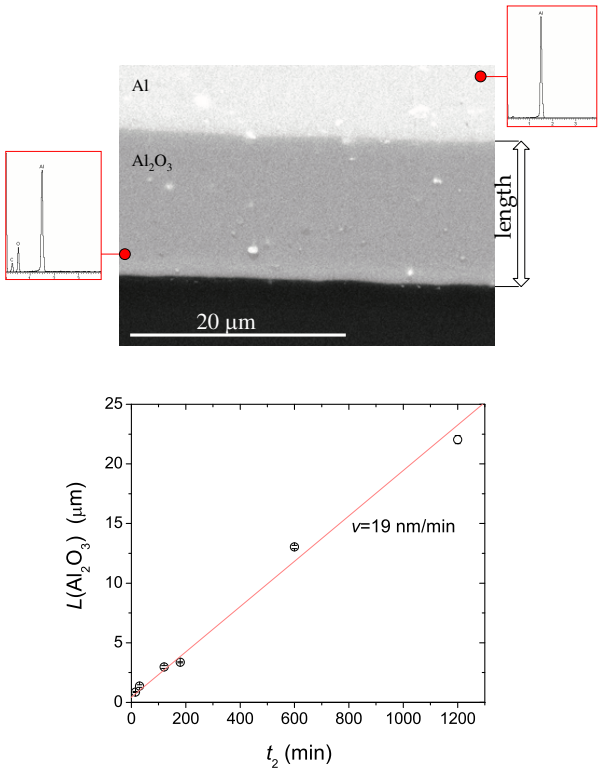

Fig. 2.11. UP: Cross-section view of sample with t_2=600 min. Chemical composition of layers was corroborated by EDX. DOWN: Influence of second anodization time (t_2) in alumina length $L(Al_2O_3)$. All samples: V=40 V, $H_2C_2O_4$ 0.3 M, T = 0 °C, t_1=30 min.

2.1.4 Nanowires characterization

Influence of the plating time: controlling the wire's length

The filling fraction of the pores can be calibrated by the plating time (t_{plate}). To this end, porous alumina membranes (details in Fig. 2.12) were filled employing AC voltage with an amplitude of 15 V and a frequency of 100 Hz for plating time between 1 and 10 minutes. As we can see in Fig. 2.12(A) when the plating time equals or exceeds 10 minutes, some wires grow completely and Nickel begins to cover the pores. Therefore, since the magnetic signal of the continuous nickel overlayer formed in this way can easily shadow the contribution from the wires, it is better not to fill the templates for times longer than 10 minutes.

For $t_{\text{plate}} < 10$ min, we have measured the length distribution of the wires using SEM images (see Fig. 2.12). The filling fraction distribution is ascribed to solution nickel depletion inside the pores.

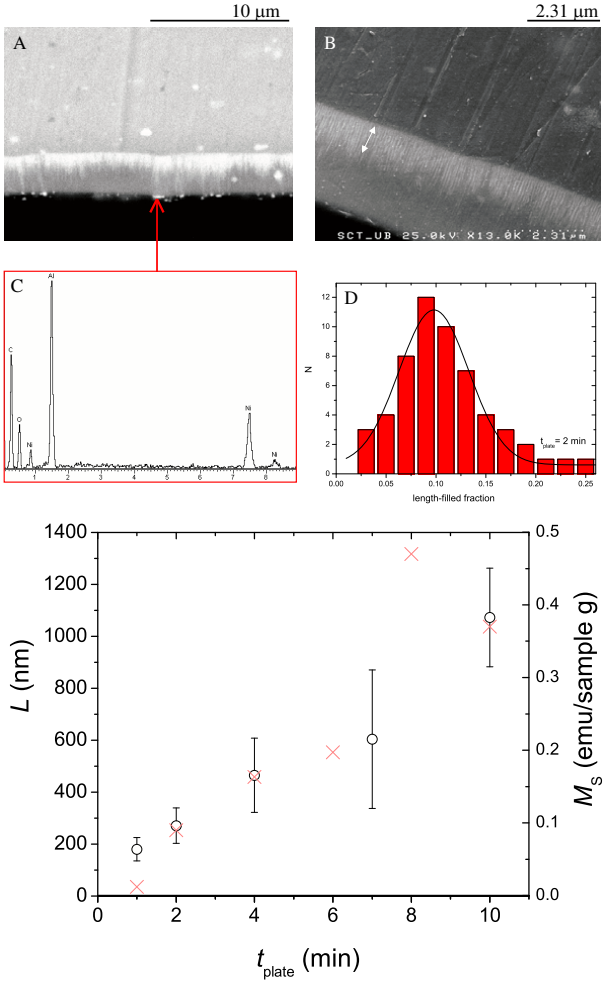

Fig. 2.12. UP: (A) SEM cross-section view of a 10 minutes plated sample on a PAM synthesized with these parameters: V=40 V, t_1=30 min, t_2=120 min. (B) FE-SEM amplification. Gaussian fit represents the pore fraction which is filled in a sample filled during 2 minutes. (C) The EDX spectrum show Nickel presence at the pore ending. (D) Gaussian distribution of lengths for a sample plated during 2 nim. DOWN: Circles: variation of the wire's length with the plating time. PAM parameters: V = 40 V, t_1=30 min and t_2=120 min. The plating voltage had an amplitude of V_{AC}=15 V and a frequency ν=100 Hz. Crosses: Saturation magnetization values obtained from hysteresis loops.

Fig. 2.12 shows the average wire length as a function of plating time (t_{plate}). Again, we see that the length increases linearly until a saturation occurs for $t_{\text{plate}} \geqq 10$ min. This dependence enables us to control the aspect ratio of the nanowires. From magnetization hysteresis loops measured at room temperature, we can study the saturation magnetization of these samples. As measurements are scaled by the total sample mass (essentially aluminium mass), saturation magnetization gives us a direct measurement of the nickel amount. The saturation magnetization and the wire length show both a qualitatively similar variation with the plating time evidencing that filling time increases the amount of nickel and directly determines the wire's length.

2.2 Magnetic properties of Nickel nanowires

In the previous sections, we have seen how the length L and diameter D of the nanowires can be varied within wide margins in a controlled way. In what follows, our interest on these materials is to investigate the dependence of their magnetic properties on their size and aspect ratio $m = L/D$.

To achieve this study, hysteresis loops and magnetization isotherms were measured on nickel nanowire samples with different morphological parameters and over a wide temperature region from 4 K up to the Curie temperature. The variation of the magnetization with the temperature does not show any superparamagnetic blocking, which confers to the material prospects for application in data storage devices.

We can consider the nanowires as single-domain particles due to shape anisotropy. According to the model of Stoner and Wohlfarth, their magnetic properties can be correlated with the wires' morphology. Therefore, the first goal is to study the hysteretic behavior on nanowires with different aspect ratios in order to determine the crossover between the 0D particle behavior to 1D elongated particles or nanowire behavior.

For particles above the aspect ratio that determines the "wire-like" behavior, room temperature coercive field values show discrepancies with those predicted by the Stoner-Wohlfarth model. The variation of the coercive field with the wire diameter is related to the predominance of magnetization reversal modes different from the "rotation in unison" that assumes the Stoner-Wohlfarth model. Different micromag-

netic theories will be introduced in order to determine the magnetization reversal mode inside the wires.

Also extrinsic effects can play a role on the magnetism of our nanowire matrices. The different thermal expansion coefficients of aluminium, alumina and nickel may induce magnetoelastic effects that affect the temperature-dependent magnetic properties. We want to elucidate the influence of the alumina/aluminium matrix on these effects (an issue sometimes controversial). To achieve this goal, we shall extend the coercivity study to a range of temperatures not covered until present.

Curie temperature will also be studied in nanowires with different aspect ratios. The variation of the Curie temperature can be ascribed to a finite-size effect and the values, also, can be influenced by the mentioned template-induced thermal stresses.

Samples and magnetic measurements

Samples of nanowires were prepared from double-step anodized porous alumina membranes (PAM) prepared by the protocol described in the last section. A double-step anodization was in all cases performed with anodization times of 30 minutes and 2 hours. The anodization voltages were 25, 40, 60, 100, 110 and 140 V, which correspond (see Fig. 2.11) to pore diameters of 17, 27, 46, 75, 85 and 105 nm respectively. For templates fabricated with these conditions and filled in a nickel solution electrolyte during 10 minutes, the diameter influence on the magnetic behavior can be investigated. These samples enable us to study experimentally how the change in diameter modifies the magnetic properties. In addition, we also prepared samples of nanowires with fixed diameter (D=27 nm and D=46 nm) and increasing aspect ratio m.

The presence of a macroscopic amount of nanowires in one membrane enables us the application of macroscopic measurements techniques. So, standard magnetization measurements were done using a commercial *Quantum Design* SQUID. A commercial SQUID equipped with an oven was used in order to study the magnetic properties above room temperature (up to 800 K) and to determine from these the variation of the Curie temperature with the wire's size. The alignment of the nanowires enables also to study directional dependences. Measurements were done with the applied magnetic field oriented approximately parallel or perpendicular to the wires' axis.

Magnetic hysteresis: shape anisotropy

As we can see in Fig. 2.13, the hysteresis loops measured at room temperature with the applied field parallel and perpendicular to the wires' axes are markedly different. The parallel loop shows larger values of remanence and coercivity.

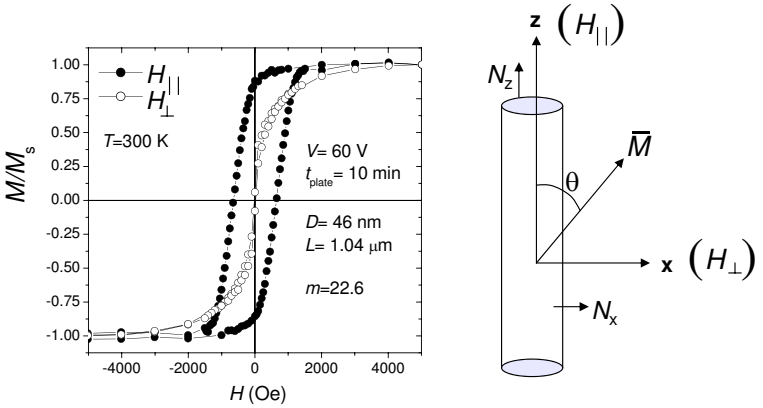

Fig. 2.13. LEFT: hysteresis loops for parallel and perpendicular applied fields measured at 300 K on a sample synthesized at V=60 V (D=46 nm), t_1=30 min and t_2=120 min. The plating time was 10 minutes. RIGHT: coordinates scheme of a wire.

The results can be explained by the existence of an effective uniaxial anisotropy that favors the magnetization along the wire axis. This *shape anisotropy* plays an important role and dominates over the magnetocrystalline anisotropy. At zero field, the energy minima correspond with the magnetization pointing along the wire axis, at $\theta = 0$ or $\theta = \pi$. Energy is maximum for $\theta = \pi/2$, i.e. perpendicular to wire axis, and shows a bistable structure with an energy barrier $U = K_{\rm sh}V$ to be overcome for the magnetization reversal. $K_{\rm sh}$ is the shape anisotropy constant and V the volume of the particle. Thus, the magnetization M points along the wire axis, in positive ($\theta = 0$) or negative ($\theta = \pi$) direction, depending on the immediate history.

In a first approximation, for particles with constrained dimensions, the magnetic response can be interpreted using the Stoner-Wohlfarth model [Morrish 1965]. This model predicts the hysteretic behavior at zero temperature of *single-domain* ferromagnetic particles with uniax-

ial anisotropy. In the model, it is assumed that the particle is uniformly magnetized and the magnetization $|M|$ remains constant. In-field magnetization component M_{H} is measured and the magnetic field necessary to avoid the barrier energy is defined as the anisotropy field H_{A}. An applied magnetic field acts merely rotating the magnetization M an angle θ with respect to the anisotropy axis. At the microscopic scale, the model is consistent with a collection of spins that reverse *in unison*.

When the field is applied parallel to the nanowires (i.e. $\theta = 0$) the parallel magnetization direction is stabilized, while the antiparallel becomes a metastable state. At T=0 K, no thermal energy is available for the spin particle to jump the barrier, thus no spin reversal occurs until the anisotropy field H_{A} is reached. As a consequence, the hysteresis loop shows a perfectly squared shape (squareness $M_{\mathrm{r}}/M_{\mathrm{s}}$ =1) and coercive field $H_{\mathrm{c}} = H_{\mathrm{A}}$. For elongated nanoparticles, as prolates, when shape anisotropy is dominant, the anisotropy field reads:

$$H_{\mathrm{A}} = (N_{\mathrm{x}} - N_{\mathrm{z}})M_{\mathrm{s}} \tag{2.3}$$

where N_{x} and N_{z} are the demagnetization factors perpendicular and parallel to long prolate axis respectively.

In the opposite extreme, when a magnetic field is applied perpendicular to wires' axis, the two stable magnetization states ($\theta = 0$ and $\theta = \pi$) becomes unstable, stabilizing two new minima with no energy change. New minima correspond with a magnetization slightly deviated from parallel and antiparallel positions. As no energy change is needed to achieve these new minima, a change in magnetic field leads to a reversible rotation of magnetization and therefore no hysteresis is present and the remanent M_{H} tends to zero in good agreement with our experimental data.

Hysteresis as a function of wire's aspect ratio: from nanoparticles to the infinite cylinder limit

In the previous section we conclude that the hysteretic behavior is due to shape anisotropy. Thus, the shape of the hysteresis loops is expected to vary for samples with different aspect ratios. Wires with reduced aspect ratio (near the unity) will show a weak shape anisotropy. The coercivity will then be dominated by the intrinsic magnetocrystalline anisotropy, with axes oriented at random. By contrast, when the aspect ratio increases, the shape anisotropy will dominate and the easy axes will be oriented along the wires' axes. This difference in the magnetic texture, should lead to a different hysteretic behavior according to the Stoner-Wohlfarth model. In the present study, hysteresis loops for samples synthesized with different plating times were measured at room temperature.

The remanent magnetization M_{r} must be obtained as the remanence at zero *local field*. Therefore, the hysteresis loops must be corrected from the *macroscopic demagnetization effect* of the samples, to obtain the intrinsic properties of the material [Samwel 1992][Paulus 1999]. Consider a sample positively saturated $M = +M_{\mathrm{s}}$, when a magnetic field is applied in the opposite direction, interactions give rise to a local field inside the sample H_{in} lower (is more negative) than the applied field H_{appl} and, therefore, the magnetization reversal starts before the anisotropy field is achieved. The demagnetization field H_{d} opposed to the applied field is defined as follows:

$$H_{\mathrm{in}} = H_{\mathrm{appl}} - H_{\mathrm{d}}, \qquad H_{\mathrm{d}} = NM \tag{2.4}$$

where N is the demagnetization factor of the macroscopic sample. This demagnetization field is generated as a consequence of the interaction of the sample magnetization with its own field and it is opposed to the applied one. In our samples, M is the average sample magnetization and N is the demagnetization factor of the dish region containing the wires. Demagnetization field has a linear dependence with the magnetization M. We assume the intrinsic hysteresis loop to have an infinitely large slope near H_{in}. By fitting the linear $M(H)$ dependence near the coercive field, $M = (1/N)H$, N is obtained and the magnetic field can be corrected (An example of this procedure is shown in Fig. 2.14). Note that this correction affects the remanence value, but not the coercive field.

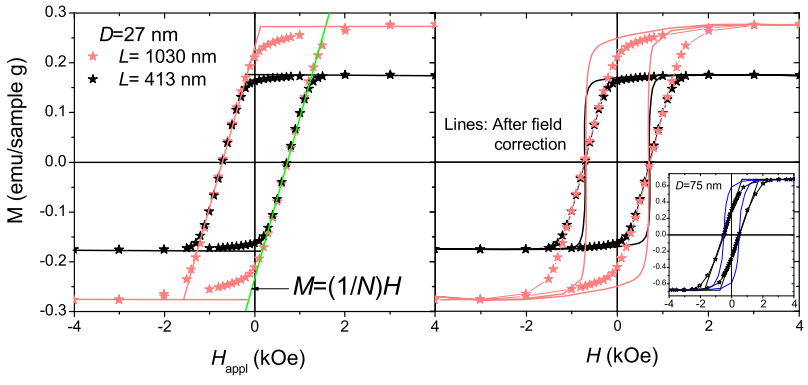

Fig. 2.14. LEFT: hysteresis loops for samples with different aspect ratios. Lines defines the linear fit to compensate the demagnetization field effect. A fit example is shown in a green line. RIGHT: corrected hysteresis loops of left samples. Note no coercive field variation. Inset: demagnetization correction for a sample with D=75 nm. Note the great difference in remanence for samples with higher mass.

As is shown in Fig. 2.15 M_r/M_s and H_c follow the same qualitative behavior. When m increases from 3.8 to 7.6, M_r/M_s and H_c first increase rapidly and tend to saturate. To explain this behavior, let's define the wires as nanoparticles. In samples with a reduced aspect ratio, shape anisotropy is not significant, so the dominant anisotropy is magnetocrystalline. Since samples grow policrystalline, each particle easy axis is oriented at random and the Stoner-Wohlfarth model predicts a squareness M_r/M_s=0.5 and a coercive field $H_c = 0.64H_A$. By contrast, when the aspect ratio of the nanoparticles increases, shape anisotropy becomes dominant and all the nanoparticles have their easy axis oriented along the cylinder axis. As the field is applied parallel to wires' axis, above a certain value of aspect ratio, long nanoparticles, or nanowires, present almost squared hysteresis loops (See Fig. 2.15 left) that leads to $M_r/M_s \backsimeq 1$ and coercive field $H_c = H_A$.

In summary, squareness and coercive field increase as the nickel in the pores grows from nanoparticles to form progressively 1D nanowires. This behavior is consistent with the change of dominant anisotropy, which is related with the change in the alignment of the anisotropy axes: random for nanoparticles, aligned for the wires along their axis.

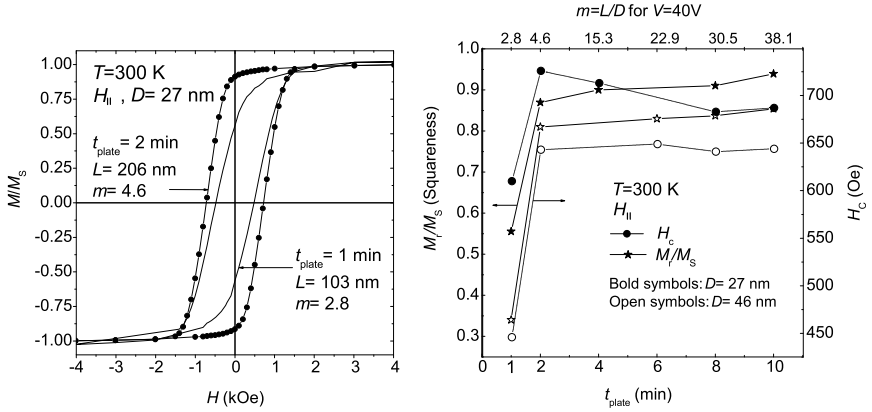

Fig. 2.15. LEFT: normalized hysteresis loops for samples with different aspect ratios. RIGHT: squareness $M_\mathrm{r}/M_\mathrm{S}$ and coercive field H_c of samples synthesized at 40 V (D=27 nm) and 60 V (D=46 nm). Upper scale shows aspect ratio for samples synthesized at 40 V.

We can estimate a value of shape anisotropy K_sh necessary to exceed the intrinsic magnetocrystalline anisotropy K_M of the nickel. In particular, for a prolate spheroid particle, K_sh reads:

$$K_\mathrm{sh} = \frac{1}{2}(N_\mathrm{x} - N_\mathrm{z}){M_\mathrm{s}}^2 \tag{2.5}$$

where N_z and N_x are the demagnetization factors for the parallel and perpendicular component to long axis, respectively. For a prolate particle with an aspect ratio $m = L/D$, with $L > D$ and an eccentricity $\xi = \sqrt{m^2 - 1}/m$, the demagnetization factors, in cgs units, become:

$$N_\mathrm{z} = \frac{4\pi}{m^2 - 1}\left[\frac{1}{2\xi}\ln\left(\frac{1+\xi}{1+\xi}\right) - 1\right] \tag{2.6}$$

$$N_\mathrm{x} = 2\pi(1 - N_\mathrm{z}) \tag{2.7}$$

As we have shown in Fig. 2.15, crossover appears when the aspect ratio arise $m = 4.6$. With this dimensions, $K_\mathrm{sh} \cong K_\mathrm{M}$ in the prolate. Calculating the demagnetization factors, as saturation magnetization M_s(Ni)=482 emu/cm^3 for the bulk nickel, an upper bound for a K_M results $1.21 \cdot 10^5$ erg/cm^3. This value can be compared with a cubic K_M tabulated for nickel crystal $K_\mathrm{M} = 0.5 \cdot 10^5$ erg/cm^3 [Morrish 1965].

Magnetization reversal process: Curling vs Nucleation

In Fig. 2.16, the variation of the coercive field H_c with wire diameter is presented. The filling time of 10 minutes results in wires with enough aspect ratio to achieve the study. Values of M_r/M_s larger than 0.85 (not shown) reveal that the dominant anisotropy can be considered uniaxial and due to shape. Squareness results justify the use of models developed for nearly infinite long wires. From Stoner-Wohlfarth model, consistent with all the spins rotating *in unison*, H_c is expected to be $H_c = (N_x - N_z)M_s$ which results in 3020 Oe for a wire with L=1030 nm (A small reduction with the diameter is due to a variation in the aspect ratio, as is shown in the black line of the Fig. 2.16). The anisotropy constant associated with the shape also can be calculated as $K_{sh} = (1/2)H_cM_s$ and results $K_{sh} = 7.3 \cdot 10^5$ erg/cm^3. As we can observe in Fig. 2.16, experimental results are approximately four times lower than the values expected for this simple model. As a result, although the shape of the hysteresis loops can be qualitatively described by Stoner-Wohlfarth model, for a quantitative analysis, one has to consider other microscopic models of the magnetization reversal. Let us give a brief review of this topic.

On basis of the micromagnetic theory, the magnetization reversal can take place via multiple routes that involve collective spin rotations. Different models of magnetization reversal modes predict different nucleation fields H_n, defined as the minimum field that enables a rotation from the uniform magnetization (i.e. at the saturation value). We expect that, according to theoretical predictions, by means of coercive field, we can distinguish between the magnetization reversal of nanowires with different aspect ratios. Note that, although the relevant information is analogous, the experimental coercive field, that is defined as the field necessary to achieve zero magnetization, differs from this theoretically defined nucleation field. Also, this H_n is predicted at zero temperature, far from our room temperature H_c values. However, some information can be extracted from the present study.

To achieve our objective, theoretical H_n dependence on diameter and length for the different reversal modes may be introduced neglecting the magnetocrystalline anisotropy contribution. During the reversal, two possibilities are expected, *coherent modes*, where the rotation of spins involves all the nanowire volume, or *local or incoherent modes*, where spin rotation initiates in a localized nanowire region.

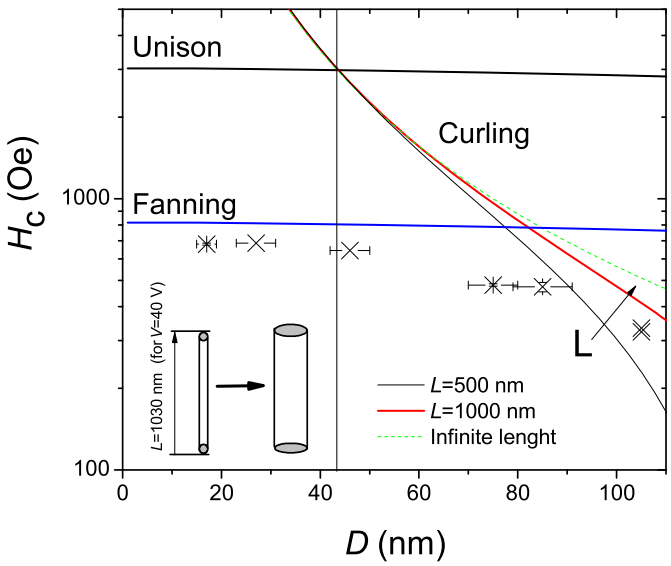

Fig. 2.16. H_c evolution for samples with different diameter. Nucleation field predictions for the diverse reversal modes in samples with a finite length of 1000 nm (length that correspond with sample prepared at 40 V and filled during 10 min) are shown. The vertical line signals the critical diameter D_{cr}. The different curves for curling correspond to wires with various lengths.

Two different coherent reversal modes were found by solving the spin configurations that minimize the free energy during the field-induced reversal:

"In unison" mode

Mechanism "in unison" was introduced in the foregoing sections, when it was assumed that magnetization magnitude $|M|$ remains constant during magnetization changes induced by a magnetic field [Frei 1957]. During the magnetization reversal, magnetization becomes uniform in all the nanowire volume. Nucleation field H_n for a prolate particle with a long axis in z direction reads, according to Stoner-Wohlfarth model:

$$H_n = (N_x - N_z)M_s \tag{2.8}$$

"Curling" mode

This mechanism is characterized for a *spin curling* that is a function of the distance to the wire axis. During the magnetization reversal, although all volume is involved, magnetization becomes non-uniform inside the nanowire volume. For a prolate spheroid, the nucleation field H_{n} [Aharoni 2000] depends on diameter D as follows:

$$H_{\mathrm{n}} = \frac{8Aq^2}{D^2 M_{\mathrm{s}}} - N_{\mathrm{z}} M_{\mathrm{s}} \tag{2.9}$$

where A is the exchange constant (For Nickel A=$1 \cdot 10^{-11}$ Jm^{-1}) and q is a geometrical factor that reads [Aharoni 1998]:

$$q = 1.8412 + \frac{0.48694}{m} - \frac{0.11381}{m^2} - \frac{0.50149}{m^3} + \frac{0.54072}{m^4} - \frac{0.172}{m^5} \tag{2.10}$$

In contrast with these coherent modes, local modes involve the spin reversal in a determined region of the nanowire. Two different incoherent or local modes will be described:

"Fanning" mode

In the fanning mode, an elongated particle is assumed as a linear chain of spheres. This idealized model assumes every sphere uniform in magnitude and interacting only by dipole-dipole interactions [Jacobs 1955]. When a field is parallel to the chain axis, the magnetization of the spheres rotates oppositely to achieve the field orientation. For an infinite wire, the fanning nucleation field with respect the infinite cylinder rotating at unison reads:

$$H_{\mathrm{n}}^{(fanning)} = 0.27 H_{\mathrm{n}}^{(unison)} \tag{2.11}$$

"Nucleation and propagation"

In a ferromagnetic macroscopic sample, the magnetization tends to be aligned with the field by the movement of domain walls through the sample. Domains aligned with field grow, while domains non-aligned reduce, giving a final single-domain structure. In our case, the initial stage is a single-domain structure due to shape anisotropy, so a domain wall may be created inside the wire, probably in a region with a surface or crystalline inhomogeneity that tends to rotate a certain

angle the magnetization with respect the long axis. This local nucleation, with the appearance of a domain wall, and the later propagation along the wire, reduces the "in unison" mode coercive field as follows [Skomski 2002]:

$$H_{\mathrm{n}} = H_{\mathrm{n}}^{(unison)} \left(1 - \frac{4A}{K_{\mathrm{sh}} D_{\mathrm{L}}^2} - \frac{3\left(a\theta(D_{\mathrm{L}}/2)\right)^{3/2}}{4} \right) \tag{2.12}$$

where a is the length of the surface or crystalline inhomogeneity, θ is the angle of the magnetization with respect the long axis when no field is applied in this region and D_L is the localization length, a domain wall length along the wire.

If we assume only a coherent rotation, a critical diameter D_{cr} in the intersection between the curves drawn for reversal "in unison" and "curling" can be defined (It is indicated in Fig. 2.16 by a vertical line, D_{cr}=43 nm). Analysis is detailed in two regions:

- Below D_{cr}

Rotation "in unison" is expected and coercive field does not depend on wire diameter D. Experimentally, lower values than the expected ones for this reversal mechanism are measured. Experimental H_{c} around 700 Oe are 4.3 times smaller than the 3000 Oe predicted by rotation in unison. Coercive values are in good agreement to the coercivity predicted by fanning and very small diameter dependence is shown. The reduction in the values can be ascribed to thermal-activation reversal at room temperature, and is an evidence of the discrepancies between the nucleation field and the coercive field when measurements were done far from 0 K temperature, as we had anticipated in the introduction of the study.

The H_{c} variation with the temperature can be explained as follows. In the classical Neel-Brown theory, the energy barrier due to shape anisotropy U can be overcome by thermal activation. The rate associated with this process follows an Arrhenius law $\Gamma = \Gamma_0 \exp\left(-U/k_{\mathrm{B}}T\right)$ where Γ_0 is an attempt frequency and k_{B} is the Boltzmann constant. Thus, the critical barrier that can be overcome at a certain temperature in an experimental time t_{e} is $U_{\mathrm{c}} = k_{\mathrm{B}}T \ln\left(\Gamma_0 t_{\mathrm{e}}\right)$. On the other hand, the field dependence of the energy barrier follows a power law $U = U_0 \left(1 + H/H_{\mathrm{c0}}\right)^{\alpha}$, where U_0 is the energy when no field is applied. In the conditions where $H = H_{\mathrm{c}}$, $U = U_{\mathrm{c}}$:

$$H_c = H_{c0}\left[1 - \left(\frac{k_B T \ln\left(\Gamma_0 t_e\right)}{U_0}\right)^{1/\alpha}\right] \tag{2.13}$$

As the coercive field has a negative slope respect H_{c0}, when T increases the coercive field H_c decreases, explaining the difference between theoretical predictions and our experimental room-temperature values.

We can conclude that, this phenomenology is probably due to local nucleation mode reversal "fanning". If we assume this nucleation is caused by imperfections [Skomski 2002], assuming equation 2.12 and neglecting the second term, which is an small correction to the first term, the localization length D_L reads 31.72 nm, that may be compared with the intrinsic domain wall length λ_W for nickel. In nickel, λ_W=25 nm [Paulus 1999] in good agreement with our estimation.

- Above D_{cr}

"Curling" reversal mode is expected and coercive field tends to decrease with the wire diameter according to equation 2.9. Experimental results show qualitatively the same behavior. Note that, only in case of curling reversal, the coercive field depends on the wire length. As is shown in Fig. 2.16, the predicted coercive field increases with length as a consequence of the variation in the aspect ratio. We have shown in Fig. 2.15 no coercive field variation for samples with lower diameters. Note that, samples prepared in PAM at 60 V, with D=46 nm, are expected to reverse via curling mechanism in case of very long aspect ratio (for infinite cylinders D_{cr} = 43 nm). However, because of the possibility of local mode reversal mechanisms, this critical diameter increases and no reliable difference can be noted between the two wire diameters (27 and 46 nm) under study. The author suggests to expand this study for nanowires with diameters larger than 100 nm where a coercive field variation with length is expected.

Temperature dependence

As the reader can observe in the previous sections, we have restricted ourselves to discussing data obtained at room temperature. The interest of studying the dependence of H_c with T is to reduce the thermal activation in order to extract the coercive field at zero temperature H_{c0}, as we have discussed previously. H_{c0} allow us to perform a more direct comparison with the different nucleation fields for reversal mechanisms. This parameter gives us more realistic information on the reversal magnetization processes inside the wires. Unfortunately, as T is varied we have found other phenomena that obscure this simple scheme.

Fig. 2.17 shows the temperature dependence of the coercive field. Let's consider first the region below room temperature. Rather surprisingly, and contrary to previous experimental studies [Paulus 1999] and [Zeng 2002], instead of the expected increase, H_c actually decreases when T decreases, and shows a minimum at a finite T. Also, for T=5 K, hysteretic behavior increases when the field is applied perpendicular to the wires, which can be associated with the appearance of a new perpendicular magnetic easy axis that competes with the parallel axis due to shape anisotropy.

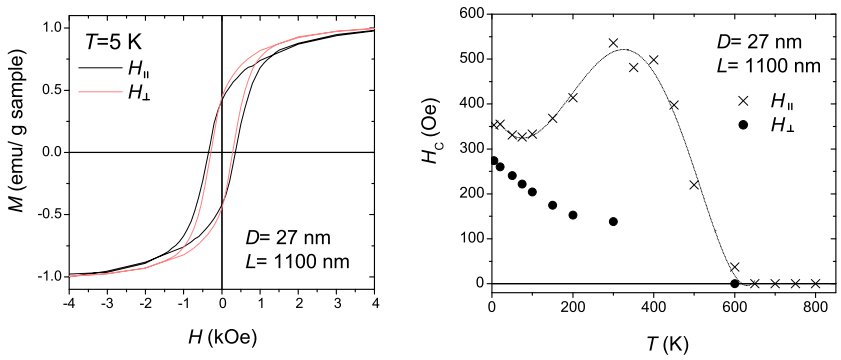

Fig. 2.17. LEFT: hysteresis loops at T=5 K for samples described in adjacent figure when a magnetic field is applied parallel and perpendicular to wires' axis. RIGHT: coercive field vs temperature dependence for a sample synthesized at 40 V and filled during 10 minutes (L=1100 nm, D=27 nm) for parallel and perpendicular applied field of 1000 Oe. Line is a guide to the eye.

- Influence of the magnetostriction

Since magnetocrystalline anisotropy can be neglected due to nickel policrystallinity, this temperature dependence is probably due to extrinsic phenomena ascribed to a thermally-induced magnetoelastic effect [Kumar 2006]. As thermal expansion coefficients (α) for aluminium $\alpha(\mathrm{Al}) = 23.8 \cdot 10^{-6}$ K^{-1}, nickel $\alpha(\mathrm{Ni}) = 13 \cdot 10^{-6}$ K^{-1} and alumina $\alpha(\mathrm{AlO}) = 6 \cdot 10^{-6}$ K^{-1} are rather different, a decrease in temperature produces a compressive stress on the wires. The α positive values indicate that materials expand with temperature increase. As the thickness of the aluminium substrate is very large ($\sim$ 100 μm) with respect to that of the alumina matrix ($\sim$ 3 μm), the aluminium foil exceeds the force exerted by the matrix and cannot be neglected in the analysis [Kumar 2006], oppositely to interpretations [Vazquez 2005][Zeng 2002] that neglect the aluminium effect. If we assume that the aluminium contraction is directly reflected in the nickel (neglecting the nickel-alumina interface) the lateral contraction is determined by the thermal expansion difference $\Delta\alpha = \alpha(\mathrm{Al}) - \alpha(\mathrm{Ni}) = 10.8 \cdot 10^{-6}$ K^{-1}. Assuming a linear temperature dependence of α, the contraction of the nickel wires reads:

$$\frac{\Delta l}{l} = \Delta\alpha(T_\mathrm{f} - T_\mathrm{i}) \tag{2.14}$$

where $\Delta l/l$ is the lateral length variation, and T_i and T_f the initial and final temperature of the sample. For our temperature increment $T_\mathrm{f} - T_\mathrm{i} = -295$ K, length variation results $\Delta l/l = -3.18 \cdot 10^{-3}$. This lateral contraction is reflected in a longitudinal expansion through the Poisson relation:

$$\frac{\Delta l}{l}_{axial} = -(1/\upsilon)\frac{\Delta l}{l}_{lateral} \tag{2.15}$$

where υ is the Poisson's constant, for nickel υ=0.33. Axial deformation value results $9.6 \cdot 10^{-3}$ and the external stress (σ) along the wire, assuming isotropic behavior, can be calculated through the Young modulus E_eff:

$$\sigma = E_\mathrm{eff}\frac{\Delta l}{l} \tag{2.16}$$

The Young modulus is $E_\mathrm{eff} = 20.4 \cdot 10^{10}$ Nm^{-2} at room temperature for bulk nickel, giving $\sigma = 19.5 \cdot 10^{8}$ Nm^{-2}. This leads to a magnetoelastic anisotropy whose anisotropy constant K_σ reads [Morrish 1965],

$$K_\sigma = -\frac{3}{2}\lambda_S \sigma \tag{2.17}$$

where λ_S is the magnetostrictive constant for isotropic samples. For our policrystalline nickel wires, $\lambda_S = -3.4 \cdot 10^{-5}$ [Morrish 1965]. Then, $K_\sigma = 9.9 \cdot 10^5$ erg/cm^3 when the temperature decreases to 5 K (compare with magnetocrystalline $K_M = 1.21 \cdot 10^5$ erg/cm^3 and shape $K_{sh} = 7.3 \cdot 10^5$ erg/cm^3 anisotropy constants calculated in a previous section). Since the energy associated with a directional exerted stress reads $E_\sigma = K_\sigma cos^2\theta$ (θ is the angle between the exerted stress and magnetization) and K_σ has a positive value, the magnetoelastic effect tends to orient spins perpendicular to the wire axis in competition with shape anisotropy [Kumar 2006]. As a result, decreasing the temperature, magnetoelastic effects will turn progressively the net anisotropy axis towards the perpendicular direction and therefore the coercive field value diminishes in measurements with the applied field parallel to wires' axis according with the Stoner-Wohlfarth model.

As nickel is assumed to be intimately linked with the alumina matrix, the alumina contraction and the reduction of the pores is only controlled by the aluminium contraction during the cooling, resulting in a lateral stress of the wires that gives rise to an axial expansion. When aluminium is neglected in this analysis, when T decreases, alumina exerts a tensile stress on the wires that tends to orient the spins along the wire, i.e., just the opposite effect that explains the magnetic phenomenology. In [Paulus 1999], where the aluminium is removed from the sample before the magnetic measurements were done, the coercive field increases by effect of the thermal activation suppression, proving that the thermally-induced magnetoelastic effect is due to the supporting aluminium sheet. We end, thus, the controversy that arises from some recent proposes [Kumar 2006][Vazquez 2005][Zeng 2002].

The interpretation is supported by the data obtained under a magnetic field applied perpendicular to the wires' axis. A monotonic increase of H_c with cooling is observed as a consequence of the turning of this anisotropy axis plus the suppression of thermal activation. As a conclusion, this phenomenon is ascribed to a thermally-induced magnetoelastic effect.

Above room temperature, in a range of temperatures not covered until now, H_c decreases monotonically until temperature arrives to the Curie temperature T_C. When temperature increases, the aluminium sheet tends to expand the nickel (oppositely to temperature reduction)

resulting in a external tensile stress that leads to an axial contraction. In this case, a negative magnetoelastic anisotropy constant tends to orient spins parallel to wire axis, analogous to shape anisotropy. Therefore, when temperature increases, the magnetoelastic effects increase the net anisotropy along the wire, although thermal activation and shape anisotropy diminish as a consequence of M_s reduction. The net effect is a tendency to decrease the coercive field value.

- The wires' length role

Unfortunately, the temperature effect on coercive field, that could help us to distinguish between the different magnetization reversal mechanisms, is hidden by the magnetoelastic effect. Hence, below room temperature, and applying a field parallel to the wire axis, the coercive field shows a temperature minimum for all the wires with different aspect ratios, as is shown in Fig. 2.18. But some information can be extracted from these data. We can define the crossover temperature T_{cross} as the intersection between the low temperature decrease due to thermal activation and high temperature increase due to magnetoelastic effect. T_{cross} is shown in the inset of Fig. 2.18. Its value decreases with increasing wire length and tends to a given value for both diameter sizes. From the Courot formula for the effective Young modulus, E_{eff} of a cylinder of length L and diameter D is given by,

$$E_{eff} = E_{bulk} + \gamma(1 - \upsilon)\frac{L^2}{D^3} \tag{2.18}$$

where E_{bulk} is the bulk Young modulus, γ is the longitudinal stress. As E_{eff} increases with the length L, the magnetoelastic effect becomes larger and the temperature interval when this effect dominates is larger and consequently T_{cross} decreases. As a conclusion, this behavior is ascribed to an increase of the longitudinal stress as the aspect ratio increases, supporting the interpretation of the thermal-induced magnetoelastic behavior of the nickel nanowires.

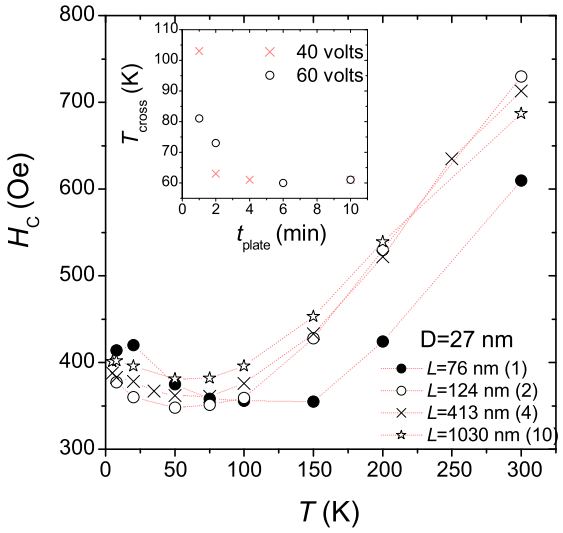

Fig. 2.18. Coercive field dependence with temperature for samples with D=27 nm and various lengths. Inset: crossing Temperatures for samples with D=27 and 46 nm and different lengths.

High temperature data: Size dependent Curie temperature

In order to determine how the Curie temperature changes with the wire diameter, temperature-dependent magnetization measurements were performed at fixed field values. An important advantage of our preparation method is that the nickel nanowires are protected from oxidation and structural damage at elevated temperatures. As we can see in Fig. 2.19 for nanowires with L=1030 nm and D=27 nm, a well defined phase transition between a ferromagnetic and a paramagnetic phases is shown. The Curie temperature was determined as the intersection between linear fits of M in the ordered and paramagnetic regions (See an example on inset of Fig. 2.19).

Ferromagnetic behavior below Curie temperature was confirmed by hysteresis loops measurements. As hysteresis is present in all the ferromagnetic range and only disappears above the Curie temperature, superparamagnetic blocking is not present for these samples. This means that, the anisotropy barrier energy $\Delta E = KV$, where K is the ef-

fective (shape + stress) anisotropy constant, remains sufficiently high to keep a time average remanence also at elevated temperatures. This phenomenon might be of interest for applications since sample replicas, with the information fixed on the magnetization of the wires, can be recorded simply by cooling a "replica" sample while it is in contact over an "original" one. The information can be deleted simply by heating.

Note that $M(T)$ curves for field applied parallel and perpendicular present different values. This is because a field of 1000 Oe field is not able to produce full saturation of magnetization (See Fig. 2.19).

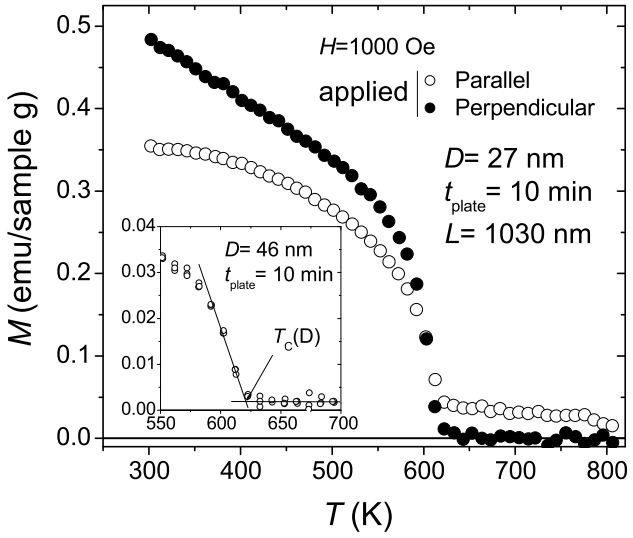

Fig. 2.19. Temperature dependence of magnetization for a sample of D=27 nm and L=1030 nm. Inset: procedure to obtain the Curie temperature.

The Fig. 2.20 shows how the Curie temperature progressively decreases as the wire diameter decreases. This reduction of the Curie temperature is due to finite-size effects, as was predicted theoretically in [D.P.Landau 1976]. In this critical phenomenon, the correlation length $\xi(T)$ of a magnetic system increases with increasing temperature [Stanley 1971] following an asymptotic behavior near the bulk transition temperature $T_C(\infty)$ that reads,

$$\xi(T) = \xi_0 \left| 1 - \frac{T}{T_{\mathrm{C}}(\infty)} \right|^{-\upsilon} \tag{2.19}$$

where ξ_0 is the corresponding length extrapolated to T=0, and υ is the critical exponent for correlation. In systems with small dimensions (as nanowire diameter D) the $\xi(T)$ growth with temperature is constrained by D, resulting in a reduction of the Curie temperature:

$$\frac{T_{\mathrm{C}}(\infty) - T_{\mathrm{C}}(D)}{T_{\mathrm{C}}(\infty)} = \left(\frac{\xi_0}{D} \right)^{\lambda} \tag{2.20}$$

where $T_{\mathrm{C}}(D)$ is the Curie temperature for a nanowire with diameter D and $\lambda = 1/\upsilon$.

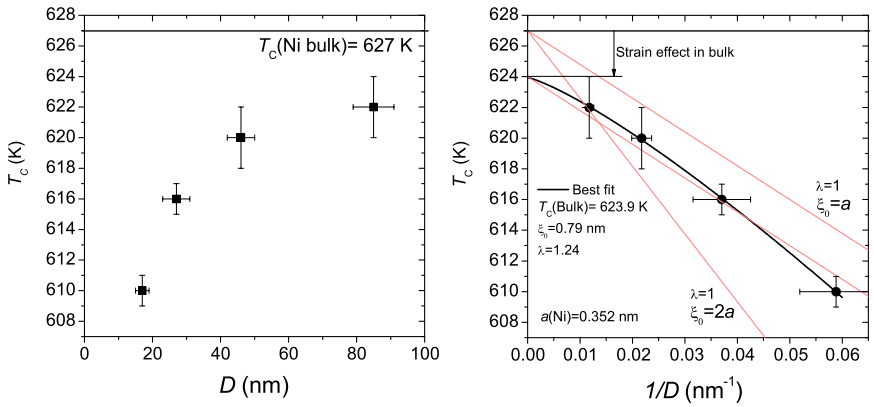

Fig. 2.20. LEFT: Curie Temperatures for samples with different nanowire diameters. RIGHT: Curie Temperature dependence with $1/D$. Black line show the best fit to data. Red lines show theoretical predictions from a simple model where λ=1 and ξ is an a multiple, where a is the length of the nickel unit cell.

As is shown in Fig. 2.20, Curie temperature departs from bulk value (627 K) when size is reduced. However, at larger diameters (extrapolating when $1/D$=0) Curie temperature differs 3 K from bulk value. This situation is not observed in nanowires embedded in mica [Sun 2000] and can be ascribed to strain effects that are absent in mica templates. It is well known, that pressures modifies bond lengths, spin interactions and, as a consequence, the Curie temperature in bulk materials

[Patrick 1954] [Smoluchowski 1954]. The correlation length ξ from our fit results to be 0.79 nm, larger than the length of the unit cell, as is expected for a ferromagnetic material, but far from 2.2 nm reported by [Sun 2000]. As a conclusion, the stresses modify the nickel bond lengths, reducing ferromagnetic interaction, and resulting in a bulk transition variation and in a correlation length decrease. Our value $\lambda = 1.24 \pm 0.08$ is close to the value predicted by a 3D Heisenberg model (λ=1.4) that assumes only nearest neighbors interactions. Our value is, in fact, closer to this theory than the value obtained by Sun (λ=0.94) in good agreement with the reduction of the correlation length.

2.3 Conclusions

- Controlling some different synthesis parameters, such as anodization voltage, anodization time or plating time, well controlled size, length and morphology nanowires were synthesized.
- Magnetic response in wires with different aspect ratios show evidences from particle-to-wire crossover above an aspect ratio $m = L/D$=4.6.
- Hysteresis loops in nanowires are determined by a shape anisotropy that competes below room temperature with a thermally-induced magnetoelastic anisotropy.
- Room temperature coercive field values lower than the predicted in the Stoner-Wohlfarth "in unison" model were measured. The coercive field for nanowires with different diameter shows an agreement with "nucleation and propagation" fanning reversal mode for diameters lower than 43 nm (A mode usually neglected). For larger diameters "curling" reversal mode is in qualitatively agreement with our experimental data.
- Below room temperature, compression stress due to different thermal expansion coefficients between aluminium and nickel induce thermally-induced magnetoelastic effects that reduce the coercivity. The latter behavior is shown only if aluminium is not removed from the samples. This aluminium influence ends a controversial question about the origin of this effect.
- The effect of stress on the coercive field is influenced by the aspect ratio of the samples, as is shown in the different dependence of the coercive field with the temperature.

- Above room temperature, in a range of temperatures not covered until now, the aluminium expansion produces a tensile stress that is the responsible of a coercive field maximum at room temperature.
- The variation of magnetization with temperature does not show any evidence of a superparamagnetic blocking, which confers to the material an important application in data storage devices.
- The Curie temperature progressively decreases with decreasing wire diameter. In agreement with models, this reduction of the Curie temperature is due to finite-size effects.
- The Curie temperature extrapolated to infinite diameter shows a decrease of about 3 K with respect the bulk value. This suggest that stresses, whose presence and influence on the magnetic properties have been put into evidence by hysteresis experiments, also modify T_{C}. This effect is not present for nickel nanowires embedded in mica, where stresses are very weak.

3

Nonlinear magnetic susceptibility in Mn_{12} single-molecule magnets

3.1 Introduction: Mn_{12}, nonlinear susceptibility and tunnelling effect

Molecular chemistry provides a "bottom-up" approach to produce new magnetic materials with interest for basic science as well as with promising applications [Kahn 1993] [Miller 2002] [Gatteschi 2006]. From these materials, the ever-growing family of single-molecule magnets (SMM) [Gatteschi 2006] [Christou 2000] [Gatteschi 2003] stands out for its appeal to the research on the foundations of Quantum Physics. Single molecule magnets are metal-organic clusters made of a magnetic core surrounded by a shell of organic ligands. One of the most studied SMM is Mn_{12}. SMM are neutral entities that form molecular crystals bound by weak Van der Waals interactions. Their basic magnetic properties (ground-state spin and magnetic anisotropy) are however characteristic of the isolated clusters. Indeed, they appear to be preserved in solution [Sessoli 1998] [Domingo 2004] [El Hallak 2007] or even when they are deposited onto solid substrates [Zobbi 2005] [Cavallini 2005] [Martínez 2007].

In this respect, SMM can be seen as a close analogue to magnetic nanoparticles, with the advantageous difference of being all identical to each other. The analogy was strengthened by the discovery, made in 1994 by R. Sessoli and co-workers [Sessoli 1993], that Mn_{12} SMM show magnetic hysteresis, i.e. magnetic memory, at liquid helium temperatures. The magnetic hysteresis does not result from long-range magnetic order induced by intermolecular interactions. Instead, it is the signature of the superparamagnetic blocking or freezing of the molecular spins by the anisotropy energy barriers that hinder, and therefore slow-down,

the spin-flip. These clusters are, therefore, potential candidates to store information at the molecular level. Achieving this technological goal requires however that memory is preserved above room temperature, which, in turn, depends on our understanding of the basic principles that rule the magnetic relaxation in these materials. Hysteresis in SMM turns out to be rather unconventional though.

In the case of macroscopic magnets, hysteresis can be fully understood in terms of classical physical laws, which describe the dynamics of domain walls [Chudnovsky 2006]. The same applies to nanosized magnetic particles [Brown 1963] as well, at least at not too low temperatures (but see e.g. ref. [Wernsdorfer 1997] for an exception to this statement). The hysteresis and, in general, the spin dynamics of SMM reveal by contrast signatures of fascinating quantum phenomena, which result from their very small size and the discreteness of their magnetic energy level scheme. In this respect, these systems are ideally suited to investigate the fuzzy borderline between the classical and quantum worlds [Zurek 2003][Leggett 2002]. In 1996, it was found that the magnetization reversal of Mn_{12} clusters becomes faster at magnetic fields where magnetic states with opposite spin orientation (i.e. spin-up and spin-down states) become degenerate in energy [Friedman 1996] [Hernandez 1996] [Thomas 1996]. At these fields, the possibility of crossing the energy barrier by quantum tunnelling (QT) provides a kind of short-cut to the magnetic relaxation process [Garanin 1997] [Luis 1998] [Fort 1998] [Leuenberger 1999].

In the last decade, a great variety of experimental and theoretical tools have been applied to the study of quantum tunnelling in SMM [Gatteschi 2006]. The dynamical or frequency-dependent magnetic susceptibility $\chi(\omega)$ deserves to be mentioned, since it has become a conventional characterization technique in Chemistry labs. In fact, the onset of a cusp in the imaginary component χ'' represents the fingerprint of the SMM behavior [Gatteschi 2006]. It is for this reason rather surprising that the nonlinear equivalent of χ has been virtually ignored in this research field, more so if one considers the relevance of this technique in the study of other magnetic materials, such as classical or quantum spin-glasses [Schiffer 1995] [Wu 1993] [Jonsson 2007] and magnetic nanoparticles [Barbara 2007] [Bitoh 1993] [Mamiya 1998] [Jonsson 1998a] [Jonsson 2000] where important dynamical effects are also observed.

Furthermore, it was expected that the nonlinear susceptibility could provide unique information on some aspects of the magnetic relaxation process of SMM that remain rather obscure. In 1996, García-Palacios and Svedlindh [Garcia-Palacios 2000b] predicted that the nonlinear dynamical susceptibility of classical superparamagnets, such as magnetic nanoparticles, can become very large for some frequencies and, in sharp contrast to the linear susceptibility, quite sensitive to the coupling of spins to their environment (lattice vibrations, conduction electrons, nuclear spins, etc, usually referred to as the bath). One therefore hopes that the same information might be extracted from this quantity also in the case of superparamagnets, such as SMM, showing quantum dynamics. For these materials, the coupling to the bath acts as the main source of decoherence [Weiss 1993] [Chudnovsky 2004] [Dube 2001] an effect that not only limits the observation of quantum phenomena to microscopic bodies but also constitutes the main limitation to their applications (in e.g. quantum information processing) [Leuenberger 2001] [Tejada 2001] [Ardavan 2007].

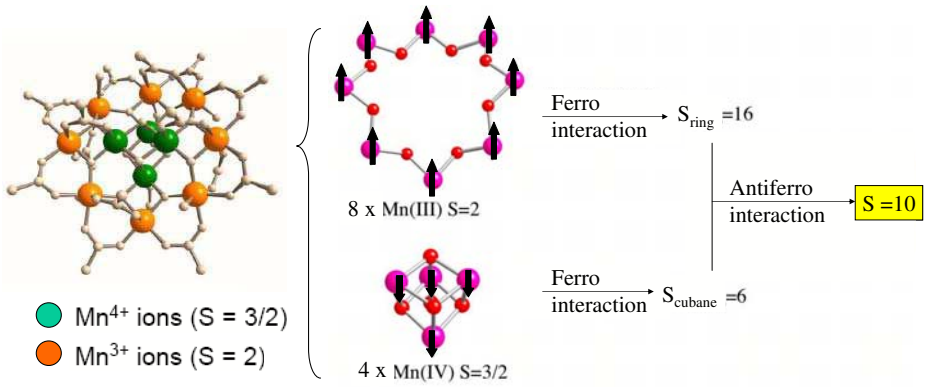

Fig. 3.1. LEFT: Mn_{12} core representation. Mn nucleus are super-exchange coupled via oxo groups. RIGHT: Spin interactions inside the molecule.

Mn_{12} magnetic description: Possibility of tunnelling effect

The most studied single-molecule magnet is Mn_{12}. The molecular structure contains four Mn^{4+} (s=3/2) ions in a central cubane structure surrounded by a ring of eight Mn^{3+} (s=2) ions. The Mn^{3+} and Mn^{4+} are antiferromagnetically coupled via super-exchange interactions, which gives a high-spin ground state $S = 10$ (see Fig. 3.1). The Jahn-Teller distortion on the Mn^{3+} sites leads to a strong uniaxial anisotropy (for other examples [Blundell 2004][Evangelisti 2006]). Furthermore, they form molecular crystals in which all molecules are nearly identical.

The energy levels have a bistable structure $\varepsilon_m \sim -Dm^2$ (at zero field) with an energy barrier $U = \varepsilon_0 - \varepsilon_S$ to be overcome for the spin reversal. Because of the anisotropy barriers, these systems show the typical behavior of superparamagnets, such as blocking or hysteresis, yet at a much smaller size scale [Sessoli 1993]. Spin reversal can take place via either thermal activation or tunnelling or via a combination of those two processes (see Fig. 3.2) in a characteristic relaxation time τ. First evidences showing the existence of resonant spin tunnelling between nearly degenerate spin states (e.g. $\pm m$ at zero field) was found in 1996 [Friedman 1996][Hernandez 1996][Thomas 1996].

The simplest Hamiltonian that describes the magnetic behavior of an isolated Mn_{12} molecule contains the Zeeman plus uniaxial anisotropy terms (see Fig. 3.2):

$$\mathcal{H} = -DS_z^2 - A_4 S_z^4 - g\mu_B(H_x S_x + H_y S_y + H_z S_z) \qquad (3.1)$$

Here, D and A_4 are second and fourth-order anisotropy constants for Mn_{12} and $H_{x,y,z}$ the components of the field along the (a, b, c) crystallographic axes. For Mn_{12} in an acetate crystal, $D \simeq 0.6$ K and $A_4 \simeq 10^{-3}$ K . The energy barrier is approximately $U = \varepsilon_0 - \varepsilon_S \simeq 70$ K.

As is well known, tunnelling probabilities decrease exponentially with the height of the barrier to be tunneled through (height that grows with the system size). At the same time, external perturbations can induce decoherence that degrades the quantum behavior. Furthermore, an external magnetic field H_z detunes energetically the initial and final states for tunnelling (i.e., those having $+m$ and $-(m + n)$ spin projections along $\boldsymbol{z}$). Actually, many experiments have shown that tunnelling takes place at those fields where states of opposite orientation are degenerate, $H_n \simeq nH_1$ ($n = 0, 1, 2, \ldots$ with $H_1 = 2g\mu_B D \simeq 4200$ Oe in Mn_{12}), whereas it is suppressed for intermediate fields. This *resonant tunnelling* enables the spins to approach faster their equilibrium state,

giving rise to steps in the hysteresis loops around $H_z = H_n$ and to maxima in the linear dynamical susceptibility χ_1.

The nonlinear susceptibility χ_2, χ_3, fruitfully exploited in studies of spin-glasses [Schiffer 1995], random anisotropy systems [Harris 1973], but also in magnetic nanoparticles [Bitoh 1993], has been overlooked in the study of SMM.

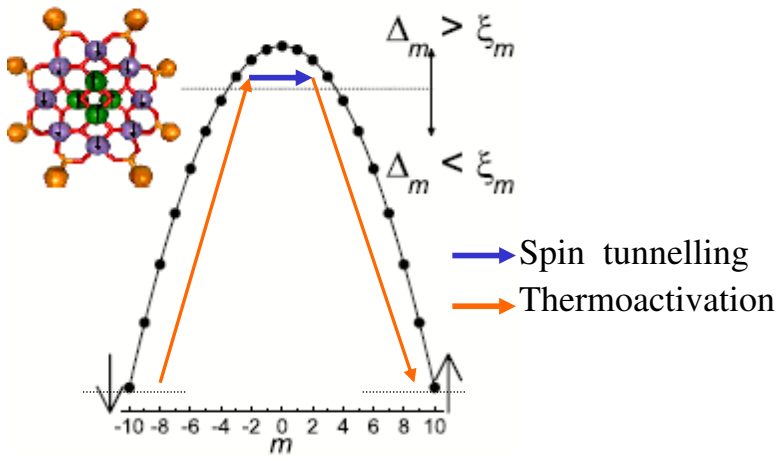

Fig. 3.2. Energy levels for Mn_{12} (the molecule is sketched in the inset along with the spin orientations of the Mn ions). The levels are plotted vs. the quantum number m at $H = 0$ and show the bistable potential for the spin due to the magnetic anisotropy. The horizontal line marks the border between "classical" or localized energy levels, $\Delta_m < \xi_m$, and the tunnelling levels $\Delta_m > \xi_m$ (Δ is the tunnel splitting and ξ the width of the environmental bias-field distribution).

For *classical* superparamagnets χ_3 provides information on parameters to which the linear susceptibility is less sensitive, like the anisotropy constant D [Garcia-Palacios 2000a] or the spin-bath coupling parameter λ [Garcia-Palacios 2000b] (which enters the scene due to the strong dependence of the relaxation rate $\Gamma = 1/\tau$ on *transverse* magnetic fields [Garanin 1999]). Besides, the dynamical nonlinear susceptibility has a genuinely *quantum* contribution due to the detuning of the energy levels by a *longitudinal* field [Luis 2004]. It has a sign opposite to the classical (precessional) contribution, thus enabling to ascertain whether quantum effects, such as resonant tunnelling, are relevant in a given nanomagnet.

Chapter outline

In next sections, experimental results for the thermal-equilibrium and dynamical nonlinear susceptibility of Mn_{12} crystals will be presented. Initially, a description of samples studied and the experimental techniques required to measure it are described. Afterwards, the dependence of the nonlinear response on temperature, frequency, and orientation at zero field is studied in Mn_{12} acetate. A major result is that the nonlinear susceptibility is dominated by a very large contribution, hitherto unforeseen, with no analogue in Classical Physics. Experiments performed varying the orientation of the crystal's axis with respect to the applied magnetic field provide the first estimate of the decoherence time for thermally assisted tunnelling. Next, we shall show how the tunnelling contribution to the nonlinear response can be switched on and off by varying an external field, tuning and breaking successively the resonances. Finally, using the same experimental methods and techniques explained for acetate crystals, we shall study a "fast relaxation" Mn_{12} benzoate crystals. Experiments show that this species provide an example of how the interaction with the "external world" can, effectively, suppress quantum effects, thus approaching the classically expected behavior.

3.2 Experimental method

Samples

Single crystals of Mn_{12} acetate, whose molecular formula is $(Mn_{12}O_{12}(CH_3COO)_{16}(H_2O)_4)\cdot 2CH_3COOH\cdot 4H_2O$, were produced in our institute ICMA (CSIC-University of Zaragoza) by Dr. A. Millán. Crystals were grown following a procedure similar to that described by Lis [Lis 1980]. The concentrations of the reactants, however, were higher than those of [Lis 1980] in order to increase the supersaturation and the growth rate, yielding larger crystals. These were regrown several times by renewing the mother solution. X-ray diffraction patterns of powdered crystals agreed with simulated patterns from the known crystal structure. Dimensions of a single crystal were typically $3 \times 0.5 \times 0.5$ mm^3.

Mn_{12} acetate crystal has tetragonal symmetry (a=b=1.7319 nm, c=1.2388 nm). The Jahn-Teller distortion on the Mn^{3+} sites leads Mn^{3+} to have an elongated octahedron environment parallel to the

molecular axis. This is the origin of the strong uniaxial anisotropy. Thus, the magnetic easy axis (z) is parallel to the Mn_{12} molecular axis and coincides with the c axis and with the large facet of the tetragonal crystal needles (Fig. 3.3). This fact makes Mn_{12} acetate very easy to orient in a magnetic field.

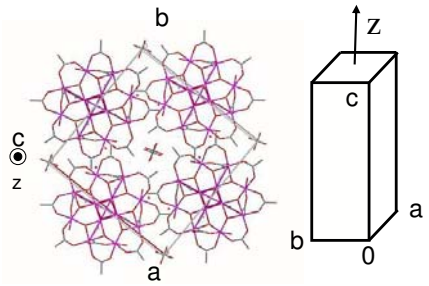

Fig. 3.3. Projection of the unit cell of Mn_{12} acetate along the c axis. z easy axis coincides with c axis (long facet in crystal needle).

Single crystals of Mn_{12} benzoate, whose molecular formula is $(Mn_{12}O_{12}(C_6H_5COO)_{16}(H_2O)_4)\cdot 2C_6H_5COOH$, were produced by Dr. K. Awaga and Dr. K. Takeda in University of Tokyo. The starting material $Mn_{12}Ac$ was prepared by a modification of the literature procedure [Lis 1980]. To a slurry of $Mn_{12}Ac$ in CH_2Cl_2 an excess of $C_6H_5CO_2H$ was added and the resulting mixture was stirred for 48 h. Black block crystals ($3 \times 0.8 \times 0.5$ mm^3) were grown by the addition of hexane, using twice as much as the CH_2Cl_2 [Takeda 2002].

This Mn_{12} benzoate compound has orthorhombic symmetry (a=2.7142 nm, b=5.618 nm, c=1.691 nm). In contrast with the situation found in the acetate crystals, the magnetic z easy axis of the Mn_{12} molecules is tilted 12° with respect to the molecular axis. For Mn_{12} benzoate molecules, z is located in the ab plane, in comparison with those on acetate crystal, where z is parallel to the crystallographic c axis. Furthermore, in the unit cell we can distinguish two Mn_{12} subunits, S1 and S2, with their z axis tilted 37° and -37° with respect to the b axis respectively (data extracted from [Takeda 2002]). To orient the sample with respect to the magnetic field it is necessary to know the deviation between the crystal needle facets and b axis, which is represented in Fig. 3.4.

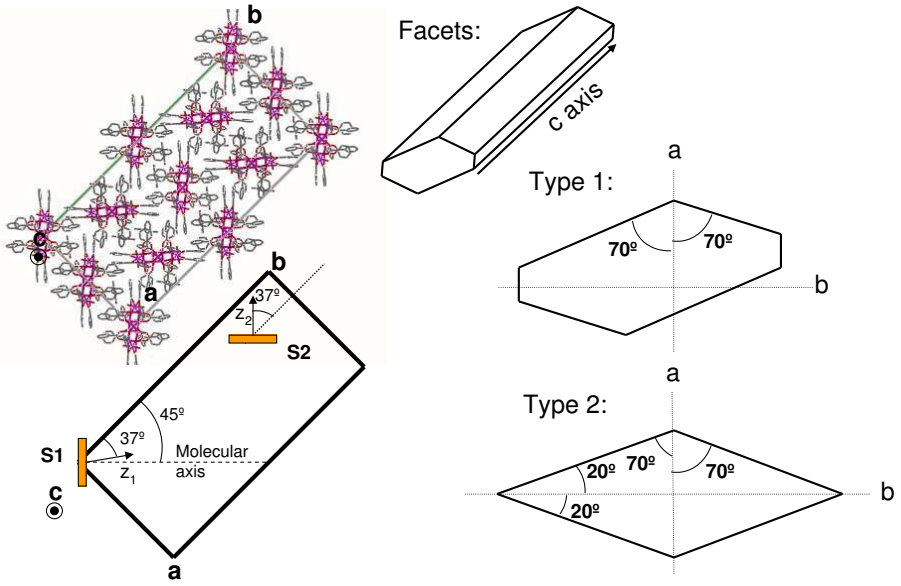

Fig. 3.4. LEFT: Projection of the unit cell of Mn_{12} benzoate along the c axis. In the schematically representation, only one Mn_{12} molecule type is represented. Note easy axis in each case with respect b axis. RIGHT: Representation of crystallographic axes on a crystal needle.

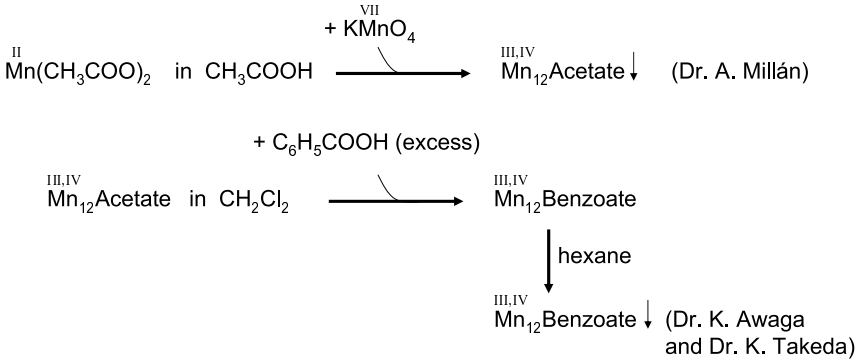

Fig. 3.5. Synthesis route for Mn_{12} single crystals studied in the present thesis. Roman numbers indicates the oxidation number of the Mn in the compound.

Magnetic measurements

To measure the nonlinear susceptibility, two different methods were employed. The zero-field nonlinear susceptibility is obtained from polynomial fits of the H-dependent linear susceptibility. The quadratic coefficient gives $\chi_3(\omega)$. When a magnetic field is applied, an inductive conventional method is employed, measuring the AC response components. $\chi_2(2\omega)$ and $\chi_3(3\omega)$ were measured as responses of the different harmonics (2ω, 3ω,...) to the principal frequency ω.

- Method I: Zero field susceptibility from linear susceptibility field expansion "$\chi_3(\omega)$"

Dynamical susceptibility measurements were performed using the ac option of a commercial SQUID magnetometer, by applying an alternating field $\sim \Delta h e^{i\,\omega t}$. The ac susceptibility was measured under a weak superimposed dc field H, parallel to the oscillating one. Near zero field, the first harmonic of the response can then be expanded as

$$\chi(\omega, H) = \chi_1(\omega) + 3\chi_3(\omega)H^2 + 5\chi_5(\omega)H^4 + \cdots \tag{3.2}$$

The H-independent expansion coefficients give the ordinary linear susceptibility χ_1 and the nonlinear ones χ_3, χ_5,... at zero field. We focus on χ_3 and refer to it as the nonlinear susceptibility.

To determine the nonlinear susceptibility we performed polynomial fits of the H-dependent ac data whose quadratic coefficient gives χ_3. An illustrative example of the fitting procedure is shown in Fig. 3.6. For sufficiently low H, a good description is provided by a simple parabolic dependence $\chi_1 + 3\chi_3 H^2$. For increasingly larger fields, we increased the order of the polynomials whenever the fitting error became greater than 5%. The experimental χ_3 was taken as the mean value of all quadratic coefficients obtained from the different order polynomials, thus minimizing the error of the determination.

The measurements were performed at temperatures $T > 2$ K and frequencies $\omega/2\pi < 1.5$ kHz. The amplitude of the ac fields was $h_0 \leq 4.5$ Oe. This amplitude has to be sufficiently small not to induce any nonlinearity in h_0 (associated to the generation of harmonics).

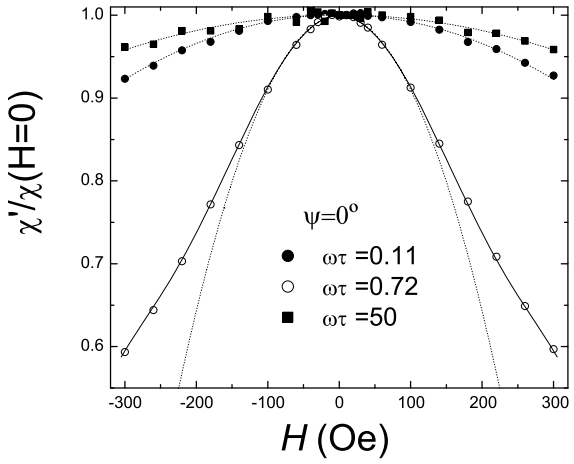

Fig. 3.6. Magnetic ac susceptibility of a single crystal of $Mn_{12}Ac$, normalized by its zero-field value, vs. the static field H (parallel to the anisotropy axes, $\psi = 0$). Results for the *real part* at $T = 5$ K and various frequencies $\omega\tau$ are shown. The solid lines represent polynomial fits from which χ_3 is obtained. The parabolic approximation $\chi_1 + 3\chi_3 H^2$, which dominates the low-field behavior ($|H| \lesssim 100$ Oe), is shown by dotted lines.

Decoherence time studies on magnetic excited states of Mn_{12} were performed by studying the angular variation of $\chi_3(\omega)$. To measure the magnetic response at different orientations with respect to the applied magnetic field, we fabricated a rotating sample holder (see Fig. 3.7). This sample holder enables rotating the crystallographic axis (i.e. c axis defines the anisotropy axes of the Mn_{12} molecules in acetate crystals) a given angle ψ with respect to the magnet axis. This angle is measured with a precision better than 0.5 degrees. To calibrate the position of the zero angle we used the measured linear equilibrium susceptibility, which should be maximum when the field is parallel to the anisotropy axis ($\psi = 0$).

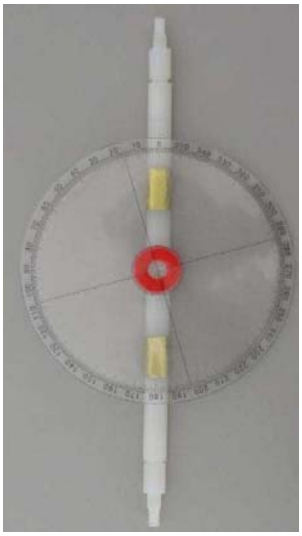

Fig. 3.7. Rotating sample holder photo. A removable coupled angle rotator is mounted on the holder.

- Method II: Nonzero field susceptibility from harmonic response "$\chi_2(2\omega)$ and $\chi_3(3\omega)$"

Clearly, the previous method is not applicable to study how χ_3 depends on the external magnetic field itself. For this reason, in the present experiments we resorted to the more traditional method of measuring the different harmonics $m(2\omega)$ and $m(3\omega)$ of the response to a large ac field $h = h_0 cos(\omega t)$. The amplitudes of different harmonics read $m(2\omega) = (1/2)\chi_2(2\omega)h_0^2$ and $m(3\omega) = (1/4)\chi_3(3\omega)h_0^3$. Thus, the analysis of harmonics provides a direct determination of the non-linear susceptibilities. In the absence of bias field one should have $\chi_2 \equiv 0$. A nonzero H_z, however, makes χ_2 the leading nonlinear term.

We employed the susceptibility option of a commercial multipurpose measuring platform (PPMS) which uses a conventional inductive method. It enables applying ac fields of amplitude $h_0 \leq 17$ Oe, and to selectively detect several harmonics of the exciting frequency $\omega/2\pi < 10$ kHz. To separate the intrinsic nonlinear response of the sample from the possible contamination due to non-perfect harmonicity of the exciting ac coil, we measured the output signals $m_2(2\omega)/h_0$ and $m_3(3\omega)/h_0$ at several amplitudes h_0. This gives the sought-for intrinsic contributions χ_2 and χ_3 as the terms proportional to h_0 and h_0^2 respectively. An example of this procedure is shown in Fig. 3.8.

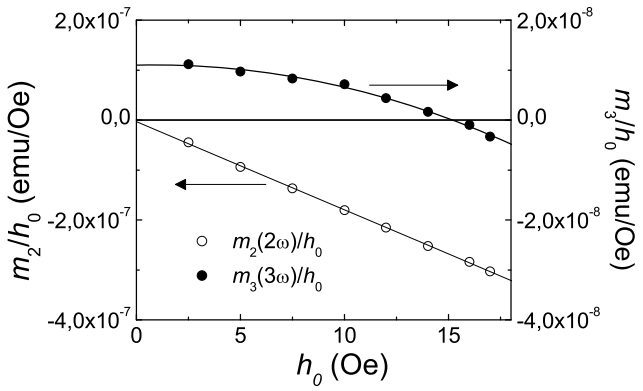

Fig. 3.8. Illustration of the method employed for measuring the nonlinear susceptibilities (here $T = 8$ K, $H_z = 100$ Oe, and $\omega/2\pi = 2$ kHz) . $\chi_2(2\omega)$ and $\chi_3(3\omega)$ are obtained, respectively, from the slope and the quadratic coefficient of the second $m_2(2\omega)/h_0$ and third $m_3(3\omega)/h_0$ harmonics of the output signal, measured as a function of the ac field amplitude h_0.

3.3 Nonlinear susceptibility of Mn_{12} acetate

3.3.1 Equilibrium nonlinear susceptibility and magnetic anisotropy

Depending on the relation between the reversal time τ and the observation time $t_{\rm obs}$, different phenomenologies can be found. For $\tau \ll t_{\rm obs}$, the spin exhibits the thermal-equilibrium distribution of orientations as in a (super)paramagnet; (here "super" refers to the high molecular spin S compared with that of conventional paramagnets). When $\tau \gg t_{\rm obs}$, in contrast, the reversal mechanisms appear *blocked* and the spin stays close to an energy minimum (stable magnetization conditions appropriate for magnetic storage). Finally, under intermediate conditions ($\tau \sim t_{\rm obs}$) one finds *non-equilibrium phenomena* i.e., magnetic "relaxation".

When is the system in equilibrium? A practical criterium

Let's us define here a practical criterion to decide when the experimental linear and nonlinear susceptibility measurements, $\chi_1(\omega)$ and $\chi_3(\omega)$, correspond to equilibrium or off-equilibrium conditions. In the

temperature range covered by our experiments, $T > 2$ K, the molecular spins of Mn_{12} relax via a thermally-activated tunnelling mechanism [Friedman 1996] [Hernandez 1996] [Thomas 1996] (See Fig. 3.2). This process gives rise to a well-defined relaxation time τ and the ac response can be described by a simple Debye formula:

$$\chi = \chi_S + \frac{\chi_T - \chi_S}{1 + i\,\omega\tau} \tag{3.3}$$

Here χ_T and χ_S are the isothermal (thermal equilibrium) and adiabatic limits of χ. In Fig. 3.9 we show how the response of the Mn_{12} crystals follows equation (3.3) at temperatures and magnetic fields typical of our experiments. The equilibrium regime corresponds to frequencies fulfilling $\omega\tau \ll 1$ (left part of the plot), relaxation effects become important when the range $\omega\tau \sim 1$ is approached. The large constant χ' at high ω does not reveal a large χ_S, but it corresponds to the χ_T of a minority fraction of clusters with lower D or "fast relaxing" molecules. For a discussion on the nature of these Mn_{12} species see [Sun 1999] and section 3.4.

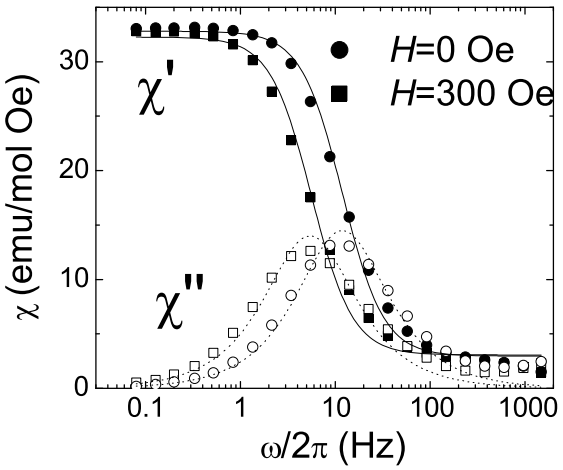

Fig. 3.9. Magnetic susceptibility vs. frequency measured along the anisotropy axis ($\psi = 0$) at $T = 5$ K. Results are shown at zero bias field (circles) and at $H = 300$ Oe (squares). Solid symbols are for the real part (in-phase component) and open symbols for the imaginary part (out-of-phase). The lines are fits to the Debye law (3.3) with $\tau|_{H=0} = 1.3(3) \times 10^{-2}$ s and $\tau|_{H=300} = 2.8(1) \times 10^{-2}$ s.

On the other hand, the relaxation time of this system increases exponentially as T decreases, following an Arrhenius law.

$$\tau = \tau_0 \exp\left(U/k_{\mathrm{B}}T\right) \tag{3.4}$$

Here U is an activation energy and τ_0 an attempt time, which set the magnitude and temperature dependence of τ. At zero field we obtained $U_0 \simeq 65$ K and $\tau_0 \simeq 3 \times 10^{-8}$ s [Luis 2004]. In a χ vs. T experiment (Fig. 3.10) the condition $\omega\tau = 1$ defines a superparamagnetic "blocking" temperature $k_{\mathrm{B}}T_{\mathrm{b}} = -U_0/\ln(\omega\tau_0)$. Below T_{b}, the real part χ_1' drops from χ_{T} towards χ_{S} whereas χ_1'' departs from zero and shows a maximum. The same blocking phenomenon can be seen in the nonlinear susceptibility. The non-equilibrium response near T_{b} leads also to a non-zero imaginary part χ_3'', and to a strong deviation of χ_3' from the equilibrium $\chi_{3\mathrm{T}}$. In contrast with the linear response (which decreases from χ_{T}), χ_3' becomes *larger* than $\chi_{3\mathrm{T}}$ near T_{b} [Luis 2004]; this dynamical nonlinear phenomenon will be discussed in detail in the following sections 3.3.2–3.3.4.

As can be seen in figures 3.9 and 3.10, the transition from isothermal to adiabatic conditions extends over a certain frequency or temperature range, determined by the width of the $\chi''(\omega, T)$ curve. As a practical rule, we take $\chi_{\mathrm{T}} = \chi_1'$ and $\chi_{3\mathrm{T}} = \chi_3'$ when the imaginary parts are reasonably small $\chi''/\chi' < 10^{-2}$. This value is, as a matter of fact, close to the experimental error of the present measurements. Using this criterion we have extracted, from the dynamical susceptibility data vs. T, the equilibrium χ_{T} and $\chi_{3\mathrm{T}}$ discussed later.

Equilibrium Study

Mn_{12} acetate measurements were performed on powder and single crystal (typical dimensions: $3 \times 0.5 \times 0.5$ mm^3). In the later case, the field was applied parallel to the crystallographic $\boldsymbol{c}$ axis.

The equilibrium χ_{T} obtained as described in the previous section is shown in the inset of Fig. 3.10. In the temperature range 4 K $< T <$ 10 K it approximately follows a Curie-Weiss law

$$\chi_{\mathrm{T}} = \frac{C}{T - \theta} \tag{3.5}$$

with a Curie temperature $\theta \simeq 1.2(2)$ K. This finite θ, points actually to the presence of dipolar interactions between the molecular spins in the crystal, which would give rise to long-range order at sufficiently low

temperatures [Luis 2005]. In the (super)paramagnetic regime of interest here, interactions merely produce a susceptibility somewhat larger than that of non-interacting clusters.

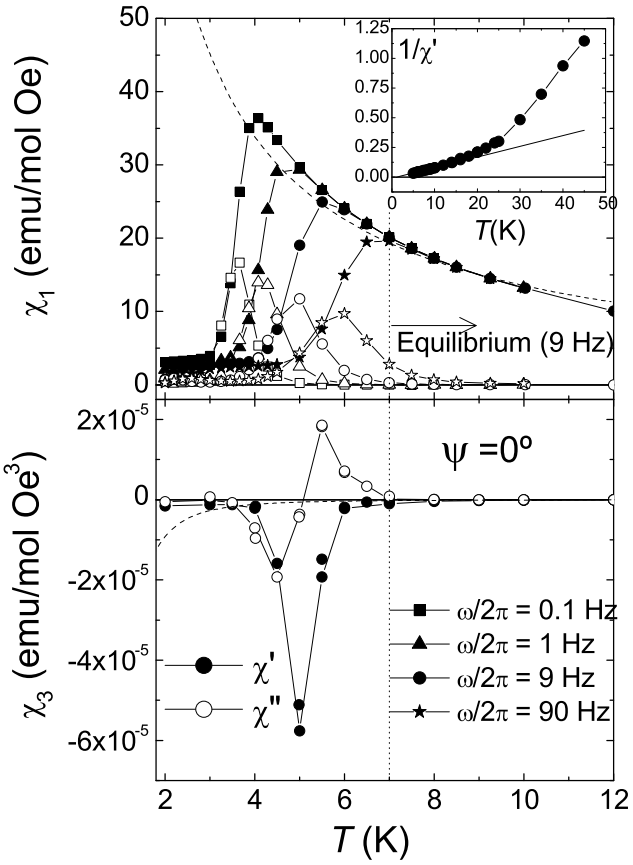

Fig. 3.10. Linear (top panel) and nonlinear susceptibilities (bottom) vs. temperature for several frequencies (only 9 Hz for χ_3) measured along the anisotropy axis. Solid symbols are for the real parts and open symbols for the imaginary parts. Dashed lines are the equilibrium susceptibilities in the Ising (large anisotropy) limit [equations (3.9) and (3.10)]. The vertical line marks the boundary above which thermal equilibrium results are safely obtained using $\omega/2\pi = 9$ Hz. Inset: temperature dependence of the reciprocal *equilibrium* linear susceptibility and its fit to a Curie-Weiss law (3.5) for $T < 10$ K.

In addition to interactions, a most important influence on the temperature-dependent susceptibilities is exerted by the magnetic anisotropy [Carlin 1986]. To illustrate these effects, it is helpful to normalize the experimental $\chi_{\rm T}$ and $\chi_{\rm 3T}$ by their isotropic limits, $\chi_{\rm iso}$ and $\chi_{\rm 3iso}$. For isotropic spins, we can get the equilibrium linear and nonlinear susceptibilities by expanding the Brillouin function around zero field:

$$\chi_{\rm iso} = N_{\rm A}\frac{(g\mu_{\rm B})^2 S(S+1)}{3k_{\rm B}T} \tag{3.6}$$

$$\chi_{\rm 3iso} = -N_{\rm A}\frac{(g\mu_{\rm B})^4}{45(k_{\rm B}T)^3}S(S+1)[S(S+1)+\tfrac{1}{2}] \tag{3.7}$$

where $N_{\rm A}$ is the Avogadro's number, i.e. the number of molecules per mol. The first of these is merely Curie's law and the second is the nonlinear equivalent. Normalized by $\chi_{\rm iso}$ and $\chi_{\rm 3iso}$, the experimental susceptibilities lose their bare $1/T$ and $1/T^3$ contributions, so that their remaining temperature dependence is mostly due to the effects of the anisotropy.

The so normalized equilibrium susceptibility data are shown in Fig. 3.11. Clearly, the isotropic limit is only attained for sufficiently high temperatures ($T \gtrsim 30$ K). Note that the high-T limits of $\chi_{\rm T}$ and $\chi_{\rm 3T}$ are slightly smaller than $\chi_{\rm iso}$ and $\chi_{\rm 3iso}$. This is caused by the thermal population of higher-energy spin multiplets of the cluster, the lowest of which has $S = 9$ in Mn_{12}. Therefore, in that temperature range the Mn_{12} molecule can no longer be seen as a superparamagnetic spin $S = 10$ and the thermal mixture of spin states reduces its susceptibility.

As the temperature decreases, both $\chi_{\rm T}/\chi_{\rm iso}$ and $\chi_{\rm 3T}/\chi_{\rm 3iso}$ increase, departing from $\simeq 1$. This is natural since equations (3.6) and (3.7) are only valid when the thermal energy $k_{\rm B}T$ is larger than all zero-field splittings (produced by the magnetic anisotropy).

The largest zero-field splitting produced by the anisotropy occurs between the states $m = \pm(S-1)$ and the ground state $m = \pm S$:

$$\Omega_0 = (2S-1)D + [S^4 - (S-1)^4]A_4 \simeq 14.8{\rm K} \tag{3.8}$$

When $k_{\rm B}T$ becomes comparable to Ω_0 several related effects occur: (i) the magnetization is no longer given by the Brillouin law and T does not appear in the combination H/T, (ii) $\chi_{\rm T}$ and $\chi_{\rm 3T}$ deviate from the simple equations (3.6)–(3.7) and depend on ψ, and (iii) the normalized

susceptibilities acquire a dependence on T. For classical spins, these effects were studied in reference [Garcia-Palacios 2000c].

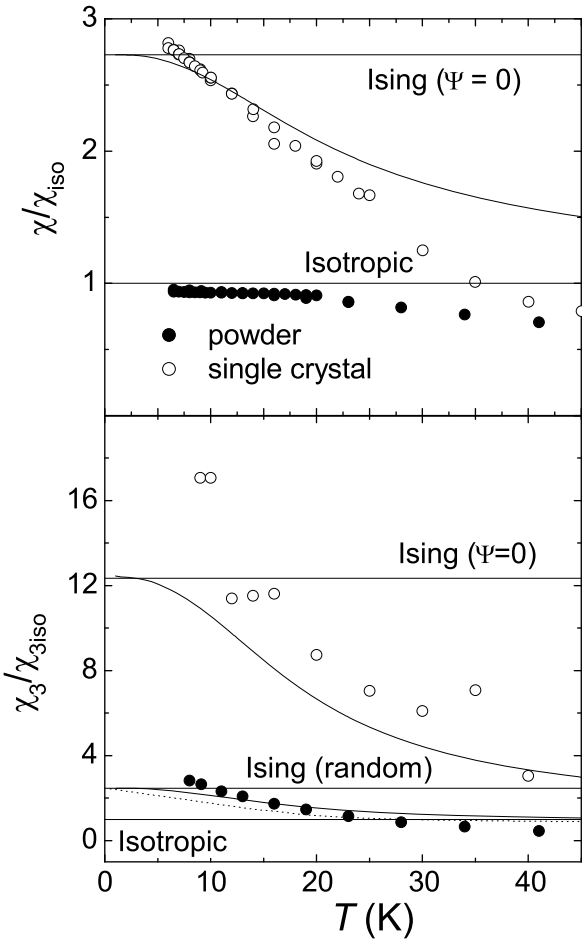

Fig. 3.11. Temperature dependence of the equilibrium linear and nonlinear susceptibilities normalized by their values for isotropic spins (Brillouin limit). Upper panel: linear susceptibility; lower panel: nonlinear susceptibility. Results are shown for a single crystal of Mn_{12} with the field parallel to the anisotropy axis ∘ and a powder sample •. The lines are theoretical results for classical spins (dotted) and quantum spins (solid).

Eventually, in the low temperature limit $k_{\mathrm{B}}T/D \to 0$, only the states $m = \pm S$ are appreciably populated and each molecular spin becomes effectively a two-level system ("spin-up" and "spin-down" states). In this "Ising" limit, χ_{T} and $\chi_{3\mathrm{T}}$ can also be calculated explicitly

$$\chi_{\mathrm{Ising}} = N_{\mathrm{A}} \frac{(g\mu_{\mathrm{B}})^2 S^2}{k_{\mathrm{B}}T} \cos^2\psi \tag{3.9}$$

$$\chi_{3\mathrm{Ising}} = -N_{\mathrm{A}} \frac{(g\mu_{\mathrm{B}})^4 S^4}{3(k_{\mathrm{B}}T)^3} \cos^4\psi \tag{3.10}$$

Here we see that the bare $1/T$ and $1/T^3$ dependences are recovered, so that the normalized susceptibilities become again temperature independent. Comparison of these expressions with equations (3.6)–(3.7) reveals that, for a single crystal at $\psi = 0$, $\chi_{\mathrm{T}}/\chi_{\mathrm{iso}}$ and $\chi_{3\mathrm{T}}/\chi_{3\mathrm{iso}}$ should increase, respectively, by an overall factor of 2.7 [$= 3 \times S^2/S(S+1)$] and 12.3 ($= 15 \times S^4/S(S+1)[S(S+1)+\frac{1}{2}]$), when decreasing temperature. The experimental curves approach indeed these values at low temperatures ($T < 10$ K in Fig. 3.11) although they become even larger. This is probably due to the interactions which, as we have seen, enhance the magnetic response at low temperatures.

Anyhow, these results suggest the measurement of the temperature-dependent reduced susceptibilities as a suitable tool to estimate the anisotropy parameters of superparamagnets. In this respect, the advantage of the nonlinear susceptibility becomes evident when dealing with systems with randomly oriented axes. Then the ratios between the Ising and isotropic limits decrease significantly [compare equations (3.6)–(3.7) with equations (3.9)–(3.10)]. Indeed, $\chi_{\mathrm{T}}/\chi_{\mathrm{iso}}$ becomes nearly T-independent, whereas the reduced nonlinear susceptibility still retains a sizable variation with T (by a factor ~ 2.5). This is experimentally confirmed by measurements on a policrystalline sample (Fig. 3.11) (For random axes the decrease of $\chi_{\mathrm{T}}/\chi_{\mathrm{iso}}$ by the small factor $S^2/S(S+1) \simeq 0.91$ is probably compensated by interaction effects). Thus we see that, contrary to the linear response, $\chi_{3\mathrm{T}}$ keeps information on the anisotropy even for superparamagnets with axes distributed at random. This is the case most often encountered in nanoparticle systems [Pankhurst 1993] but also for single-molecule magnets when deposited on surfaces [Ruiz-Molina 2003] [Cornia 2003] [Cavallini 2003] or inside porous materials [Clemente-León 2003].

The considerations above can be supported by direct diagonalization of the Hamiltonian described in Eq.(3.1). The results (solid lines in Fig. 3.11) exhibit the same trends as the experiments, both for parallel axes and after averaging over random orientations. Full agreement is precluded by the effect of interactions, on the low-T side, and by the population of excited multiplets with $S \neq 10$ at high T, as discussed above.

Before concluding this section, there is an additional feature that deserves to be commented upon. Consider the theoretical behavior of $\chi_{3\mathrm{T}}$ in *classical* spins (using the simplest uniaxial anisotropy $\mathcal{H} = -DS_z^2$ but with a barrier $U = 70$ K, equal to that provided by 3.1 Hamiltonian) also plotted in Fig. 3.11. We see that, although classical and quantum calculations predict the crossover from the isotropic to the Ising limits, the classical susceptibilities are shifted towards lower temperatures. This shift can be seen as a manifestation of the quantum, discrete nature of the energy spectrum of Mn_{12}, since the finite energy gap between the two lowest quantum levels, Ω_0, leads to a faster convergence to the Ising limit.

3.3.2 Dynamical nonlinear susceptibility: quantum nonlinearity

In this section we turn our attention from the equilibrium to the dynamical response. We begin reviewing briefly the behavior of the nonlinear susceptibility χ_3 in the *classical* case. This allows to introduce some basic expressions valid also for quantum superparamagnets. Then, the experimental results for Mn_{12} acetate crystals are presented.

Classical superparamagnets and modelization

The dynamical nonlinear susceptibility of classical spins was theoretically found to be very large and, in contrast to the linear susceptibility, non-trivially sensitive to the spin-bath coupling strength λ [Garcia-Palacios 2000b] [Garcia-Palacios 2004]. The "damping" λ measures the relative importance of the relaxation and Hamiltonian (precessional) terms in the dynamical equations [Brown 1963] [Garcia-Palacios 2000c]. Thus $1/\lambda$ is of the order of the number of precessional turns that the spin executes until it arrives to the energy minima.

The contributions to the nonlinear response of the longitudinal and transverse components of the field are captured by a simple formula involving the low-H expansion coefficients $g_\parallel$ and $g_\perp$ of the relaxation rate [Jonsson 2001a]:

$$\Gamma \simeq \Gamma_0\left[1+\tfrac{1}{2}\left(g_\parallel\xi_\parallel^2+g_\perp\xi_\perp^2\right)\right] \tag{3.11}$$

where $\Gamma_0=\Gamma|_{H=0}$ and $\xi=g\mu_\mathrm{B}SH/k_\mathrm{B}T$. The rate expansion coefficients, $g_\parallel$ and $g_\perp$ are second derivatives of Γ with respect to the external field, and give an idea of the relaxation time τ variation when an small field is applied along a longitudinal or a transverse direction. Note that the relaxation rate Γ should be invariant upon field inversion, leading to the absence of odd powers in the field expansion. The invariance of Γ upon field reflection through the barrier plane yields the vanishing of a mixed term $\propto\xi_\parallel\xi_\perp$ for uniaxial spins.

The expression for the nonlinear susceptibility oscillating with the third harmonic of the field $\chi_3(3\omega)$, extracted from [Garcia-Palacios 2004], follows:

$$\chi_3(3\omega)=-N_\mathrm{A}\frac{(g\mu_\mathrm{B})^4S^4}{3(k_\mathrm{B}T)^3}\left[\frac{\cos^4\psi}{1+3\mathrm{i}\,\omega\tau}\right.$$
$$\left.-\frac{3\mathrm{i}\,\omega\tau}{2(1+\mathrm{i}\,\omega\tau)(1+3\mathrm{i}\,\omega\tau)}(g_\parallel\cos^4\psi+g_\perp\cos^2\psi\sin^2\psi)\right] \tag{3.12}$$

and the equivalent expression for the $\chi_3(\omega)$ oscillating with $\mathrm{e}^{\pm\mathrm{i}\,\omega t}$:

$$\chi_3(\omega)=-N_\mathrm{A}\frac{(g\mu_\mathrm{B})^4S^4}{3(k_\mathrm{B}T)^3}\left[\frac{\cos^4\psi}{1+\mathrm{i}\,\omega\tau}\right.$$
$$\left.-\frac{\mathrm{i}\,\omega\tau}{2(1+\mathrm{i}\,\omega\tau)^2}(g_\parallel\cos^4\psi+g_\perp\cos^2\psi\sin^2\psi)\right] \tag{3.13}$$

This $\chi_3(\omega)$ obtained from the field-dependent susceptibility differs from the $\chi_3(3\omega)$ extracted from the third harmonic of the response to an ac field (at $H=0$). However, Eqs. (3.12) and (3.13) show dependence of both quantities on the parameters under study, $g_\parallel$ and $g_\perp$, is analogous.

Here the Ising approximation for the equilibrium parts has been used (this works fine at temperatures around the blocking temperature $T_\mathrm{b}\sim$ 5 K; see the equilibrium section). The longitudinal part, proportional to $\cos^4\psi$, is maximum at $\psi=0$ (in absolute value); the "transverse"

contribution associated to $g_\perp$ becomes zero both at $\psi = 0$ and $\pi/2$, being maximum at $\psi = \pi/4$. Equation (3.13) shows that the magnitude, signs, and the ω and angular dependences of χ_3 are determined by the competition between the rate expansion coefficients $g_\parallel$ and $g_\perp$. Therefore, measurements of those dependences can provide valuable information on the different contributions to the spin reversal.

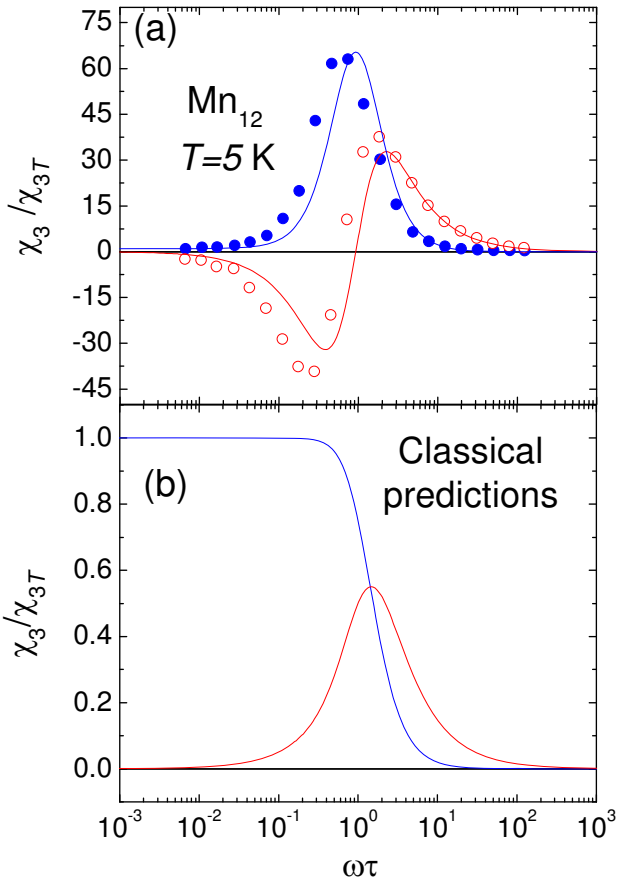

Fig. 3.12. Top panel: Nonlinear susceptibility of a Mn_{12} acetate single crystal measured at $T = 5$ K along the c axis (easy axis for magnetization). The susceptibility data are normalized by the equilibrium χ_{3T} and the frequency is multiplied by the relaxation time τ obtained at the same temperature from frequency-dependent linear susceptibility data [41]. Lines are theoretical predictions that include the presence of quantum tunnelling. Bottom panel: theoretical predictions for the classical case (i.e. no tunnelling).

For classical superparamagnets, where only the thermal activation operates, the rate expansion coefficients are given in the considered low-temperature range by [Garcia-Palacios 2004] [Jonsson 2001a]

$$g_{\parallel} = 1 \,, \qquad g_{\perp} = F(\lambda)/2 \tag{3.14}$$

The positive and small longitudinal rate expansion coefficient $g_{\parallel}$ is an evidence of a classical behavior because the variation of Γ with an small field (in terms of anisotropy field) is governed by the small change in the energy barrier due to the field induced stabilization of the energy levels. $F > 0$ is a function of λ (and T). For strong damping, $F \to 1$, so that $g_{\parallel}$ and $g_{\perp}$ are of the same order. In contrast, in the weak damping regime (governed by the precession), one has $F \propto 1/\lambda$ and $g_{\perp}$ becomes very large, dominating the nonlinear response. Then one can find that the real part $|\chi_3'| \gg |\chi_{3\mathrm{T}}|$ but with $\chi_3'/\chi_{3\mathrm{T}} < 0$ (i.e., the sign is reversed with respect to the equilibrium value). This phenomenology is equivalent to that of the third harmonic nonlinear susceptibility [Garcia-Palacios 2000b] [Garcia-Palacios 2004] since both quantities exhibit similar dependences on λ and ω.

The functional form of the equation (3.13) is quite generic and valid for classical as well as quantum superparamagnets. Thus, the relevant information on the quantum reversal mechanisms will be incorporated by the rate expansion coefficients $g_{\parallel}$ and $g_{\perp}$. Obviously, they could be very different from their classical counterparts (3.14).

Fig. 3.12 displays frequency-dependent measurements of the nonlinear susceptibility of Mn_{12} performed at constant T for ψ =0. They corroborate the result already shown in Fig. 3.10, namely, that χ_3' becomes much larger than its equilibrium value $\chi_{3\mathrm{T}}$ near the blocking temperature. The data measured at fixed T indicate that this is a dynamical effect not caused by magnetic ordering or some kind of "freezing" (interactions also enhance the susceptibilities, but by a much smaller factor). We know that classically one can also have $|\chi_3'| \gg |\chi_{3\mathrm{T}}|$, but here we observe $\chi_3'/\chi_{3\mathrm{T}} > 0$, that is, the peak of the measured nonlinear dynamic susceptibility is *reversed* with respect to the classical prediction.

From equation (3.13) we see that at $\psi = 0$ there is no contribution of $g_\perp$ to χ_3. In addition, the first term in that equation, which has a Debye-type profile, cannot provide $|\chi_3'| > |\chi_{3\mathrm{T}}|$ because $\mathrm{Re}[\chi/(1 + \mathrm{i}x)] \leq \chi$. Therefore, the maximum observed in Fig. 3.12 should be due to the $g_\parallel$ contribution. The height of the susceptibility peak $\chi_3'|_{\max}$ is related with the combination of the relaxation rate coefficients $Q(\psi) \equiv g_\parallel \cos^2\psi + g_\perp \sin^2\psi$.

$$\chi_3'|_{\max}/\chi_{3\mathrm{T}}\big|_{\psi=0} \simeq -\cos^2\psi\, Q(\psi)/4 \tag{3.15}$$

Therefore, the positive sign of the maximum of $\chi_3'(\omega)/\chi_{3\mathrm{T}}$ at $\psi = 0$ entails $Q < 0$. But $Q|_{\psi=0} = g_\parallel$, implying that the relaxation time $\tau = 1/\Gamma$ becomes *longer* as $H_\parallel$ increases. No classical mechanism can account for this; actually, $g_\parallel = 1$ in the classical model, which gives a $\chi_3'/\chi_{3\mathrm{T}}|_{\psi=0}$ smaller than 1 and decreasing with ω (inset of Fig. 3.12), in sharp contrast to the measured χ_3. On the other hand, it is well-established [Friedman 1996] [Hernandez 1996] [Thomas 1996] [Garanin 1997] [Luis 1998] [Würger 1998] that in Mn_{12} the suppression of tunnelling by a longitudinal field *strongly* reduces the relaxation rate (as it breaks the degeneracy between initial "spin-up" and final "spin-down" states, inhibiting the tunnel channels). This effect provides the $g_\parallel$ required, both negative and large, to account for the experimental χ_3 of Mn_{12}. Thus, we see that the known field-suppression of tunnelling shows up in the nonlinear response as a distinctly quantum contribution, which we call here "quantum nonlinearity", with its sign reversed with respect to the classical case.

3.3.3 Orientation effect: Experimental determination of decoherence time

When $\psi > 0$, the quantum contribution coexists with the transverse $g_\perp$ contribution. Still, the data measured at varying ψ and shown in Fig. 3.13 suggest that $\chi_3 \propto \cos^4\psi$ holds approximately. We can check this by plotting the maximum of χ_3' vs. $\cos^4\psi$ (Fig. 3.14). This yields an almost straight line indicating that in Mn_{12} the coefficient $g_\parallel$ overwhelmingly dominates $g_\perp$, which in the classical case embodies the precessional contribution and could be sizable.

Thus $\chi_3(\omega, \psi)$ provides *direct* experimental access to the relaxation-rate expansion coefficients $g_\parallel$ and $g_\perp$, which contain information on the spin relaxation mechanisms. Besides, from the sign of the $\chi_3(\omega)$

peaks we can infer whether the spin reversal is dominated by a classical mechanism or by quantum processes. The consistency of our analysis can be ascertained by comparing the experimentally determined rate Γ (obtained from Debye fits of χ), with the rate reconstructed from the expansion $\Gamma = \Gamma_0(1 + Q\,\xi^2/2 + \dots)$, using the $Q|_{\psi=0}$ extracted from the χ_3' maxima via equation (3.15) ($Q_{\mathrm{Mn_{12}}}|_{\psi=0} \simeq -260$). Fig. 3.15 shows the good agreement between both results in the weak field regime, supporting our interpretation.

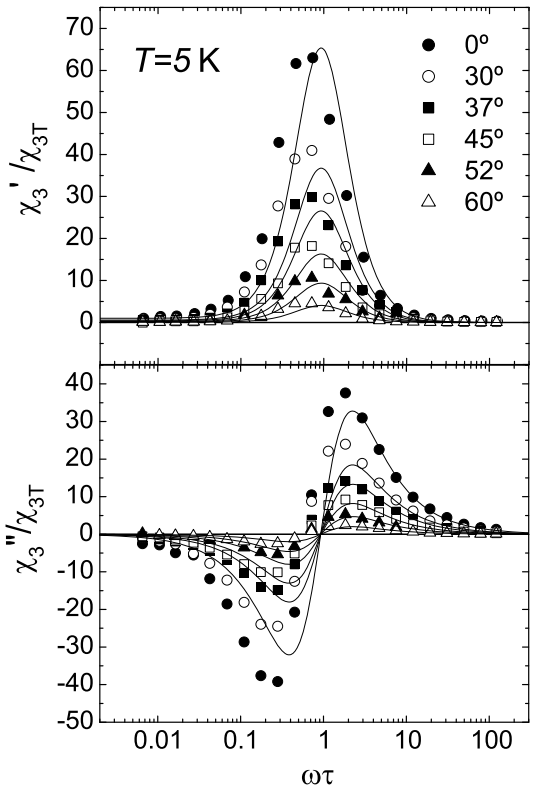

Fig. 3.13. Nonlinear susceptibility vs. frequency at $T = 5$ K. Results are shown for different angles ψ between the applied field and the anisotropy axis. The data are normalized by the equilibrium $\chi_{3\mathrm{T}}$ measured at $\psi = 0$. The relaxation time τ was obtained from ω-dependent linear susceptibility measurements (as those of Fig. 3.9). Upper panel: real part χ_3'; lower panel: imaginary part χ_3''. The lines are obtained using equation (3.13) with $g_\parallel = -260$ and $g_\perp = 0$.

We have seen that the transverse contribution to the nonlinear susceptibility is nearly absent in Mn_{12} (indeed the experiments are consistent with $g_\perp = 0$). Classically, $g_\perp$ incorporates the precessional contribution, which can be large for weak damping $\lambda \ll 1$ [Garcia-Palacios 2000b] [Garcia-Palacios 2004]. Still, as its long τ_0 indicates, Mn_{12} is expected to be quite "underdamped" (in the sense of energy dissipation). Thus, it seems that some other process induces the spin to lose its intrinsic, or coherent, precessional dynamics and appear, when seen through $\chi_3(\omega)$, as "overdamped". We shall try to reconcile these results ($g_\perp \simeq 0$ and long τ_0) invoking an effect of the coupling to the bath, absent in classical physics; *the decoherence*.

Before starting, let us quantify a lower bound for an effective λ of Mn_{12}. To this end we generate $\chi_3(\omega)$ curves using equation (3.13) with the $g_\parallel$ experimentally determined from $\chi_3(\omega)|_{\psi=0}$, while assuming $g_\perp = F(\lambda)/2$ as in classical superparamagnets. In this way we compute $\chi_3'|_{\max}$ vs. $\cos^4\psi$ for several λ and compare with the experimental results (Fig. 3.14). The best agreement is obtained for large λ, which in fact yields small $g_\perp$ and hence almost no $\cos^2\psi \sin^2\psi$ contribution. However, taking into account experimental uncertainties as well as the smaller sensitivity of $g_\perp$ to large λ, gives a lower bound of $\lambda \gtrsim 0.01$.

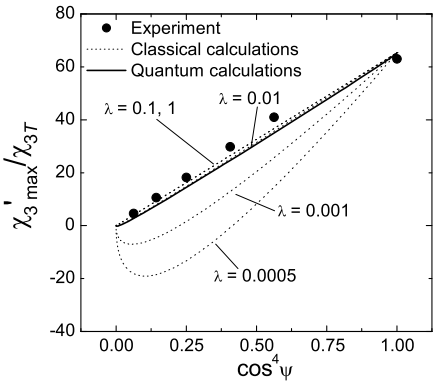

Fig. 3.14. Evolution of the maximum of $\chi_3'(\omega)$ with the angle ψ of the applied field at $T = 5$ K. The symbols are the experimental results. The dashed lines are obtained from equation (3.13) using the experimentally determined $g_\parallel = -260$ and the classical transverse contribution $g_\perp = F(\lambda)/2$ computed for different values of the phenomenological damping constant λ. The solid line corresponds to theoretical calculations with a Pauli quantum master equation.

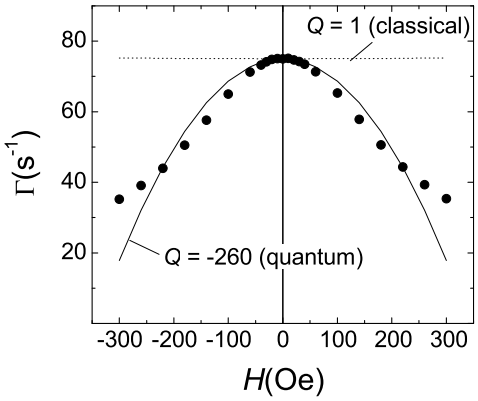

Fig. 3.15. Relaxation rate of Mn_{12} at $T = 5$ K as a function of the field applied along the anisotropy axis ($\psi = 0$). The symbols are the Γ's obtained from Debye fits of $\chi(\omega, H)$. The lines are calculated as $\Gamma = \Gamma_0(1+Q\,\xi^2/2)$, where $\xi = g\mu_B S H_\parallel / k_B T$ and Q comes from the maximum of $\chi_3'(\omega)$ via equation (3.15). The classical prediction ($Q = 1$) is shown for comparison.

In the classical equations of motion the damping parameter λ is a measure of the relative weights of their relaxation and precessional terms. It can then be expressed as the Larmor precession period $\tau_L = 2\pi/\gamma H_A$ (in the anisotropy field H_A; $\gamma = g\mu_B/\hbar$) divided by some timescale of relaxation. For the latter we can use the classical prefactor in the Arrhenius law [Brown 1963] [Garcia-Palacios 2000c]

$$\tau_0 = \frac{1}{\lambda\gamma H_a}\sqrt{\frac{\pi}{4\,\sigma}}\left(1 + \frac{1}{\sigma} + \cdots\right) \tag{3.16}$$

where the reduced anisotropy barrier is $\sigma = U_0/k_B T$. In our experiments at $T = 5$ K we have $\sigma \simeq 14$, whence

$$\lambda \simeq 0.04 \times \tau_L/\tau_0 \tag{3.17}$$

Experimentally $\tau_0 \sim 3 \times 10^{-8}$ s in Mn_{12}. Its anisotropy field can be obtained from magnetization measurements (along the hard plane) or from the ground-state transition frequency $\Omega_0/\hbar$ [equation (3.8)], getting $\tau_L \simeq 3$–4×10^{-12} s. This gives $\tau_L/\tau_0 \sim 10^{-4}$ and hence an effective $\lambda \sim 10^{-6}$, many orders of magnitude smaller than the lower bound $\lambda \gtrsim 0.01$ extracted from χ_3.

The estimation of $\tau_{\rm L}/\tau_0$ is in agreement with the mentioned underdamped character of Mn_{12} (in the sense of long-lived levels). However, in case of $g_\perp$ having some precession-type contribution akin to $F(\lambda)$, the above $\lambda \propto \tau_{\rm L}/\tau_0$ would not be the parameter entering there. Otherwise a giant $g_\perp \propto 1/\lambda$ would dominate χ_3 (leading to $\chi_3'/\chi_{3T} < 0$ and $\chi_3'|_{\max}$ not proportional to $\cos^4\psi$), which is clearly not seen in the experiments. Still, it might be that, instead of the damping, some other timescale limits the precession; as this is a type of coherent dynamics, we can call such time a decoherence time $\tau_{\rm dec}$. This should replace τ_0 in the effective $\lambda \propto \tau_{\rm L}/\tau_{\rm dec}$. To get a λ consistent with the lower bound $\lambda \gtrsim 0.01$ obtained from χ_3, the time $\tau_{\rm dec}$ should be far shorter than $\tau_0 \sim 10^{-8}$ s, actually $\tau_{\rm dec} \sim 1\text{–}1.5 \times 10^{-11}$ s.

Approximate quantum treatment

A critical assessment of the considerations above is in order before proceeding. They have been based on stretching the classical idea that $g_\perp$ should include some precessional-type contribution. Further, they assume that this contribution is controlled by a parameter relating the Larmor period with some scale limiting the time allowed to the spin to precess (either by damping or by some loss of coherence). By definition, however, $g_\perp$ accounts for the effects of $H_\perp$ on the relaxation rate [equation (3.11)]; besides, $\chi_3(\omega)$ gives *direct* access to $g_\parallel$ and $g_\perp$. Then, one would expect that a pure quantum approach for Γ, including the bath coupling and coherent dynamics (tunnel and precession) could account for the experimental χ_3 without recourse to classically preconceived notions.

An exact quantum treatment, unfortunately, is difficult because one must deal with the full density-matrix equation including the intrinsic (Hamiltonian) dynamics plus the effects of the bath (damping and decoherence). However, as this can be handled in various limit cases, we shall attempt a discussion based on the corresponding partial solutions for the quantum Γ, with the hope of shedding some light on the physical origin of the results.

The dominant terms that enter the relaxation rate describing quantum tunneling via a pair of nearly degenerate states $|\pm m\rangle$ have a Lorentzian shape as a function of the *longitudinal* bias $\xi_m = 2mg\mu_{\rm B}H_\parallel$ [Leuenberger 1999][Tupitsyn 2002]

$$\Gamma \simeq 2\Gamma_m \frac{\Delta_m^2}{\xi_m^2 + \underbrace{\Delta_m^2 + \hbar^2\Gamma_m^2}_{w_m^2}} \exp(-U_m/k_{\rm B}T) \tag{3.18}$$

Here Γ_m is the probability of decaying to other levels via the absorption or emission of phonons (i.e., it is approximately $1/\tau_0$), Δ_m is the tunnel splitting of the pair $|\pm m\rangle$ induced by terms not commuting with S_z in the Hamiltonian, and U_m is the energy of the levels measured from the ground state, i.e. $U_m = \varepsilon_m - \varepsilon_S$. The width of the Lorentzian introduced [Tupitsyn 2002], $w_m^2 = \Delta_m^2 + \hbar^2\Gamma_m^2$, interpolates between the results that can be obtained in the two limit cases of (i) large coupling $\hbar/\tau_0 \gg \Delta_m$ [Garanin 1997], where $w_m \simeq \hbar/\tau_0$, and (ii) weak coupling $\hbar/\tau_0 \ll \Delta_m$ [Luis 1998], in which $w_m \simeq \Delta_m$.

Performing the second $H_\perp$-derivative of equation (3.18) gives the corresponding $g_\perp$. For the parameters of Mn_{12} it results that the main contribution at zero longitudinal bias comes from the derivative of the quotient Δ_m^2/w_m^2

$$g_\perp \equiv \frac{1}{\Gamma_0}\frac{\partial^2\Gamma}{\partial H_\perp^2}\Big|_0 \simeq \frac{2}{(\Delta_m/w_m)}\frac{\partial^2}{\partial H_\perp^2}(\Delta_m/w_m) \tag{3.19}$$

Now, for large coupling $\hbar/\tau_0 \gg \Delta_m$, we have $w_m = \hbar/\tau_0$. Then the relaxation rate depends on the ratio between τ_0 and the tunneling time $\hbar/\Delta_m$. A transverse field eases the tunneling and significantly increases Δ_m, and hence Γ. As Γ is then quite sensitive to $H_\perp$, we can have large $g_\perp$, in analogy with the classical situation. On the contrary, when $\hbar/\tau_0 \ll \Delta_m$, we have $w_m \simeq \Delta_m$ and hence $\Delta_m^2/w_m^2 \simeq 1$. Then the rate becomes quite insensitive to Δ_m (and hence to $H_\perp$), leading to a small $g_\perp$.

In Mn_{12}, where $\hbar/\tau_0 \sim 0.2$ mK, both situations are possible. The reason is the exponential increase of the tunnel splitting Δ_m with decreasing $|m|$, going from the sub-nanoKelvin regime for the ground levels $m = \pm S$ to some tenths of K for $|m| \lesssim 2$. Therefore, the relation between $\hbar/\tau_0$ and Δ_m depends on which tunnelling path (i.e., which pair $\pm m$) gives the dominant contribution to Γ. If tunnelling proceeds via the deep levels, where $\hbar/\tau_0 \gg \Delta_m$, we would find a large $g_\perp$. In contrast, when tunnelling occurs through the excited levels, one has $\hbar/\tau_0 \ll \Delta_m$ and hence small $g_\perp$.

At this point it is important to bring into the discussion the effect of environmental bias fields (due to intermolecular dipolar interactions or the hyperfine interaction with the nuclear spins of the Mn ions).

They produce a distribution of bias ξ whose typical width is of a few tenths of K (of the order of the Curie-Weiss θ). These bias fields enter as $\Delta_m^2/(\xi_m^2 + w_m^2)$ in the rate expression (3.18), replacing the bare Δ_m^2/w_m^2 and supressing tunneling when $w_m \ll \xi_m$ (Fig. 3.2). Taking into account the order of magnitude of ξ_m, the bias effectively blocks tunneling via the large $|m|$ (deep) channels, those that would provide large $g_\perp$. Tunneling becomes possible only for $\Delta_m > \xi_m$, but for those upper levels $\hbar/\tau_0 \ll \Delta_m$, leading to small $g_\perp$, in agreement with the experiments.

We can support this picture with direct numerical calculations. An approximate (Pauli) quantum master equation, which works well when tunneling occurs under weak damping conditions and that incorporates the effects of environmental bias fields, was used to study several problems in Mn_{12} [Luis 1998] [Luis 2002a] [Fernandez 1998]. We have implemented it to address the nonlinear response problem, mimicking the experimental protocol and calculating χ' and χ'' vs. H. Results are shown in Fig. 3.14 (solid line). They account well for the measured nonlinear susceptibility; in particular, for the nearly $\cos^4\psi$ dependence of χ_3 associated to small $g_\perp$.

We would like also to provide a physical picture in the limit cases discussed ($\hbar/\tau_0$ much larger or smaller than Δ_m). To this end, let us discuss the total energy of the spin plus the bath, treating their interaction perturbatively. Then, time-dependent perturbation theory leads to the celebrated *time-energy* "uncertainty" relation. In particular, for $t \gtrsim \hbar/\Delta E$ the dominant transitions are those conserving the total energy. On the other hand, for a spin in a $|m\rangle$ state, which is not an exact eigenstate of the Hamiltonian, the energy uncertainty is of the order of the tunnel splitting Δ_m. Well, consider now a transition to such an $|m\rangle$ state; although the spin could at short times remain there, for times longer than $\tau_\Phi \equiv \hbar/\Delta_m$ it will have to become an energy eigenstate. Then the wavefunction consists of a superposition of spin-up and spin-down states $|\pm m\rangle$, delocalized between both sides of the barrier.

We can now revisit the limit cases discussed above. Consider first the strong-coupling case $\hbar/\tau_0 \gg \Delta_m$. For times shorter than the decay τ_0, the time-energy uncertainty allows the existence of superpositions of energy eigenstates, which can be localized on either side of the barrier ($\sim |\pm m\rangle$). These wavepackets may exhibit Hamiltonian dynamics including tunnel oscillations and precession. Under these conditions the rate Γ is quite sensitive to Δ_m, as it controls the probability for the

spin to have tunneled before a time τ_0. It is this sensitivity to Δ_m, and in turn to $H_\perp$, which can lead to large $g_\perp$.

When, by contrast, $\hbar/\tau_0 \ll \Delta_m$ the "semiclassical" wavepacket around $|m\rangle$ delocalizes in the tunneling time $\tau_\Phi = \hbar/\Delta_m$, evolving towards an energy eigenstate due to the uncertainty principle. Then, there is neither coherent oscillation between $|m\rangle$ and $|-m\rangle$, nor precession of the (averaged) transverse components, since this is a stationary state. The dependence on Δ_m (and hence on $H_\perp$) is then minimized, as the wavefunction is already delocalized between the spin-up and spin-down states, leading to small $g_\perp$ values. Note that under these conditions the coherent (precessional) dynamics is not limited by the level lifetime τ_0 but by the much shorter "decoherence" time to attain a diagonal density matrix. Therefore, the $\tau_{\rm dec}$ introduced heuristically above can be identified with this $\tau_\Phi = \hbar/\Delta_m$. For $|m| = 2$, 4, we have $\Delta_m \sim 0.7$–0.02 K, which give $\tau_\Phi \sim 10^{-11}$–4×10^{-10} s. These values are consistent with the estimation, based on $\chi_3(\omega)$, of the $\tau_{\rm dec}$ required to get $\lambda \sim 0.01$ (which yielded $\tau_{\rm dec} \sim 10^{-11}$ s). Although dipole-dipole interactions between molecular spins could in principle contribute to decoherence, experimental evidence shows that the broadening of the Mn_{12} excited levels is predominantly homogeneous (see [Friedman 1998] and [Wernsdorfer 1999]). Therefore, the decoherence mechanism considered here is probably giving the dominant contribution.

3.3.4 Applied field effect: classical to quantum relaxation crossover

In recent sections, we showed that in Mn_{12}, near zero field, resonant tunnelling via excited states yields a contribution to the *nonlinear* susceptibility that makes it qualitatively different from the classical curves. Here we extend the experimental study to the case where finite longitudinal dc fields H_z are applied. To determine the nonlinear susceptibility, the standard method of measuring the harmonics ($\chi_2(2\omega)$ and $\chi_3(3\omega)$) of the response to an oscillating field $h_0 \cos(\omega t)$ has been employed (details in section 3.2).

Fig. 3.16 show the $\chi_3(3\omega)$ behavior when a field is applied. The fields, both dc and ac, were applied *parallel* to the common anisotropy direction $\boldsymbol{z}$ of the clusters. The low signal-to-noise ratio (in spite of gluing several single crystals) prevented from obtaining good χ_3 data, but we can observe in Fig. 3.16 that a small applied field "switches off" the tunnelling reversal, and the "quantum nonlinearity" falls until

arriving to the small classical limit (within experimental uncertainties). As a conclusion the thesis that enormous χ_3 is due to spin tunnelling is reinforced. If we continue increasing the field we can "switch on" this phenomenon again, as we can arise new crossing between energy levels. Fortunately, nice curves for χ_2 were obtained, which is the leading nonlinear term when a bias field is applied.

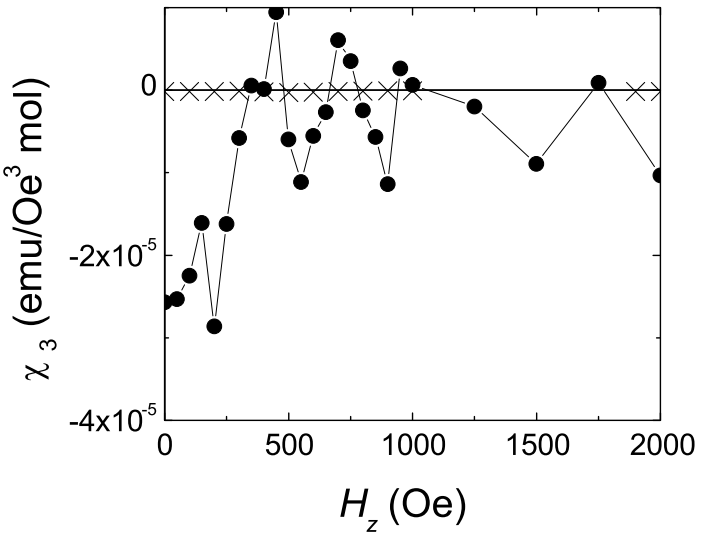

Fig. 3.16. Nonlinear susceptibility $\chi_3(3\omega)$ of a sample of oriented single crystals of Mn_{12} acetate as a function of the external bias at $T = 8$ K: Dots: $\chi_3(3\omega)$ measured at $\omega/2\pi = 2$ kHz; Crosses: equilibrium $\chi_{3\mathrm{T}}(3\omega) = (d^2\chi_\mathrm{T}/dHz^2)/6$.

The so-measured linear and nonlinear susceptibilities of Mn_{12} at $T = 8$ K are shown in Fig. 3.17. The frequency-dependent χ_1 shows maxima near the resonant fields, where it approaches the equilibrium χ_1^{eq}. Fig. 3.17 also displays (panel b) the second component measured at $\omega/2\pi = 2$ kHz. The *equilibrium* nonlinear susceptibilities, also shown, were obtained differentiating χ_1^{eq}, measured at the lowest frequency $\omega/2\pi = 1$ Hz.

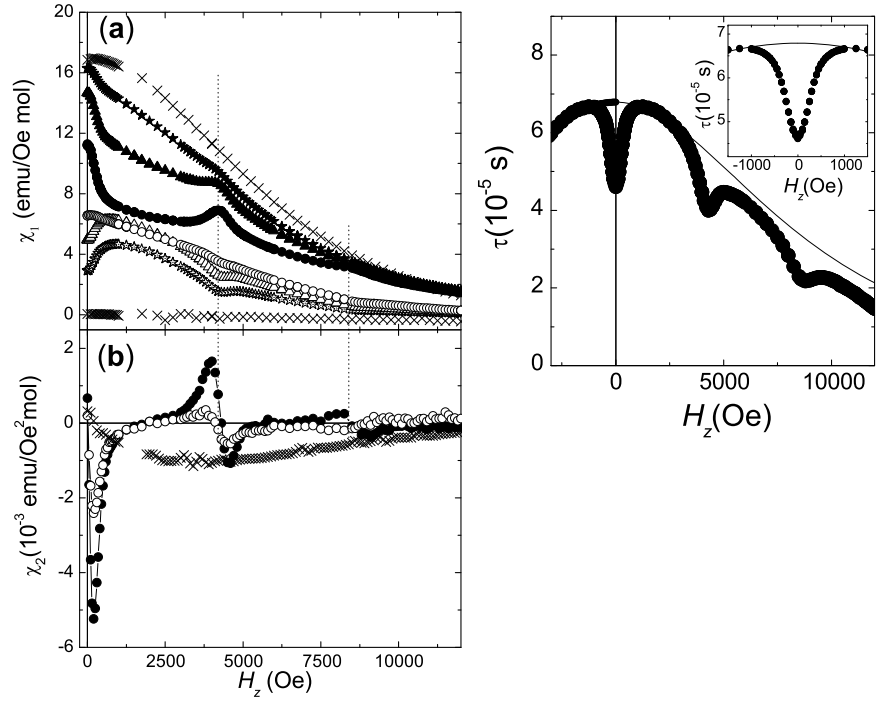

Fig. 3.17. Upper panel: linear susceptibility of Mn_{12} measured at $T = 8$ K versus a magnetic field applied parallel to the anisotropy axis. ×, $\omega/2\pi = 1$ Hz (∼equilibrium); ⋆, 500 Hz; △, 1 kHz; •, 2 kHz. Solid symbols, real parts; open symbols, imaginary parts. Lower panel, second harmonic susceptibility measured at the same temperature. • and ○, $\chi_2'(2\omega)$ and $\chi_2''(2\omega)$ at 2 kHz; ×, equilibrium $\chi_2^{\rm eq} = (\mathrm{d}\chi_1^{\rm eq}/\mathrm{d}H_z)/2$. LEFT: Relaxation time τ, as obtained from $\chi_1''/\omega\chi_1'$ [see equation (3.20)] as well as calculated for classical spins (line) [Brown 1963]. Dotted vertical lines mark the resonant fields $H_1 \simeq 4200$ Oe and $H_2 = 2H_1$.

Fig. 3.17 shows that the magnitudes of the harmonics increase in the neighborhood of the resonant fields $H_0 = 0$, H_1 and H_2, where states of opposite S_z are degenerate and tunnel channels open. Besides, in contrast with the behavior of χ_1, both χ_2 and χ_3 become, near H_0, larger than $\chi_2^{\rm eq}$ and $\chi_3^{\rm eq}$. Thus, when resonant tunnel sets on, the multiharmonic response of these molecular clusters is enhanced.

In order to better understand these results, simple expressions for the susceptibilities have been derived. This was done by solving [Garcia-Palacios 2004] a simple system of balance equations for the net population of the two anisotropy potential wells:

$$\chi_1(\omega) = \chi_1^{\rm eq}\frac{1}{1+{\rm i}\,\omega\tau} \tag{3.20}$$

$$\chi_2(2\omega) = \chi_2^{\rm eq}\frac{1}{1+2{\rm i}\,\omega\tau} - \chi_1^{\rm eq}\frac{{\rm i}\,\omega\tau'}{(1+{\rm i}\,\omega\tau)(1+2{\rm i}\,\omega\tau)} \tag{3.21}$$

$$\begin{aligned}\chi_3(3\omega) = \chi_3^{\rm eq}\frac{1}{1+3{\rm i}\,\omega\tau} - \chi_1^{\rm eq}&\frac{\frac{1}{2}{\rm i}\,\omega\tau''}{(1+{\rm i}\,\omega\tau)(1+3{\rm i}\,\omega\tau)}\\ &- \chi_2^{\rm eq}\frac{2{\rm i}\,\omega\tau'}{(1+2{\rm i}\,\omega\tau)(1+3{\rm i}\,\omega\tau)}\\ &-\chi_1^{\rm eq}\frac{2{\rm i}(\omega\tau')^2}{(1+{\rm i}\,\omega\tau)(1+2{\rm i}\,\omega\tau)(1+3{\rm i}\,\omega\tau)}\end{aligned} \tag{3.22}$$

The equilibrium $\chi_k^{\rm eq} = ({\rm d}^k M_z/{\rm d}H_z^k)/k!$ are the derivatives of the magnetization curve, while τ, τ', and τ'' are the relaxation time and its corresponding field-derivatives (all evaluated at the working field H_z). At $H_z = 0$ we have $\chi_2^{\rm eq} \equiv 0$ [since $M_z(H_z) = -M_z(-H_z)$] as well as $\tau' \equiv 0$ [from $\tau(H_z) = \tau(-H_z)$]. Then $\chi_2(2\omega) \to 0$ as $H_z \to 0$, while in χ_3 the last two terms vanish. Therefore these equations extend the expressions (3.12) and (3.13) to nonzero bias fields.

The first equation (3.20) gives the ratio $\chi_1/\chi_1^{\rm eq} < 1$. Besides χ_1 depends, via the product $\omega\tau$, on how far the spins are from thermal equilibrium. By contrast, the nonlinear susceptibilities χ_2 and χ_3 include also terms depending on τ' and τ'', i.e., on how sensitive τ is to changes of H_z. As a result, the relaxation time does not simply "renormalize frequency", as occurs with χ_1, but it modifies the magnitudes of the nonlinear responses. Extending the arguments we used for $H_z = 0$ [Luis 2004] [Lopez-Ruiz 2005], it is this property that makes the quantum χ_2 and χ_3 qualitatively different from the classical ones.

According to equation (3.20), the relaxation time of the magnetic clusters can be estimated from χ_1 as $\chi_1''/\omega\chi_1'$ where χ_1' and χ_1'' are the real and imaginary components of the first harmonic. This τ is shown in the inset of Fig. 3.17. The data show minima at the resonant fields, in contrast with the monotonous behavior of τ in classical spins. At zero field and finite temperatures, Mn_{12} spins are able to tunnel between those excited magnetic states ($m \sim 2$–4) for which such process is not blocked by the internal bias caused by dipolar and hyperfine interactions [Luis 1998]. This results in a effective barrier reduced by a

few magnetic levels, say $U \sim \varepsilon_{\pm 3} - \varepsilon_{\pm S}$, so that the thermo-activated relaxation gets faster ($\delta U \sim 4$ K). Tunnelling is however suppressed as soon as the external bias $\xi_m = 2g\mu_{\rm B} m H_z$ exceeds the tunnel splitting Δ_m, slowing down the relaxation (the full barrier has to be overcome). As a result, τ is minimum at zero field, whence $\tau'' > 0$, while τ' changes sign from < 0 to > 0.

The same features are repeated every time the field brings magnetic levels again into resonance $H_n = n \times (2g\mu_{\rm B})D$. Therefore, tunnelling becomes, at any crossing field, an additional source of nonlinear response via τ' and τ''. Besides, taking into account the signs of the τ derivatives and equations (3.20) and (3.22), one sees that the sign of the nonlinear susceptibilities can be reversed with respect to the classical ones. In the classical model τ decreases monotonically with increasing field [Brown 1963] (see Fig. 3.17 right), giving $\tau'' < 0$ and $\tau' < 0$ for any H_z.

It is interesting that both behaviors can be obtained in our case just varying the external field. For fields between resonances, tunnelling becomes blocked for *all* states and the spins reverse by thermal activation over the total ("classical") energy barrier. But when a crossing field is approached, the strong nonlinearity of τ shows up with its characteristic contribution to the nonlinear susceptibilities via τ' and τ''.

To confirm this interpretation, the nonlinear responses from equations (3.20)–(3.22) have been computed incorporating the relaxation time obtained by solving a Pauli quantum master equation [Luis 1998].

Fig. 3.18 shows how the bias can trigger the system to display those quantum nonlinear responses, near the resonant fields, while recovering a classical-like behavior for fields between them. This is due to the smallness of the tunnel splitting of the relevant states for our Mn_{12} sample: $\Delta_4 \sim 2 \times 10^{-2}$ K and $\Delta_2 \sim 7 \times 10^{-1}$ K. This means that the fields required to block tunnelling via these levels, albeit relatively small (~ 20 Oe and 1000 Oe, respectively), give rise to relatively large changes in τ, and hence, large τ' and τ''. In the "classical" regime, by contrast, the scale of change of τ is determined by the anisotropy field $H_{\rm A} \sim (2S-1)H_1$. As this is very large in Mn_{12} ($\simeq 95$ kOe), one has a comparatively slow decrease of τ with H_z. This corresponds to small values of the derivatives τ' and τ'' and in turn of the classical (non-tunnel) nonlinear susceptibilities.

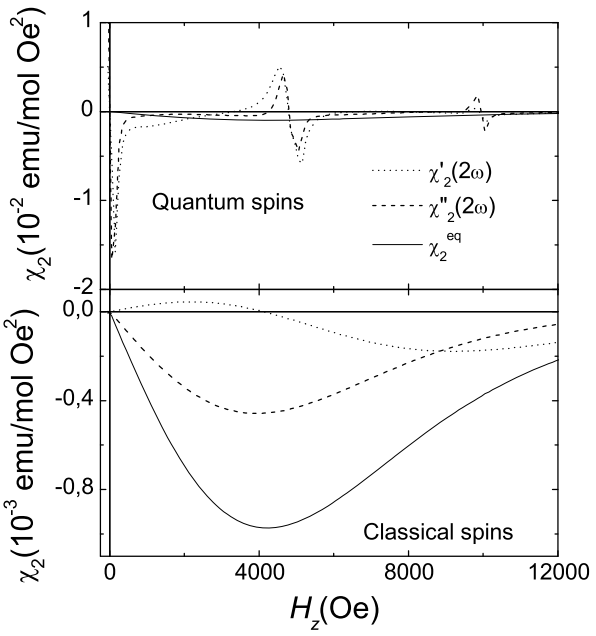

Fig. 3.18. Theoretical calculations of $\chi_2(2\omega)$ [equation (3.21)] for quantum and classical spins. In the latter case, Brown's classical formula for τ [Brown 1963] is used and the former τ was calculated by solving Pauli's quantum master equation (described in [Luis 1998]). Notice the difference in the χ_2 axis scale (the solid equilibrium curve is the same in both panels).

It is also worth mentioning that the τ vs H_z resonances are further broadened by dipolar and hyperfine interactions [Luis 1998]. In fact, the master-equation calculations tell us that tunnelling via lower lying states would give rise to enormous spikes in χ_2 ($\Delta_{10} \sim 7 \times 10^{-10}$ K for the ground state). However, these peaks are also very fragile, being easily suppressed by environmental bias fields and therefore not observed experimentally.

3.4 Nonlinear susceptibility of "fast" Mn_{12} molecules: Mn_{12} benzoate

Why fast?

Inside a Mn_{12} molecular crystal, two kinds of Mn_{12} magnetic cores can be detected: fast relaxing (FR) molecules (with lower blocking temperature, $T_b = 2$ K) and slow relaxing (SR) molecules (with higher blocking temperature, $T_b = 5$ K). Experimentally, the imaginary ac susceptibility (χ'') measured at a single frequency reveals two peaks at two different temperatures.

In the already studied Mn_{12} acetate crystals (Mn_{12}Ac), about 96% of molecules in the crystal are "slow". When the acetate ligand is replaced under certain conditions by benzoate ligand (see the chemical route in Fig. 3.5), a different crystallographic ordering induces crystals where up to 98% of molecules are "fast". Differences between the two cores lie on Mn number 7. In a benzoate crystal (Mn_{12}Bz), it seems that ligands near Mn number 6 and Mn number 7 in the molecules receive a steric pressure from the crystallization solvent molecules (benzoic acid) and the structural flexibility in this Mn_{12}-core region results in the unusual distortion at Mn number 7 [Takeda 2002]. In this case, Mn number 7 elongated octahedron environment is not parallel, but perpendicular to molecular axis and this unusual distortion results in a weaker anisotropy and a tilting of the easy axis with respect to the molecular axis (Fig. 3.4).

Linear response: Determination of the anisotropy axes orientations

In order to evaluate the components of nonlinear χ_3 response, it is very important to study the orientation of the easy axes. Let us, thus, define the angles that parameterize the following measurements: ψ_C is the angle between the applied field and the c axis. ψ_1 and ψ_2 are the angles between the applied field and the easy axes of the S1 and S2 sublattices respectively.

The two easy axes from the different sublattices of the Mn_{12} molecules inside the benzoate crystal (see Fig. 3.4) are reported [Takeda 2002] to be on ab plane and separated by $\psi_2 - \psi_1 = 74^o$. Assuming the reported easy axes orientation, we expect that the linear susceptibility may show a minimum when the ac magnetic field is perpendicular to the ab plane. We can extract the transversal component $\chi_\perp$ rotating the sample a Θ angle which defines the deviation of the

crystallographic c axis with respect to the applied field. The inset of Fig. 3.19B shows that this minimum is located at $\Theta \simeq -7^{\rm o}$. This means that $\Theta \simeq \psi_{\rm C} + 7^{\rm o}$. Due to orientation experimental uncertainty $\Theta \simeq -7$ is the angle that makes $\psi_{\rm C} \simeq 0$ supposing S1 and S2 perfectly oriented inside the ab plane. The expected $\chi_\perp$ reads:

$$\chi_\perp = N_{\rm A} \frac{gS\mu_{\rm B}}{H_{\rm A}} \tag{3.23}$$

where $H_{\rm A}$ is the anisotropy field $H_{\rm A} = (2S-1)D/(g\mu_{\rm B})$, $g = 2$, $S = 10$ and $D = 0.45$ K (extracted from [Takeda 2002]). Experimentally we observe that the value of this minimum susceptibility is higher than the predicted $\chi_\perp$, and unexpectedly, temperature dependent (as is shown in Fig. 3.19A). Thus, experimental data can be described as an addition of the perpendicular and a temperature-dependent "contamination" from the parallel susceptibility as:

$$\chi \simeq \chi_\perp + (C/T)\cos^2(90 - \psi_{\rm C}) \tag{3.24}$$

From the fit we can extract both $\chi_\perp$ and $\psi_{\rm C}$ (C=143 emu/mol was extracted from the Curie law). The numerical value of $\chi_\perp$ is in good according with the value extracted from inset of Fig. 3.19A. The theoretical fit gives us a deviation of $\psi_{\rm C}$= 9$^{\rm o}$ with respect to the ab plane.

The field dependence of χ (Fig. 3.19B) also indicates a non-perfect perpendicular orientation of the field with respect to the easy axes. In this case, the susceptibility can be described as an addition of a constant perpendicular component which should be almost independent of H, plus the field-dependent parallel contribution. The contribution $\chi_\parallel$ depends on field and orientation $\psi_{\rm C}$ as:

$$\chi_\parallel = N_{\rm A} \frac{g^2\mu_{\rm B}^2 S^2}{k_{\rm B}T} \frac{1}{\cosh^2 \xi_\parallel} \qquad \xi_\parallel = \frac{g\mu_{\rm B} HS\cos(90 - \psi_{\rm C})}{k_{\rm B}T} \tag{3.25}$$

The best fit of the experimental data (it is indicated in red line in Fig. 3.19B) provides a $\psi_{\rm C}$= 10.4$^{\rm o}$ in good agreement with the previous determination. As a conclusion, in contrast to the model proposed in [Takeda 2002], our data suggest that the easy axes of the molecules of the sublattices are approximately tilted 10$^{\rm o}$ with respect the ab plane.

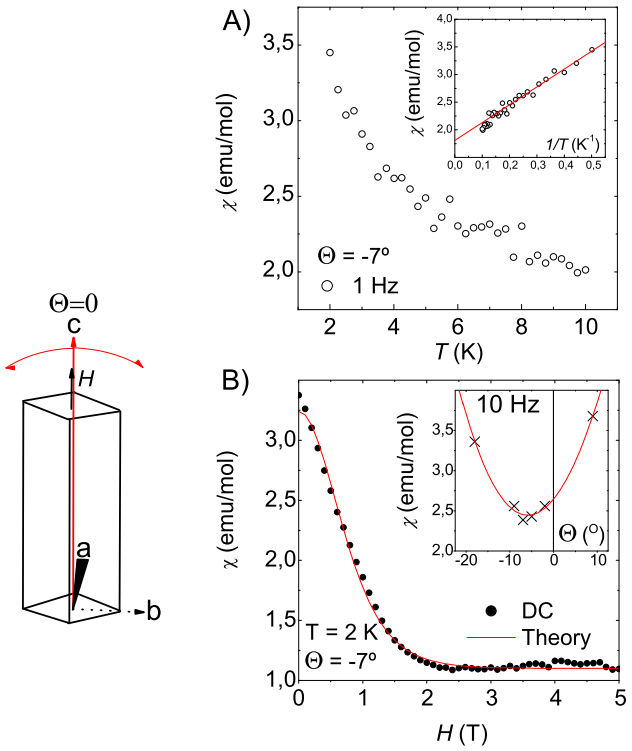

Fig. 3.19. A: Linear susceptibility vs. temperature measured at -7°. Inset: Linear susceptibility vs the inverse of temperature. The value in the origin reveals the value of $\chi_\perp$. B: Linear ac susceptibility vs. filed measured at $T = 2$ K in the position of minimum (-7°). Line is the theoretical prediction from equation 3.25. Inset: Linear susceptibility vs Θ (It reveals the angle in which χ is minimum). The line is a guide to the eye.

Orientation of the easy axes on ab plane

We can obtain additional valuable information about the orientation of easy axes studying the angular dependence of the linear susceptibility within the *ab* plane. Measurements were performed on a single crystal glued to the rotating sample holder shown in Fig. 3.7. A schematic picture is represented in Fig. 3.20. Let us, for convenience, introduce the angle Θ to represent the susceptibility measurements. The effect of the tilt out of the *ab* plane was estimated to reduce the values by a 3% and consequently was neglected in the following analysis.

The angular dependence of χ can be fitted following a simple formula

$$\chi = \frac{1}{2}\left(\chi_{\parallel}\cos^2\psi_1 + \chi_{\perp}\mathrm{sen}^2\psi_1\right) + \frac{1}{2}\left(\chi_{\parallel}\cos^2\psi_2 + \chi_{\perp}\mathrm{sen}^2\psi_2\right) \quad (3.26)$$

where the first bracket corresponds to S1 sublattice contribution and the second bracket to S2 contribution. The parallel contribution was calculated as Eq. (3.6) and the perpendicular contribution was calculated from Eq. (3.23).

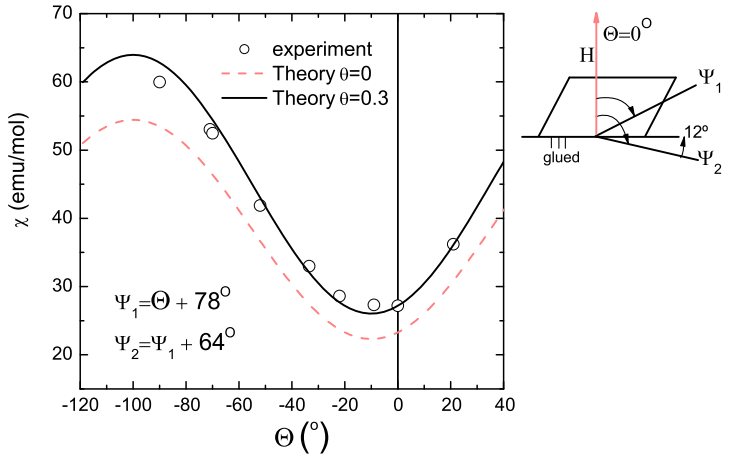

Fig. 3.20. Orientation dependence of the linear susceptibility by rotating on the ab plane (See the schematic picture). Measurements were performed at $T = 2$ K and $\omega/2\pi = 1$ Hz. Red line is the theoretical prediction assuming no interactions. Black line assumes $\theta = 0.3$ K, which is consistent with the Curie-Weiss representation.

Results are shown in Fig 3.20. The main conclusion is that the easy axes of the two sublattices S1 and S2 lie 10° closer that what was estimated in [Takeda 2002]. This conclusion is univocally supported by the difference in height between minimum and maximum. Also an experimental displacement of 10° in Θ is observed, probably due to a crystal orientation error. With respect the prediction of the equation 3.26, the experimental data show higher values due to interactions. If we introduce a finite $\theta = 0.3$ K, extracted in an independent way from the fit of a Curie-Weiss law to the linear susceptibility (see inset of Fig. 3.22), the curves account very well for the experimental data.

The Debye law

The frequency dependence of the linear response for a single crystal of Mn_{12}Bz is shown in Fig. 3.21. Analogously to acetate compound, it follows a conventional Debye law in which the relaxation time τ is reduced when a magnetic field is applied. However, comparing with acetate crystals, a lower increment in the relaxation time τ is observed with increasing H.

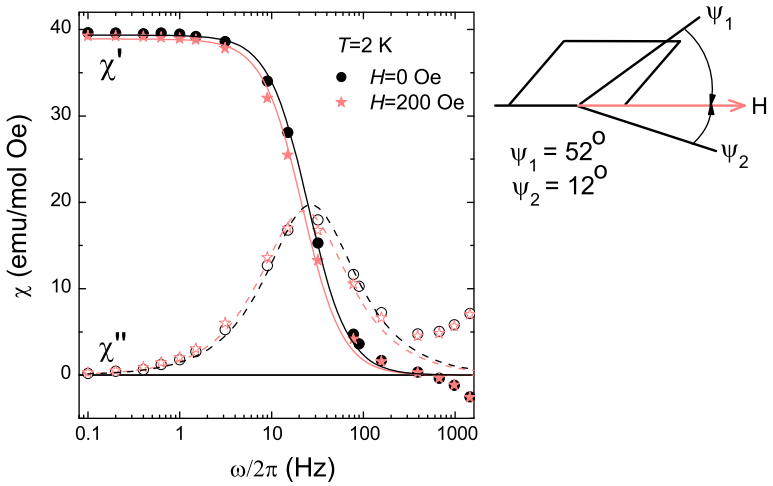

Fig. 3.21. Magnetic susceptibility vs. frequency measured at $T = 2$ K on ab plane. Field was applied between the easy axes of the sublattices S1 and S2. $\psi_1 = 12^o$ and $\psi_2 = 52^o$ were the angles with respect the easy axes of sublattice S1 and S2 respectively. Results are shown at zero bias field (circles) and at $H = 200$ Oe (stars). Solid symbols are for the real part (in-phase component) and open symbols for the imaginary part (out-of-phase). The lines are fits to the Debye law (3.3) with $\tau|_{H=0} = 6.3(3) \times 10^{-3}$ s and $\tau|_{H=200} = 7.2(1) \times 10^{-3}$ s. In case of acetate, fits parameters were $\tau|_{H=0} = 1.3(3) \times 10^{-2}$ s and $\tau|_{H=200} = 2.3(1) \times 10^{-2}$ s.

The nonlinear behavior

Fig. 3.22 shows the variation with temperature of the linear $\chi_1(\omega)$ and nonlinear $\chi_3(\omega)$ susceptibilities of a benzoate crystal. The behavior is quite similar to that observed for Mn_{12}Ac (See Fig. 3.10): at high temperatures χ_3' attains its equilibrium limit, whereas below the blocking

temperature it progressively tends to zero. Near the blocking temperature (when $\tau \approx 1/\omega$) similarly to what we observed in the Mn_{12}Ac sample (slow relaxing), the two nonlinear components χ_3' and χ_3'' attain very high values, crossing well above the equilibrium curve (dashed line). It evidences that the additional nonlinear contribution explained in the section devoted to Mn_{12} acetate, due to tunnelling spin reversal, is also present in the fast relaxing molecules.

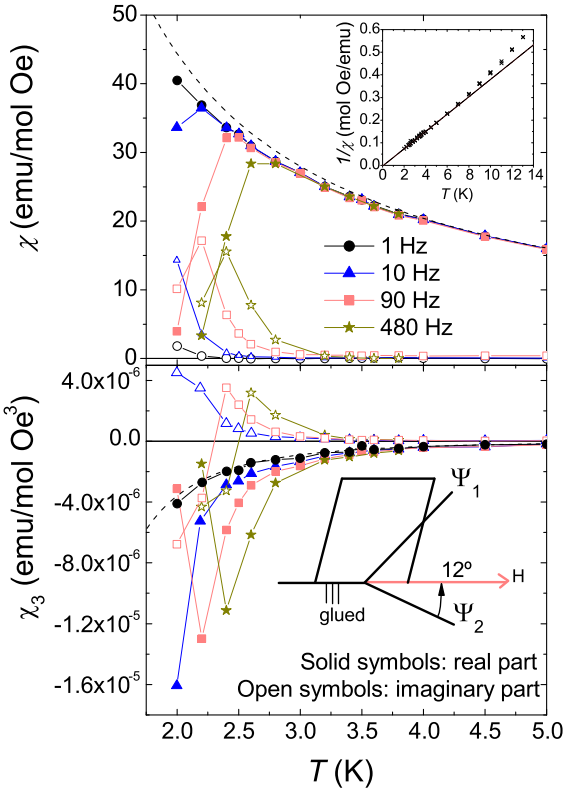

Fig. 3.22. Linear (top panel) and nonlinear susceptibilities (bottom) vs. temperature for several frequencies. Field was applied forming $\psi_1 = 52^o$ and $\psi_2 = 12^o$ respect of the easy axes of sublattice S1 and S2 respectively. Solid symbols are for the real parts and open symbols for the imaginary parts. Dashed lines are the equilibrium susceptibilities in the Ising (large anisotropy) limit (equations 3.9 and 3.10) taking into account the interaction $\theta = 0.3$ K and the crystal orientation. Inset: temperature dependence of the reciprocal *equilibrium* linear susceptibility and its fit to a Curie-Weiss law (3.5) for $T < 6$ K.

3.4.1 Equilibrium nonlinear susceptibility

Let us, first, study the equilibrium data. We have used the same criterion explained for the acetate measurements to extract the equilibrium χ_{T} and $\chi_{3\mathrm{T}}$. From the dynamical susceptibility data vs T, we take $\chi_{\mathrm{T}} = \chi_1'$ and $\chi_{3\mathrm{T}} = \chi_3'$ when the imaginary parts are reasonably small $\chi''/\chi' < 10^{-2}$.

In the inset of Fig. 3.22, the reciprocal equilibrium χ_{T} is shown. In the temperature range 2 K $< T <$ 7 K it approximately follows a Curie-Weiss law (3.5) with a Curie temperature $\theta \simeq 0.3$ K. The finite θ could be ascribed to dipolar interactions between the molecular spins in the crystal. This long-range order at low temperatures is lower than those observed in acetate crystals, where $\theta \simeq 1.2$ K congruently with the larger unit cell of the benzoate compound.

Excluding dipolar interactions, let us illustrate in the following, the dependence exerted by the magnetic anisotropy on the temperature-dependent susceptibility. In order to visualize these effects, we normalize the experimental χ_{T} and $\chi_{3\mathrm{T}}$ by their isotropic limits (equations 3.6 and 3.7). The normalized equilibrium susceptibility data are shown in Fig. 3.23.

The isotropic regime equations (3.6) and (3.7) are only valid when the thermal energy $k_{\mathrm{B}}T$ is larger than all zero-field splittings produced by the anisotropy. As a consequence, the isotropic limit is only attained for sufficiently high temperatures. In a benzoate crystal, the largest zero-field splitting produced by the anisotropy (between the state $m = \pm(S-1)$ and $m = \pm S$) reads $\Omega_0 = 7.6$ K, whereas for the SR specie this splitting read $\Omega_0^{SR} = 13$ K. When the energy $k_{\mathrm{B}}T$ becomes comparable to Ω_0, $\chi_{3\mathrm{T}}$ deviates from the simple isotropic limit and the normalized susceptibilities acquire a dependence on T. Therefore, when the temperature decreases, equilibrium linear and nonlinear reduced susceptibility increases towards the Ising limit in a different temperature range depending of the crystal, according to Ω_0 splitting. In the low temperature limit $k_{\mathrm{B}}T/D \to 0$ ($T < 5$ K for FR species and $T < 10$ K for SR species as is shown in Fig. 3.23) for both crystals, the experimental curves approach the Ising limit. In fact, $\chi_{3\mathrm{T}}/\chi_{3\mathrm{Iso}}$ become even larger than $\chi_{3\mathrm{Ising}}/\chi_{3\mathrm{Iso}}$, probably, as we have shown for the linear part, due to interactions which enhance the magnetic response at low temperatures.

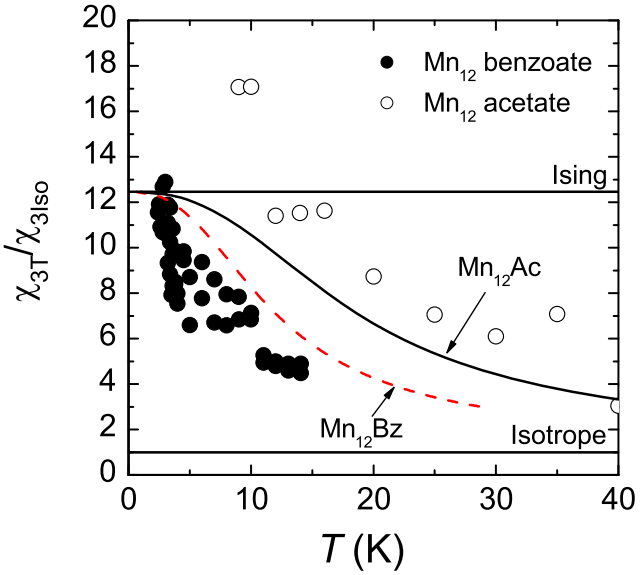

Fig. 3.23. Temperature dependence of the equilibrium nonlinear susceptibilities normalized by their values for isotropic spins (Brillouin limit). Results are shown for a single crystal of Mn_{12} acetate with the field parallel to the anisotropy axis ∘ and for a single crystal of Mn_{12} benzoate •. The lines are theoretical results for quantum spins. Field was applied between the easy axes of the sublattices S1 and S2: analogue to 3.22 $\psi_1 = 12^{\circ}$ and $\psi_2 = 52^{\circ}$.

3.4.2 Dynamical nonlinear susceptibility of the fast relaxing Mn_{12}

We have shown that for a SR species in the acetate: $U_0 = 65$ K and $\tau_0 = 3\times10^{-8}$ s. Estimated experimental parameters from [Takeda 2002] for the FR species are: $U_0^{\mathrm{FR}} = 38$ K and $\tau_0^{\mathrm{FR}} = 3.2\times10^{-11}$ s. The main interest to study such material lies in the difference in U_0 and τ_0 (in FR specie, it is in the same order of magnitude that τ_Φ) can induce a different behavior, in a sense that the spin precession should not be restricted by the decoherence time, leading to a "more classical" behavior that can be evaluated by means of the field expansion rate coefficients $g_\parallel$ and $g_\perp$.

To support the expected tendency to a more "classical behavior", let us evaluate τ_0/τ_{L} in both cases: $\tau_0/\tau_{\mathrm{L}} = 10^{-4}$ for SR species, and $\tau_0/\tau_{\mathrm{L}} = 0.1$ for FR species. The smaller value in FR species indicates a

larger delocalization of energy levels with respect to the total anisotropy energy barrier. As smaller τ_0 increases the broadening of the energy levels, the system approaches a more classical behavior.

Fig. 3.24 displays the frequency dependence of the nonlinear susceptibility of both Mn_{12}Ac and Mn_{12}bz. Curves were measured at constant temperature where the range $\omega\tau \sim 1$ can be approached and therefore relaxation effects become visible: the temperatures used were $T = 2$ K for Mn_{12}Bz and $T = 5$ K for Mn_{12}Ac crystals. The data corroborate the result shown in Fig. 3.22 as the nonlinear dynamic susceptibility is also reversed with respect to the classical predictions and χ_3' and χ_3'' attain higher values than those in equilibrium near the blocking temperature.

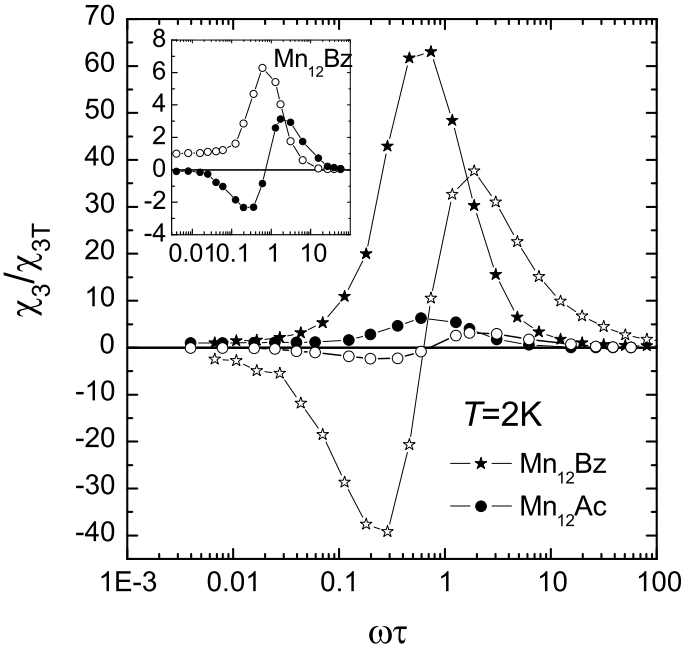

Fig. 3.24. Nonlinear susceptibility vs frequency at $T = 2$ K (Mn_{12}Bz) and $T = 5$ K (Mn_{12}Ac). Field was applied on *ab* plane between the easy axes of the sublattices S1 and S2. $\psi_1 = 12^o$ and $\psi_2 = 52^o$ were the angles with respect the easy axes of sublattice S1 and S2 respectively. The data are normalized by the equilibrium χ_{3T}. The relaxation time τ was obtained from ω-dependent linear susceptibility measurements (as those of figure 3.9). Inset: Magnification of the Mn_{12} benzoate curve.

However, in the benzoate crystal, around $\omega\tau \approx 1$ the maximum value of $\chi_3'/\chi_{3\mathrm{T}}$ is about ten times smaller than the value measured for the slow relaxing species. This large difference between the slow and the fast relaxing clusters cannot be ascribed to an angular dependence, since a value of near 70 for χ_3'/X_{3T} is also observed in powdered acetate samples [Luis 2004]. To evaluate the effects responsible for the lowering of the χ_3 peak we have to evaluate the field expansion coefficients $g_\parallel$ and $g_\perp$ through the components $\chi_3^\parallel$ and $\chi_3^\perp$. Two possibilities are possible, a lower $g_\parallel$, or a larger $g_\perp$ with respect to the canonical Mn_{12} acetate.

Neglecting the tilting of the easy axis on *ab* plane, for every frequency, and taking in consideration the orientation of the easy axes extracted from the linear analysis, the dependence of χ_3 with angle can be fitted with the following equation:

$$\begin{aligned}\chi_3(\omega) = \frac{1}{2}\left[\chi_3^\parallel \cos^4\psi_1 + \chi_3^\perp \mathrm{sen}^2\psi_1 \cos^2\psi_1\right] \\ +\frac{1}{2}\left[\chi_3^\parallel \cos^4(\psi_2) + \chi_3^\perp \mathrm{sen}^2(\psi_2)\cos^2(\psi_2)\right]\end{aligned} \tag{3.27}$$

Measurements were performed for different orientations, within the *ab* plane. In this way we vary both ψ_1 and ψ_2. From the fitting with respect to the crystal orientation (see an example in the inset of Fig. 3.25) we can extract both $\chi_3^\parallel$ and $\chi_3^\perp$ components as is shown in Fig. 3.25.

For all frequencies, the perpendicular $\chi_3^\perp = 0$, while $\chi_3^\parallel$ shows qualitatively the same behavior observed in Fig. 3.24. The coefficient $g_\parallel$ dominates $g_\perp$, which in the classical case embodies the precessional contribution and could be sizable. In conclusion, the fact that $\chi_3 \propto \cos^4\psi$ and the null contribution of $g_\perp$ enable us to elucidate that there are no classical contributions that mask the quantum large nonlinearity of Mn_{12} fast relaxing molecules. Discrepancies in the maximum observed in Fig. 3.24 are mainly due to the decrease in the energy barrier of Mn_{12} in benzoate, that diminishes the strong field dependence of the relaxation rate due to the detuning of degenerated energy levels. Instead, the smaller maximum value of $\chi_3'/\chi_{3\mathrm{T}}$ measured in this sample simply reflects a smaller $g_\parallel$, which in its turn indicates that resonant tunnelling in these molecules leads to a smaller relative change of the relaxation rate.

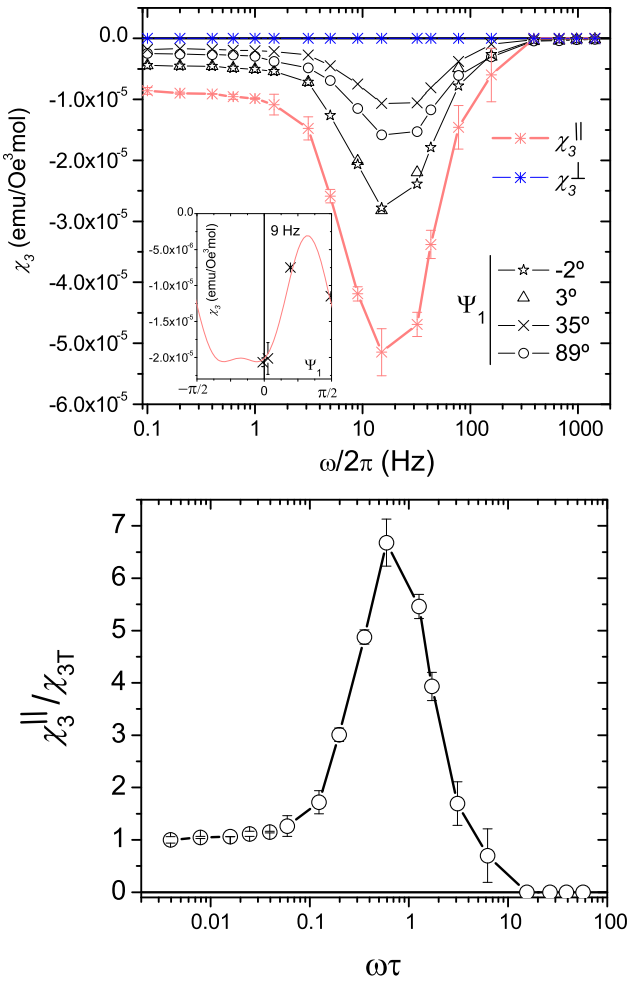

Fig. 3.25. UP: dynamical nonlinear susceptibility performed for different orientations (ψ_1). Also is shown the results of the angular fitting (Eq. 3.28) $\chi_3^{\parallel}$ and $\chi_3^{\perp}$. Inset: Example of fit for a frequency $\omega/2\pi = 9$ Hz. DOWN: normalized parallel nonlinear susceptibility vs frequency at $T = 2$ K. The data are normalized by the equilibrium χ_{3T}.

3.5 Conclusions

- The experimental nonlinear response is consistent with the established scenario of thermally activated tunnel via excited states in Mn_{12}.
- Compared to the linear susceptibility, the equilibrium χ_3 shows an enhanced sensitivity to the magnetic anisotropy, even for superparamagnets with axes distributed at random, where χ_1 looses this information (allowing to estimate D from measurements in powdered samples)
- The dynamical nonlinear susceptibility has a genuinely *quantum* contribution due to the detuning of the energy levels by a *longitudinal* field. It has a sign opposite to the classical (precessional) contribution, thus allowing to ascertain whether quantum effects, such as resonant tunnelling, are relevant in a given nanomagnet.
- The angular analysis of nonlinear susceptibility gives a bound for the decoherence time τ_Φ (timescale for the attainment of a diagonal density matrix due to the coupling to the phonon bath). The obtained τ_Φ turns out to be much shorter than the lifetime of the spin levels τ_0, and is responsible for a fast loss of coherent dynamics (like tunnel oscillations or precession).
- Near the resonant fields H_n (matching the levels at both wells) the χ_2 vs. H_z curves neatly amplify the resonant tunnel, as this entails large $\delta\tau/\delta H_z$. For fields, in between, the H_n's, tunnel is blocked and the response is governed by the thermo-activation over the total barrier, as in the classical case. This does not give such large τ', while its sign is reversed with respect to the tunnel contribution. Thus the sensitivity of χ_2 to the local features of the $\tau(H_z)$ curve provides an alternative method to asses if tunnelling plays a role in the relaxation of a superparamagnets; and if so, in which field ranges it does take place.
- In Mn_{12} benzoate single crystals, where most of the magnetic centers of Mn_{12} are "fast" species (lower blocking temperature), nonlinear magnetic susceptibility reveals an anisotropy change. The environment interaction (damping) respect to the Mn_{12} acetate crystals (where most of the magnetic centers of Mn_{12} are "slow" species) is, essentially, equivalent. However, the lower energy barrier diminishes the effect of the detuning of the energy levels by a *longitudinal* field.

4

Nonlinear magnetic susceptibility in Cobalt nanoparticles

4.1 Introduction

Metallic nanoparticles are of interest for widely employed applications, such as catalysis [Lewis 1993], photography [Fayet 1986] [James 1977] and electronics [Batlle 2002]. Also magnetic nanoparticles are used by animals like the Monarch butterfly to travel oriented by the Earth's magnetic field [Jones 1982]. Nowadays, applications in informatics need faster computers with larger memory that demand memory miniaturization and maximum memory reading speed.

The data storage importance: a practical interest

The maximum quantity of information that can be recorded depends on the minimum surface of the magnetic region that contains a bit. It seems obvious that single-molecule magnets (i.e. Mn_{12} studied in the previous chapter) provide a size limit, so the next step in miniaturization are magnetic nanoparticles. Thus, the development of dense arrays of magnetic nanoparticles are rather important with respect to the memory miniaturization. The main problem to be solved is to maintain the magnetization stable when a ferromagnetic material is reduced to nanometer size and the superparamagnetic limit is approached or overcome. This superparamagnetic limit is directly related with the anisotropy of the molecule: as the energy barrier between the orientation with an energy minima reads $U = K_{\text{anis}}V$, when the volume is reduced, the energy barrier is lowered and thermal agitation provides a perturbation that can take the magnetization over the barrier. If this process occurs, nanoparticles exhibit superparamagnetism (as we have shown in Mn_{12}) remanence is zero and no magnetic information is

recorded. Note that when temperature decreases, the process to overcome the barrier is frozen and makes recording information possible below this blocking temperature. As a consequence of their fast magnetic relaxation, molecular clusters or very small nanoparticles arrays are not useful to record information at room temperature, in contrast with nickel nanowires studied in chapter 2. On the other hand, the maximum speed of recording depends on the magnetic reversal speed of the magnetic material. Problems appear when particle interactions are not negligible, since recording a bit can erase the information stored previously on its neighbors. The study on the interactions effect will be extensively discussed in chapter 5.

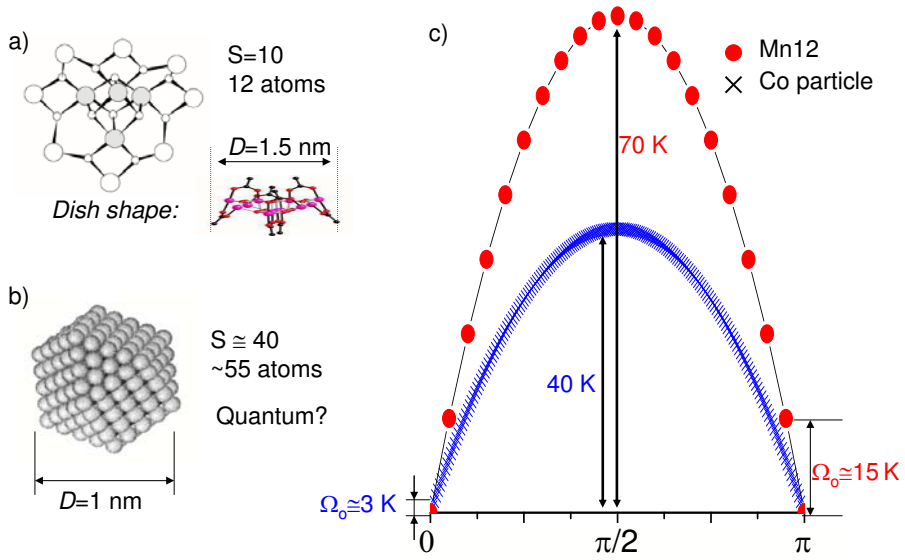

Fig. 4.1. Description of a) Mn_{12} acetate cluster and b) cobalt nanoparticle with 1 nm in diameter. c) Anisotropy energy barrier and energy states for a Mn_{12} acetate single-molecule magnet (circles) and for a cobalt particle with 1 nm in diameter (crosses).

The presence of quantum phenomena and spin dynamics: a basic research

As we have shown in chapter 3, the nonlinear susceptibility is a very sensitive measurement to distinguish between the quantum or the classical behavior. As we can see in Fig. 4.1 the cobalt particles (in particular, we will study a cobalt sputtered nanoparticle arrays) can be proposed as candidates to show a quantum behavior. Both the size and the energy barrier to be overcome for the reversal of their spins are in the same order of magnitude as that of the Mn_{12} molecules. Therefore, nanoscale clusters provide a next step in size from the limit of single-molecule magnets to investigate the fuzzy borderline between the classical and quantum worlds. The first goal of the work carried out in this chapter is to discern between the classical or quantum behavior of these cobalt particles.

In this chapter, we also propose to study the anisotropy and the spin dynamics of these dense arrays of nanoparticles using the previously described nonlinear susceptibility, in the same way as was done in Mn_{12} crystals in chapter 3. Independently of the "classical" or "quantum" magnetic behavior, χ_3 provides information about the anisotropy and the "damping" regime [Garcia-Palacios 2000a] of the particles, even if the anisotropy axes are distributed at random. Notice that the damping determines the fastest speed at which spin can reverse its orientation. Cobalt nanoparticle samples are very adequate to achieve the present study because of the easiness to prepare samples varying the anisotropy and therefore the energy barrier in a controlled way. As the magnetic anisotropy in cobalt particles are determined by the special properties of surface atoms [Bartolomé 2006] [Luis 2002b] [Luis 2006], the anisotropy constant can be tuned easily by:

- Modifying the size of the nanoparticles: consequently the fraction of surface atoms at the surface is varied and thereby the surface contribution to the anisotropy constant as well.
- Varying the nanoparticle environment: as the samples can be prepared in an insulator or in a metallic matrix, the surrounding environment of the atoms in the surface can be modified easily.

4.2 Sample fabrication and characterization

The preparation

Cobalt nanoparticle samples were prepared by Dr. F. Petroff and co-workers in Palaiseau (France), at the Unité Mixte de Physique that belongs to Thales Corporate, CNRS and the Université Paris-Sud XI.

Samples were produced by rf sputtering. The method is sketched in Fig. 4.2. The sputtering fabrication consists of depositing a target material on a substrate using a ionized plasma. Under a strong applied voltage, an argon plasma ionizes and impacts on the target substrate. Atoms/molecules in the surface target material can detach probabilistically when an argon molecule impacts, and target molecules deposit on the substrate.

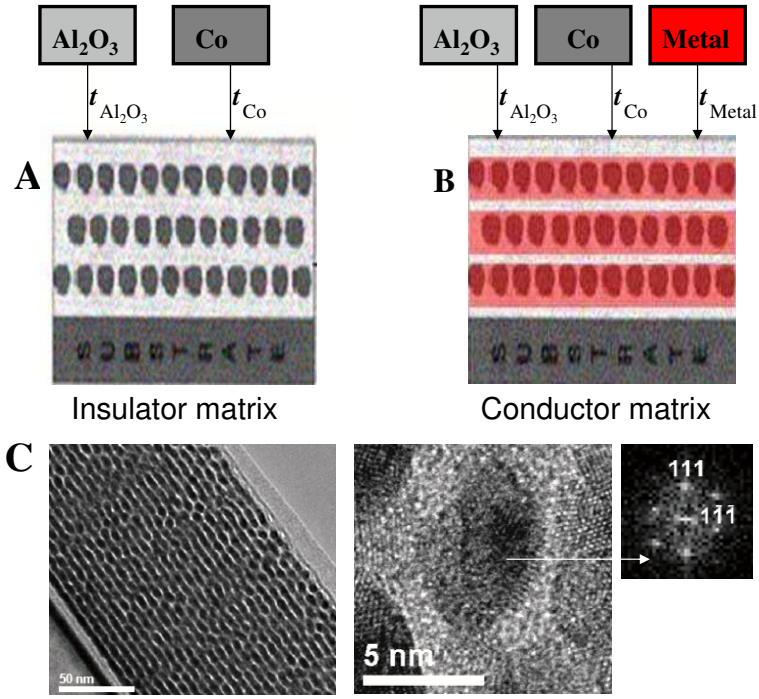

Fig. 4.2. Schematic diagram of Cobalt nanoparticle samples preparation. Cobalt nanoparticles are embedded in an insulator (A) or in a conductor matrix (B). t is the nominal thickness and is controlled by the substrate exposition time to the plasma. (C) TEM image of a cobalt nanoparticles multilayer embedded in gold. It is shown a nanoparticle amplification with a specific area XRD analysis.

In the standard fabrication (fig. 4.2A), a sequential sputtering deposition of amorphous Al_2O_3 and Co layers on a silicon substrate was performed. Due to the difference in surface energies, the Co layer aggregates forming nanoparticles well dispersed in the Al_2O_3 layer [Maurice 1999], with six nearest neighbors on average. Pilling up next layers, cobalt nanoparticles grow in the valleys left on the latest deposited layer. As a result, cobalt nanoparticles are embedded in an alumina insulator matrix in a quasi-regular spatial order of approximately hexagonal close-packed symmetry [Babonneau 2000], as we can see in Fig. 4.3.

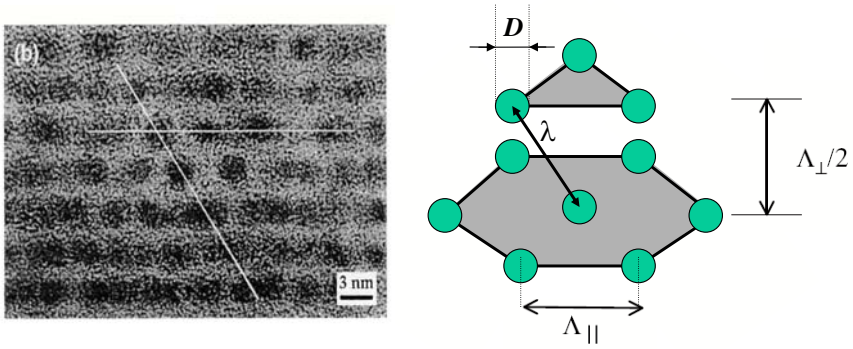

Fig. 4.3. LEFT: cross-section TEM image from Co/Al_2O_3 multilayer sample with t_{Co}=0.7 nm and $t_{Al_2O_3}$ = 3 nm. RIGHT: schematic diagram of Cobalt nanoparticle structure [Babonneau 2000].

Electron energy loss spectroscopy (EELS), X-ray photoelectron spectroscopy (XPS) and X-ray absorption spectroscopy (XAS) indicate that encapsulation with sputtered alumina keeps the clusters free from cobalt oxide [Briatico 1999]. The presence of an antiferromagnetic shell of cobalt oxide can also be rejected since hysteresis loops measured after a field cooled protocol show no exchange bias [Luis 2002b].

To modify the matrix embedding the particles, a metallic layer of copper or gold can be deposited on the cobalt particles (fig. 4.2B). Sequential depositions of Al_2O_3, Co and metal on a silicon substrate were performed. The average cluster' size and shape appear to be preserved after the capping [Luis 2006].

The sample preparation parameters are:

- N: number of Co/Al_2O_3 layers (When samples are metal capped, N is the number of Co/Al_2O_3/Metal layers).
- t_{Co}: nominal thickness of Co. It is the thickness of the cobalt supposing homogeneous layer deposition. In order to increase the Co nanoparticle diameter, it can be varied between 0.1 to 1.5 nm.
- $t_{Al_2O_3}$: nominal thickness of alumina layer. Typically, $t_{Al_2O_3}$=3 nm.
- t_{Metal}: nominal thickness of metal (if cobalt is capped). Typically, t_{Metal}=1.5 nm, sufficient to partially cover the cobalt nanoparticles.

Control of the cobalt nanoparticles array structure

As is shown in Fig. 4.4 the diameter of cobalt nanoparticles D varies linearly with t_{Co}. As the nominal thickness is controlled by the substrate exposition time to the plasma, the diameter of the particles is easily controllable. A diameter size distribution is obtained but the normalized variance σ remains approximately independent of size (Fig. 4.4). It is confirmed that, for the same t_{Co}, the average D and the distribution width of a monolayer or multilayers are nearly identical [Luis 2002b].

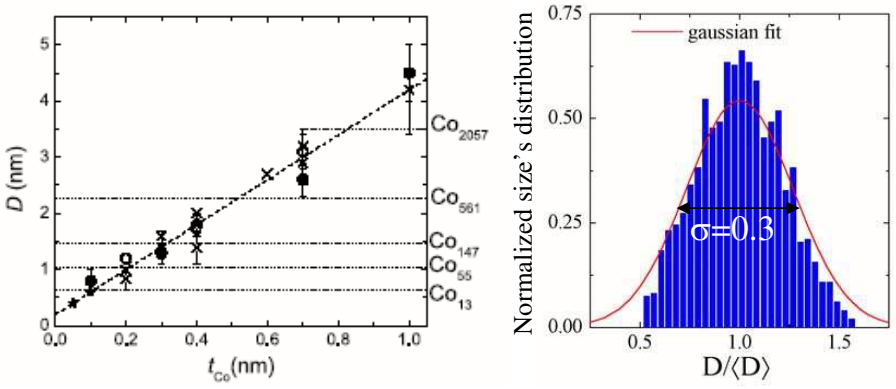

Fig. 4.4. LEFT: average particle diameter as a function of nominal thickness extracted from different techniques: crosses are extracted from TEM analysis, circles from magnetic measurements and stars are extrapolations from TEM analysis. RIGHT: normalized gaussian distribution of diameter sizes for a sample synthesized with $t_{Co} = 0.7$ nm.

The sphericity and the crystallinity of the nanoparticles also varies with the nominal thickness t_{Co}. Nanoparticles formed for a nominal thickness $t_{\mathrm{Co}} < 0.7$ nm exhibit a good sphericity, while for $t_{\mathrm{Co}} > 0.7$ nm nanoparticles tend to become plates loosing sphericity. For $t_{\mathrm{Co}} > 1.5$ nm, the coalescence limit is reached and cobalt does not form into independent particles [Babonneau 2000]. For $t_{\mathrm{Co}} < 0.8$ nm cobalt grows with the fcc β phase [Kitakami 1997], in contrast with hcp cobalt bulk structure, stable when $t_{\mathrm{Co}} > 0.8$ nm.

Once we know the cobalt nanoparticle array structure, let us describe the order using the parameters shown in Fig. 4.3. $\Lambda_{\parallel}$ is the in-plane cobalt distance. As in-plane surface-to-surface distances are, on average, 2.2 nm [Maurice 1999] and are independent of the cobalt nanoparticle diameter, $\Lambda_{\parallel}$ reads:

$$\Lambda_{\parallel} \backsimeq D + 2.2 \ (nm) \tag{4.1}$$

$\Lambda_{\perp}$ is the distance between two cobalt nanoparticles in the direction perpendicular to the layers, and it is determined by the nominal thickness of alumina, so:

$$\frac{\Lambda_{\perp}}{2} \backsimeq t_{Al_2O_3} \tag{4.2}$$

In conclusion, nanoparticles tend to self-organize into nearly ordered (at short ranges) close-packed lattices. These arrays of sputtered Cobalt nanoparticles can be easily controlled in morphology by fabrication parameters and the characterization of the samples is well-defined in terms of particle-size, shape distribution, or the spatial distribution of the nanoparticles.

Magnetic description of the samples: the surface anisotropy

Physical methods provide a top-down approach to produce new magnetic materials. In opposition with the bottom-up chemically-synthesized single molecule magnets with sizes all identical to each other, the experimental study of our nanometer-sized particles is complicated by the fact that these systems are usually macroscopic ensembles of particles with different sizes. As we have explained before, the size dispersion can be described by a gaussian size distribution (See Fig. 4.4). Size distribution $g(D)$ gives rise to an activation energy distribution $f(U)$. From the imaginary component of the linear susceptibility χ'', the full distribution of activation energies $f(U)$ can be

estimated to find which value of U corresponds to the mean diameter $\langle D \rangle$ (See [Torres 2002] [Luis 2002b] for a detailed description). Once $U(\langle D \rangle)$ is obtained, assuming a spherical shape of the clusters, the effective anisotropy constant can be calculated by the expression:

$$K_{\text{eff}} = \frac{U(D)}{V}, \qquad V = \frac{\pi}{6} D^3 \tag{4.3}$$

Effective constant values are one or two orders of magnitude larger than the expected intrinsic magnetocrystalline anisotropy. The size dependence follows approximately the following expression:

$$K_{\text{eff}} = K_{\text{bulk}} + \frac{6K_{\text{S}}}{D} \tag{4.4}$$

where $K_{\text{bulk}} = 5(2) \cdot 10^4$ J/m^3 and $K_{\text{S}} = 3.3(0.5) \cdot 10^{-1}$ mJ/m^2. K_{bulk} is close to the intrinsic magnetocrystalline anisotropy of fcc cobalt $K/4 = 6.5 \cdot 10^4$ J/m^3, where K is the second order cubic anisotropy constant. Note that K_{eff} is observed to increase as the average diameter D of the nanoparticles decreases. Values of diameter dependent anisotropy constant are in good agreement with those reported in [Bodker 2002] [Chen 1995] [Respaud 1998]. As the size of the particles decreases, an increasing fraction of the total magnetic atoms lies at these surface. The electronic and magnetic structure of these atoms is modified by the smaller number of neighbors as compared to the bulk and/or by the interaction with the surrounding atoms of the matrix where the particles are dispersed.

4.3 Experimental method

Samples

Different samples with a variation in cobalt nanoparticles size were synthesized. Also the surrounding environment can be varied: the cobalt particles can be capped by a metal as copper (Cu) or gold (Au). When the cobalt particles were not capped, samples are surrounded by alumina (A). In the following, samples will be denoted by the surrounding element and a number that indicates the nominal thickness of cobalt in Armstrong Å. Much of these samples are summarized in table 4.1.

Name	N	t_{Co} (nm)	$t_{\mathrm{Al_2O_3}}$ (nm)	t_{Metal} (nm)	D (nm)	σ	x_{para}
A2	50	0.2	3	0	1.05	0.24	0.38
Cu2	50	0.2	3	1.5	1.2	0.28	0.32
A4	25	0.4	3	0	1.8	0.3	0.144
Cu4	20	0.4	3	1.5	1.7	0.3	0.275
Au4	25	0.4	3	1.5	1.75	0.3	0.24

Table 4.1. Parameters of the studied samples. Extracted from [Luis 2002b] and following magnetic measurement from [Torres 2002]. Note that D refers to the mean diameter, σ in diameter units and x_{para} is the fraction of paramagnetic cobalt amount that does not form nanoparticles.

It is corroborated by TEM that cobalt that does not form nanoparticles, is distributed at random around the sample and form little aggregates of few atoms [Maurice 1999]. From magnetization curves this quantity can be extracted [Torres 2002] [Luis 2002b]. Every cobalt atom contributes to the saturation magnetization with $1.71\mu_{\mathrm{B}}$, where μ_{B} is the Bohr magneton. In the saturation region, it is observed a linear increase due to this fraction that can be corrected. As we know the total cobalt amount deposited, we can estimate this fraction x_{para} from the saturation magnetization value as: $M_{\mathrm{s}} = 1.71\mu_{\mathrm{B}}\,(1 - x_{\mathrm{para}})$.

Magnetic measurements

The magnetic measurements were performed using a commercial SQUID magnetometer. The temperature range of the measurements was $1.8 < T < 320$ K. The ac susceptibility was measured by applying a small ac field (4 Oe) sufficiently small not to induce any additional nonlinear contribution . The frequency of the ac magnetic field can be varied continuously between 0.01 Hz and 1.5 kHz. The samples had a rather large diamagnetic signal arising from the silicon substrate. This contribution was estimated independently by measuring a bare substrate and found to be linear in field and independent of the temperature. It was subsequently subtracted from all experimental data.

Nonlinear susceptibility is performed via polynomial fits of the H-dependent linear susceptibility. The quadratic coefficient gives $\chi_3(\omega)$ as is explained in chapter 3. An illustrative example of the fitting procedure is shown in Fig. 4.5. In this static field H range, a simple parabolic dependence $\chi_1 + 3\chi_3 H^2$ provides a good approximation.

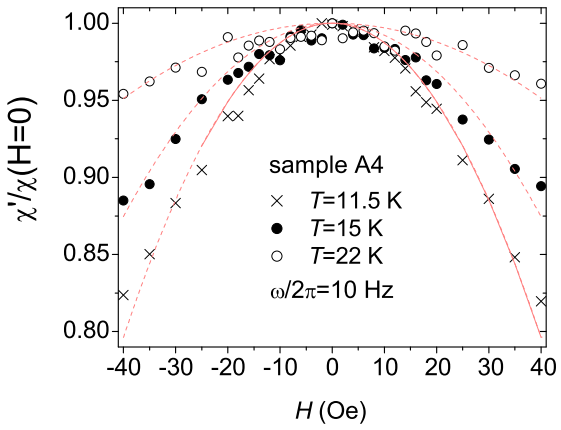

Fig. 4.5. Magnetic ac susceptibility of cobalt nanoparticles normalized by its zero-field value, vs. the static field H. Results for the *real part* at $\omega/2\pi = 10$ Hz and various temperatures T are shown. The parabolic approximation $\chi_1 + 3\chi_3 H^2$, which dominates the low-field behavior is shown by dotted lines.

4.4 Nonlinear susceptibility of cobalt nanoparticles

Cobalt nanoparticles exhibit superparamagnetic behavior that for each particle can be described with the well-known Debye's law (equation 3.3). As we have seen in the study of Mn_{12}, the maximum slope of the real part χ_1' of the susceptibility vs ω and the maximum of the imaginary part χ_1'' correspond to the condition $\omega\tau = 1$. Thus, a fit of the experimental data enables a very accurate determination of the relaxation time as a function of external parameters, such as temperature and magnetic field. This well-known determination of τ enables to determine the nature of the spin reversal mechanism. The frequency-dependent dynamical response of the nonlinear susceptibility is also sensitive to the "damping" of the nanoparticle spin dynamics by their environment (phonons, conduction electrons,etc...) as we can see in Fig. 4.6. So, we can discern between the under- or over- damped regimes.

In the present case, when a size distribution is present, the relaxation times of nanoparticles with a divergence of a 10% in diameter gives relaxation time divergences of 7 orders of magnitude, τ is not well-defined and invalidates the analysis. The main advantage of the nonlinear component is that it enables us to discern some aspects rel-

ative to the classical or quantum nature of the relaxation process, the anisotropy and the damping in an independent way, even if a well-defined relaxation time is not known.

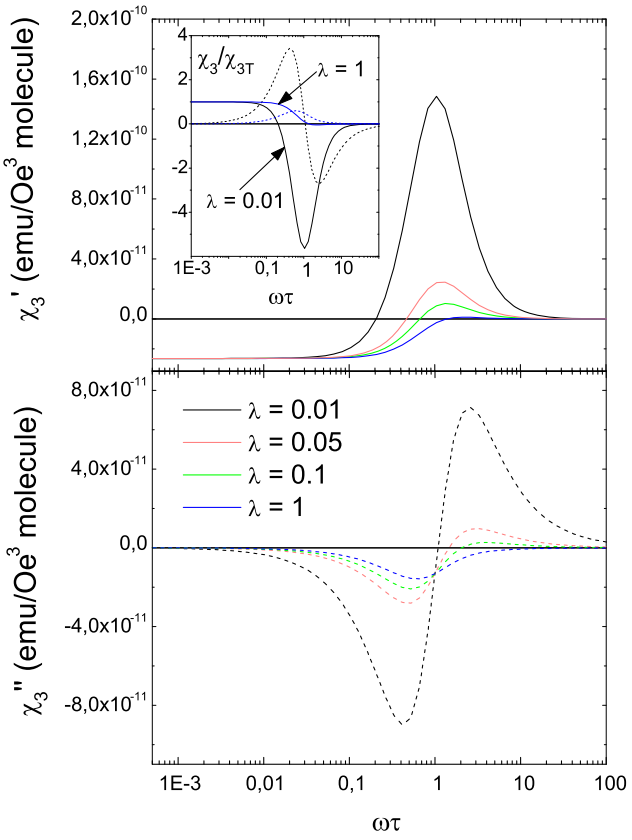

Fig. 4.6. Prediction of a frequency dependence of nonlinear susceptibility for a "classical" superparamagnet with a well defined relaxation time τ in function of the "damping" λ extracted from [Garcia-Palacios 2004]. Real and imaginary part are presented in solid and dashed lines respectively. Inset: Equilibrium normalized susceptibility for a "underdamped" λ=1 and a "overdamped" λ=0.01 situation. Predictions were obtained using the following parameters: U=70 K, T=5 K and $\psi = \pi/4$.

Contrary to what we did for Mn_{12}, in the case of cobalt nanoparticles we did not perform the analysis using the frequency dependence of the susceptibility. It is more appropriate to achieve these analysis using the nonlinear susceptibility dependence with temperature. As τ diminishes exponentially with temperature following an Arrhenius law (Eq. 3.4), we are able to show the superparamagnetic phenomenology in an accessible temperature range.

4.4.1 Classical vs quantum behavior

The Fig. 4.7 shows the variation with temperature of the linear $\chi_1(\omega)$ and nonlinear $\chi_3(\omega)$ susceptibilities of cobalt nanoparticles with average diameter 1.8 nm embedded in alumina. The blocking transition is just broader with respect to SMM crystals, on account of the distribution of sizes characteristic of particles. Linear equilibrium susceptibility χ_T data are shown in the inset of Fig. 4.7. In the temperature range between 15 and 30 K, χ_T follows a Curie-Weiss law with a Weiss temperature θ= 4.4 K. The finite θ reveals the existence of dipolar interactions between the cobalt nanoparticles that form the 3D array. The behavior of the nonlinear component is qualitatively similar to that shown for Mn_{12} (Fig. 3.10): at high temperatures χ_3' attains its equilibrium limit, whereas below the blocking temperature it progressively tends to zero. However, paying attention near the blocking temperature (i.e. when $\tau \approx 1/\omega$) strong differences are found in contrast with Mn_{12} SMM in which the two components χ_3' and χ_3'' attain very high values, crossing well above the equilibrium curve (dotted line in Fig. 3.10): both χ_1' and χ_3' lie always below (in absolute values and within experimental uncertainties) their respective equilibrium limits. Clearly, the additional contribution due to tunnelling spin reversal is absent in the nanoparticles. As we can see in Fig. 4.1 the higher spin values reduce the energy states discreetness with respect the Mn_{12} molecule, thus probably masking any quantum behavior [Garcia-Palacios 2000a].

In Fig. 4.8 the nonlinear susceptibility for samples with a reduced size $D \sim 1.05$ nm and different environment is represented. The same qualitative dependence on T is observed for the smaller particles and for particles embedded in any media (insulator in case of alumina or metallic in case of cooper and gold), evidencing the same "classical" behavior. Note that χ_3 provides in a very sensitive way differences in temperature divergences (θ) that reveal a different intensity of interactions. We will extend this interaction study in chapter 5.

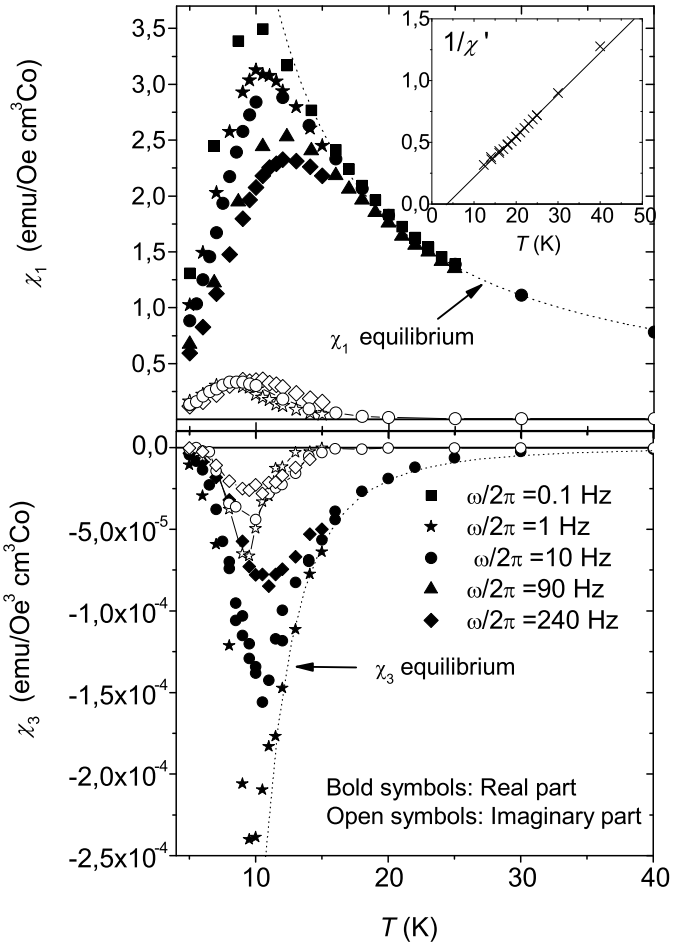

Fig. 4.7. Linear (top panel) and nonlinear susceptibilities (bottom) vs. temperature for several frequencies measured in a sample with $t_{\mathrm{Co}} = 0.4$ nm (average diameter D is 1.8 nm and contains about 280 atoms) in a matrix of alumina (A4). Solid symbols are for the real parts and open symbols for the imaginary parts. Dashed lines are the equilibrium susceptibilities in the Ising (large anisotropy) limit. Inset: temperature dependence of the reciprocal *equilibrium* susceptibility χ_1'.

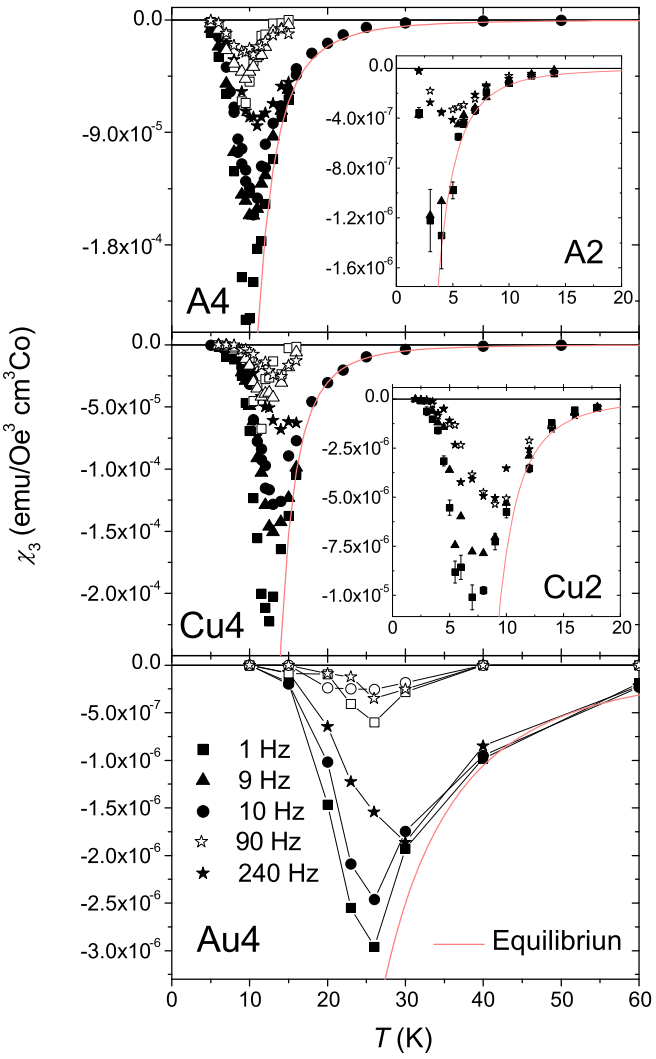

Fig. 4.8. Nonlinear susceptibility measurements for samples with $t_{\mathrm{Co}} = 0.4$ nm in alumina (A4), copper (Cu4) and gold (Au4). Real part and imaginary part in bold and open symbols respectively. Red lines are the equilibrium susceptibilities in the Ising (large anisotropy) limit. Insets: Real part of the nonlinear susceptibility measurements for samples with $t_{\mathrm{Co}} = 0.2$ nm in alumina (A2) and copper (Cu2). Error bars are shown for $\omega/2\pi = 1$ Hz.

4.4.2 Equilibrium nonlinear susceptibility and magnetic anisotropy

Neglecting interactions between nanoparticles, the magnetic anisotropy [Carlin 1986] exerts the most important influence on the temperature-dependent susceptibility. Unfortunately, as the anisotropy axes of our particles are distributed at random, the equilibrium linear susceptibility χ_1 is insensitive to this temperature dependence of the anisotropy [Garcia-Palacios 2000c] [Lopez-Ruiz 2005]. By contrast, $\chi_{3\mathrm{T}}$ retains information on the anisotropy strength even for randomly oriented anisotropy axes [Luis 2004]. In this way, we shall use an equilibrium magnitude $\chi_{3\mathrm{T}}$ to discern some aspects relative to the anisotropy.

In this section, we propose to study the nonlinear susceptibility in equilibrium conditions. We have considered, in analogy to Mn_{12} measurements, that the experimental data correspond to an equilibrium regime when the imaginary part of the linear susceptibility is zero or reasonably small ($\chi''/\chi' \leq 10^{-2}$). The theoretical expressions for the nonlinear susceptibility in the (high temperature) isotropic [Eq. 3.7] and (large anisotropy) Ising [Eq. 3.10] regimes for classical spins and anisotropy axis oriented at random follow:

$$\overline{\chi}_{3\mathrm{Iso}} = -N\frac{(M_{\mathrm{SB}}V)^4}{45(k_{\mathrm{B}}T)^3} \tag{4.5}$$

$$\overline{\chi}_{3\mathrm{Ising}} = -N\frac{(M_{\mathrm{SB}}V)^4}{15(k_{\mathrm{B}}T)^3} \tag{4.6}$$

Overline refers to axes oriented at random and N is the number of cobalt particles. The magnetic moment of a molecular spin $\mu = g\mu_{\mathrm{B}}S$ has been replaced by the macroscopic expression $\mu = M_{\mathrm{SB}}V$, where M_{SB} is the bulk saturation magnetization by volume units. For cobalt, M_{SB}= 1450 emu/cm^3.

From these last equations, it is easy to deduce that the equilibrium susceptibility $\chi_{3\mathrm{T}}$ should decrease with increasing temperature from the Ising limit $\chi_{3\mathrm{Ising}}$ to the isotropic limit $\chi_{3\mathrm{iso}}$. In the temperature range covered by our experiments, we can consider the anisotropy variation near the Ising limit. To study quantitatively the Ising to isotropic transition, we have to develop the equation 4.6 to take into account the finite anisotropy barrier and the temperature. The new equation reads [Luis 2004]:

$$\bar{\chi}_{3\mathrm{Ising}}(U,T) = -N\frac{(M_{\mathrm{SB}}V)^4}{(k_{\mathrm{B}}T)^3}\frac{1}{15}\left[1-2\frac{k_{\mathrm{B}}T}{U}\right] \tag{4.7}$$

This corrected expression for the Ising limit nonlinear susceptibility is valid for $k_{\mathrm{B}}T/U < 0.5$. It is convenient, in order to remove the $1/T^3$ contribution and visualize easily the remaining temperature dependence due to the effect of the anisotropy, to normalize the experimental susceptibility $\chi_{3\mathrm{T}}$ by its Ising limit, $\chi_{3\mathrm{Ising}}$. We can deduce that the reduced susceptibility $\chi_{3\mathrm{T}}/\chi_{3\mathrm{Ising}}$ may decrease with increasing temperature from 1 to 0.33 following, in our temperature range, an approximately linear variation with the temperature. The slope of this variation is related inversely with the energy barrier U. As we have anticipated, this procedure gives us an estimation of this parameter without the need to estimate the relaxation time.

Because of its surface origin, the anisotropy constant can be tuned by changing diameter of the nanoparticles (See equation 4.4) or by varying the different environment that interacts with the surface atoms i.e. varying the nanoparticle environment. Measurements were carried out on samples with different sizes and environments.

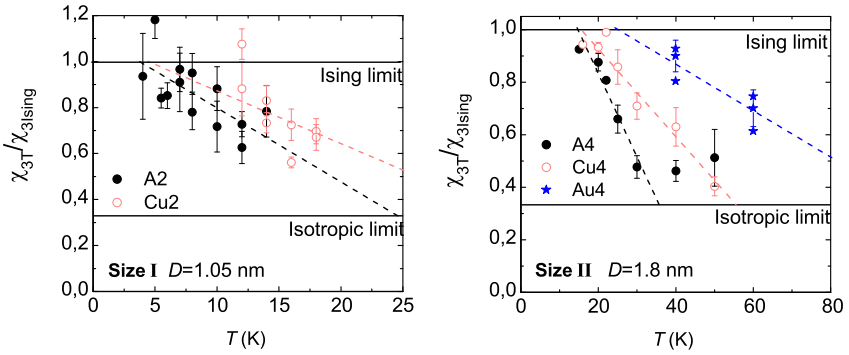

Fig. 4.9. Temperature dependence of the equilibrium nonlinear susceptibilities normalized by their values for Ising limit. LEFT: For particle arrays of average diameter 1.05 nm. RIGHT: For particle arrays of average diameter 1.8 nm. Lines show the best fit in the linear range that corresponds with equation 4.7.

As it is shown in Fig. 4.8, in analogy with the linear contribution, nonlinear equilibrium behavior drops from the equilibrium value toward zero below a certain temperature. This blocking temperature T_b increases with the capping in both sizes as a consequence of the surface interaction with the media that affects the anisotropy $T_b(A) < T_b(Cu) < T_b(Au)$.

In Fig. 4.9 is shown the temperature dependence of the normalized equilibrium nonlinear susceptibility, i.e. measured above T_b, for the samples listed in the table 4.1. For all samples, the reduced nonlinear susceptibility tends progressively from the Ising (infinite anisotropy) towards the isotropic limit when temperature increases, as was predicted. Different slopes can be shown in the transition due to the different energy barriers induced by the anisotropy. From the linear fits we can obtain a quantitative estimation of the anisotropy barrier. For particles with 1.05 nm in average diameter (size I), the anisotropy increases when the particles are embedded in Cu, a change by about 40%, that is not far from that observed in the T_b. In case of arrays with particles of 1.8 nm (size II), the anisotropy barrier U grows as 1/1.3/2.9 when particles are embedded in copper or gold respectively. The growth in blocking temperatures T_b reads 1/1.3/2.6.

Note the case when size is reduced (A2 vs A4 data). This change in the anisotropy can be explained as a consequence of the change in the particle volume. As $U(D) = K_{\text{eff}}V$ a little change in D causes a huge increment in volume. This change is reflected in the nonlinear susceptibility, due to the huge dependence with the volume, i.e. the diameter, but can not be ascribed in an univocal way to a change in the anisotropy, as the anisotropy ratio between a particle with a diameter D_1 with respect to a particle with a diameter D_2 follows: $K_1/K_2 = U(D_1)V_2/U(D_2)V_1$.

To conclude, we can observe using an equilibrium magnitude, without the necessity of the relaxation time study, the increase of the anisotropy due to the capping of the samples. This influence of the metal surrounding in the enhancement of cobalt anisotropy is confirmed by XMCD studies [Bartolomé 2004] [Bartolomé 2007] [Luis 2006] that show an orbital moment enhancement due to hybridization between the surface cobalt atoms and metal adjacent atoms of the bath. These little modifications (size or environment) therefore provide simple methods to control the magnetic behavior of nanoparticles.

4.4.3 Dynamical nonlinear susceptibility: Damping of spins

In this section we will investigate the dynamical response. As we have concluded previously the classical behavior of our particles, we can make use of classical theoretical predictions that link χ_3 to the damping of spin dynamics by the environment [Fig.4.6]. The nonlinear dynamical susceptibility of classical superparamagnets [Garcia-Palacios 2000a] [Garcia-Palacios 2000b], such as our cobalt nanoparticles, is quite sensitive to the coupling of spins to their environment, usually referred as the "bath" (lattice vibrations, nuclear spins, conduction electrons, other molecular spins...). Fig. 4.10 shows this information is preserved even for axes distributed at random and in the presence of a distribution of particle sizes. This interaction of the spin with its surroundings perturbs and eventually destroys the Larmor precession of the spins. It also determines the fastest speed at which magnetic moment flips. This influence is measured by a "damping" parameter λ [Garcia-Palacios 2004].

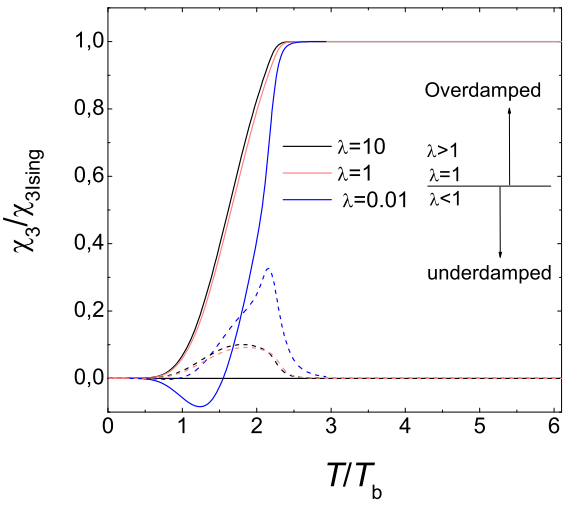

Fig. 4.10. Temperature dependence of nonlinear susceptibility of a cobalt superparamagnet with axis distributed at random in function of the "damping" λ. The susceptibility was normalized by the Ising (low temperature) limit. Real and imaginary part are presented by solid and dashed lines respectively.

To illustrate the spin dynamics behavior, let us propose the analogy between the spin and a mechanical oscillator, such as a spring. In the same way that a spring oscillates around the equilibrium position when is placed in a higher energy point, when the spin is in an excited state, and neglecting quantum tunnelling, the spin undergoes the classical Larmor precession at frequency $\omega_{\mathrm{L}} = 2\pi/\tau_{\mathrm{L}}$ around the anisotropy axis. In addition, equal to a damped spring, it can decay towards the fundamental state via the emission of lattice phonons (Fig. 4.11(b)), a process that determines the lifetime τ_0 of the excited level.

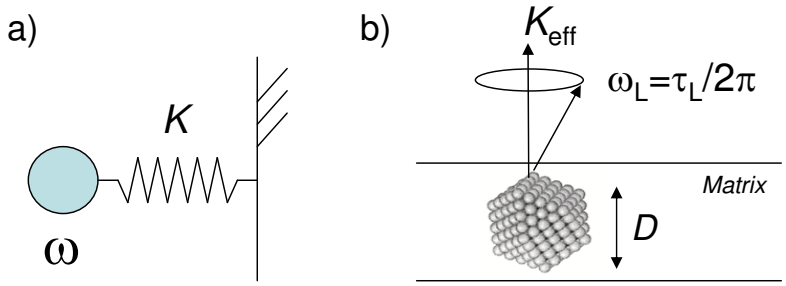

Fig. 4.11. (a) A damped oscillator: mechanical system analogy for the spin dynamics (b) "Classical" spin dynamics of a particle with the easy axis in the anisotropy axis direction marked by K_{eff}.

The Larmor precession frequencies are related with the energy of excited states Ω_0. For large spins S the energy gap between fundamental and the first excited state reads $\Omega_0 = 2U/S$. So, Larmor precession time τ_{L} can be tuned with the anisotropy. In particular, the Larmor precession period follows:

$$\tau_{\mathrm{L}} = \frac{2\pi}{\omega_{\mathrm{L}}} = \frac{2\pi\hbar}{\Omega_0} \tag{4.8}$$

The system is in an underdamped regime when $\tau_{\mathrm{L}} \ll \tau_0$, while for $\tau_{\mathrm{L}} \gg \tau_0$ the system is considered overdamped. As "damping" parameter can be written as $\lambda = \tau_{\mathrm{L}}/\tau_0$, an underdamped or overdamped regime reflect $\lambda < 1$ or $\lambda > 1$ respectively. For particles with 1.05 nm in average diameter, Larmor precession time results $\tau_{\mathrm{L}} \approx 1.4 \cdot 10^{-11}$ s whereas for particles with average diameter D=1.8 nm, $\tau_{\mathrm{L}} \approx 2.2 \cdot 10^{-11}$s.

Thus, to vary the damping regime, the easiest possibility is to vary the anisotropy K_{eff} and therefore the energy barrier. It is analogous to vary the spring constant K in an oscillator. To achieve this variation it is sufficient to modify the size of the nanoparticles and consequently the fraction of surface atoms at the surface. As we have explained in a previous section, the anisotropy constant increases inversely with the nanoparticle diameter.

Another strategy to vary the damping regime is to vary the matrix. It is analogous to introduce a modification in the viscosity of the environment in the oscillator. To carry out this variation in the nanoparticle environment, the samples can be prepared embedded on an insulator or in a metallic matrix. The different interactions depending on the nature of the "bath", can play an important role on the spin dynamics [Stamp 1996].

Size dependence

Let us begin the dynamical study of the reduced χ_3 with the study of the particle size dependence. In Fig. 4.12 these data for particles with $D = 1.05$ nm and 1.8 nm embedded in alumina are shown. Measurements were done at several frequencies.

At low temperatures, the magnetic moments are blocked until the equilibrium is reached. Susceptibility decreases according to the equilibrium temperature-induced change in the anisotropy. As a consequence of the different blocking temperatures, the samples attain the equilibrium at different temperatures depending of the sample size and the frequency measured. To analyze the data, it is convenient to scale the temperature by the sample blocking temperature. Note, connecting with the previous section 4.4.2, that the scaling of $\chi_{3\text{T}}/\chi_{3\text{Ising}}$ with T/T_{b}, both at $T > T_{\text{b}}$ and $T < T_{\text{b}}$ shows the degree of the enhancement of the anisotropy predicted.

Within the experimental uncertainties, the nonlinear susceptibility reveals that in alumina insulator matrix, despite of the size change, cobalt nanoparticles spin dynamics behavior is analogous. The absolute value of $\chi_{3\text{T}}$ never exceeds in all cases the equilibrium, proving the characteristic "classical behavior" of our particles. Comparing with theoretical curves for classical spins and size distribution, experimental data are close to the $\lambda = 1$ curve in both samples, revealing an "overdamped" regime. As $\lambda \geq 1$, $\tau_0 \leq \tau_{\text{L}}$ and a excited state lifetime bound can be extracted: $\tau_0 \leq 1.4 \cdot 10^{-11}$ s.

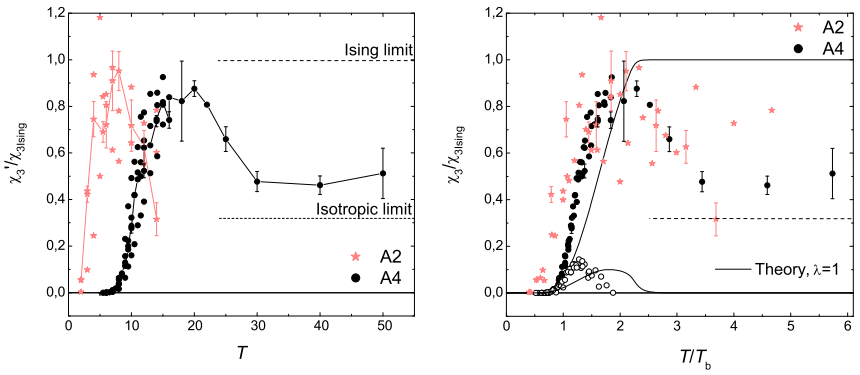

Fig. 4.12. Dynamical nonlinear susceptibility measurements normalized by their equilibrium values for Ising limit for particles with different mean diameter t_{Co}=0.2 nm and t_{Co}=0.4 nm in alumina. LEFT: Bold symbols are the real component and open symbols the imaginary part (only for A4 sample). To guide the eye, 10 Hz measurements were marked by lines. RIGHT: Data vs reduced temperature. Temperature is normalized by the values of the blocking temperature T_{b}. Error bars for $\omega/2\pi = 9$ Hz and $\omega/2\pi = 10$ Hz are shown for samples with mean diameter 1.05 nm and 1.8nm respectively. The curve is a theoretical prediction for classical spins for an overdamped value of the phenomenological damping constant λ= 1. The isotropic (high temperature) limit is also indicated.

Capping dependence

We follow the dynamical study with the study of the capping dependence on the spin dynamics. In Fig. 4.13, the Ising normalized data versus the normalized temperature for our two different size samples varying the capping (copper and gold) are shown. The alumina capped samples serve as a reference.

The behavior of the curves is analogous to that shown in the latter section. We can draw a difference between the low-temperature blocking region and the high-temperature anisotropy variation in the equilibrium region above T_{b}. In all cases, cobalt exhibits the characteristic "classical behavior" and experimental data fit in a lower bound with $\lambda = 1$, revealing an "overdamped" regime.

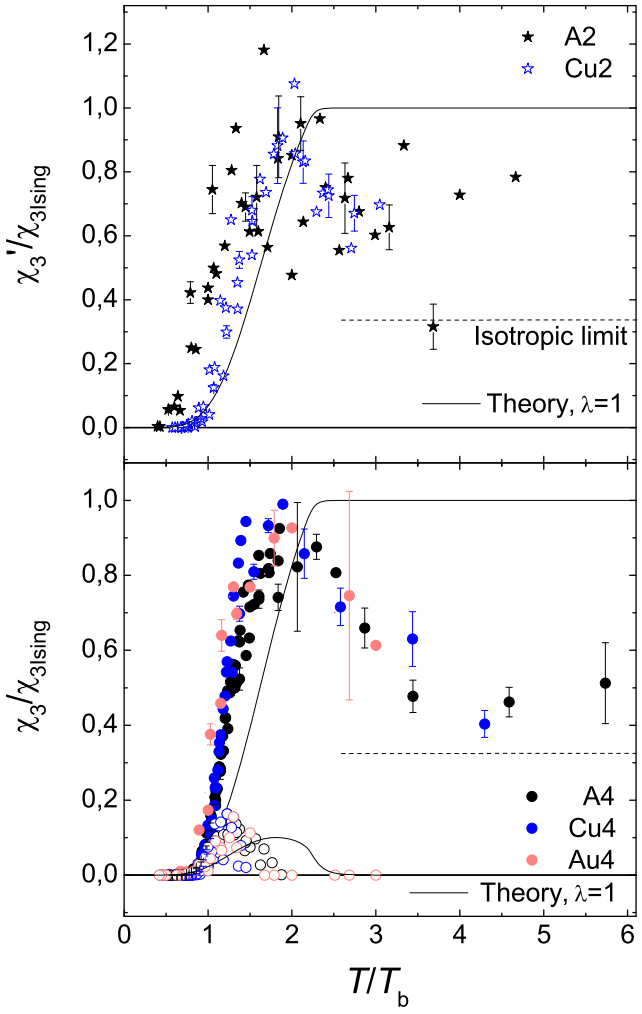

Fig. 4.13. Dynamical nonlinear susceptibility measurements normalized by their equilibrium values for Ising (low temperature) limit. Results are shown for samples with the same mean nanoparticle diameter and different environments. Upper panel: t_{Co}=0.2 nm for alumina and copper. Lower panel: t_{Co}=0.4 nm for alumina, copper and gold. Temperature is normalized by their values for blocking temperatures. Error bars for $\omega/2\pi = 9$ Hz and $\omega/2\pi = 10$ Hz are shown for samples with mean diameter 1.05 nm and 1.8nm respectively. The curve is a theoretical calculation for classical spins for an overdamped value of the phenomenological damping constant λ= 1. Isotropic (high temperature) limit is also indicated.

As a conclusion, metal capping does not change the energetic dissipation degree of these magnetic moments. No change is induced in the spin dynamics although the variation of the environment, probably due because dipolar interactions between the particles involved are the main cause of the anergy dissipation.

4.5 Conclusions

- Measurements of nonlinear susceptibility in cobalt embedded particles in insulator and metallic environments reveal, oppositely to Mn_{12}, that both χ_1' and χ_3' lie always below their respective equilibrium limits. In conclusion, the behavior of cobalt spins is eminently classical.
- Nonlinear susceptibility temperature dependence in insulator and metallic matrices clearly shows in a very sensitive way differences in temperature divergences (θ) which are ascribed to an anisotropy change induced by conduction electrons of the metallic capping. This modification may open a simple method to control magnetic behavior of nanoparticles.
- Nonlinear susceptibility reveals that, in alumina insulator matrix, cobalt nanoparticles spin dynamics are in the "overdamped" regime. Apparently, metal capping does not change the energetic dissipation degree of these magnetic moments.
- The fact that no change is induced in the spin dynamics, in spite of the variation of the environment and the anisotropy constant, let us think that the overdamped regime is intrinsic to the nanoparticles array, probably due to dipolar interactions between the particles involved. These interactions between nanoparticles will be studied in the next chapter.

5

Memory effects and "aging" in quasi-organized Co nanoparticles

5.1 Introduction: Overview and interest

In dense arrays of magnetic nanoparticles, dipolar interactions can become strong, even compared with the magnetic anisotropy energy. Under such conditions, interactions can and, indeed, do modify the magnetic behavior [Dormann 1988] [Luo 1991] [Morup 1994] [Morup 1995] [Jonsson 1995] [Dormann 1996] [Djurberg 1997] [Mamiya 1998] [Jonsson 1998b] [Mamiya 1999] [Dormann 1999] [Hansen 2002] [Luis 2002c] [Sahoo 2002] [Sahoo 2003] [Jonsson 2004] [Sasaki 2005]. The influence of interactions has obvious implications for the application of these materials to high-density magnetic storage, since recording a bit can erase the information stored previously in its neighbors. In addition to their relevance for the technological applications, interacting magnetic nanoparticles are also attractive systems for fundamental studies. Dipolar interactions operate at long distances and the interaction energy can have both positive and negative signs, depending on the distance between particles and on the relative orientations of their magnetic moments. As a result of the random arrangement of the particles and of their anisotropy axes, dipolar interactions give, therefore, rise to disorder and frustration [Luo 1991], the two necessary ingredients for spin-glass behavior [Mydosh 1993]. However, arrays of nanoparticles do also have important differences with materials considered as canonical spin-glasses, such as noble metals (Au, Ag, Pt) containing Fe or Mn impurities [Mydosh 1993]. The differences arise from the fact that nanoparticles with strong magnetic anisotropy already show slow dynamics in the absence of

interactions and from the broad dispersion of single-particle relaxation times associated with the distribution of sizes.

The existence of a true spin-glass phase in systems of nanoparticles has been subject to experimental and theoretical studies for a long time. Some reported evidences in favor of the presence of a true spin-glass phase transition are the observation of a very large peak in the nonlinear magnetic susceptibility [Jonsson 1998b] [Mamiya 1998] [Sahoo 2002], the weak dependence of the susceptibility maxima with frequency (interpreted as critical slowing down) [Djurberg 1997], and the dependence of the magnetic susceptibility on the magnetic and thermal history of the sample (usually referred to as "aging") [Jonsson 1995] [Mamiya 1999] [Dormann 1999] [Sahoo 2003] [Sasaki 2005] [Jonsson 2005]. Another related interesting question is whether "aging" phenomena are exclusive of the spin-glass phase or they can be observed in samples that do not show any clear-cut transition or for $T > T_g$, where T_g is the spin-glass freezing temperature [Fernández 2008].

From the experimental point of view, the study of these issues is far from easy. One of the difficulties is that there is usually little control over parameters, such as the size and spatial arrangement of the particles, which define the strength of dipolar interactions. In addition, samples contain a distribution of particle shapes and sizes, which gives rise to a very broad distribution of relaxation times, even for non-interacting nanoparticles. As a result, the region of temperatures close to the spin-glass freezing temperature T_g is experimentally inaccessible [Djurberg 1997] [Mamiya 1998] [Jonsson 1998b] [Sahoo 2002] thus rendering critical scaling analysis of doubtful value for these materials. Finally, surface effects and the possible aggregation of nanoparticles in e.g. colloidal samples might also influence the magnetic properties.

For the reasons mentioned above, experiments performed on well characterized samples, for which the relevant parameters are known and can be varied in a controlled way are highly desirable. The samples of Co clusters that we have introduced in the previous chapter do certainly possess very appealing properties. The average particle size is well characterized by TEM and magnetic measurements, and it can be varied within a rather wide range. In addition, size distributions are relatively narrow [Maurice 1999] [Luis 2002b]. But perhaps the most important aspect is related with the spatial arrangement of the nanoparticles. Early studies show that when nanoparticles grow in each

of the layers, they keep an approximately constant distance between their boundaries [Maurice 1999]. This gives rise to very homogeneously dispersed arrays of clusters. In addition, for some values of the nominal Co thickness t_{Co}, clusters in adjacent layers tend to self organize in a structure that, at short distances, looks like a closed-packed hexagonal lattice of nanospheres [Babonneau 2000] [Luis 2002b]. The average number of nearest neighbors can be varied by changing the number of layers whereas the interaction between the layers can be controlled by modifying their relative distance, determined by the thickness of the alumina layer that separates them.

The goal of the work presented in this chapter is to investigate in detail the glassy dynamics and "aging" phenomena in these model systems. We have studied how these phenomena depend on sample parameters such as particle size, number of layers and their separation, as well as on temperature and magnetic field. Notice that the influence of interactions on the magnetic response of nanoparticles is usually measured by the temperature-independent coefficient h_{d} defined as [Jonsson 2001b] [Jonsson 2004]:

$$h_{\mathrm{d}} = \frac{E_{\mathrm{dip}}}{2U} \tag{5.1}$$

where $E_{\mathrm{dip}} \equiv \mu^2/a^3$. U is the anisotropy energy barrier, μ is the magnetic moment of the particle and a is the distance between the dipoles. This parameter gives the magnetic dipolar field created by a nearest neighbor particle in units of the anisotropy field. When $h_{\mathrm{d}} << 1$, the magnetization dynamics should be dominated by the energy barriers associated with the anisotropy. As h_{d} approaches unity, collective magnetic phenomena and "aging" are expected to come to the fore. As we discussed in the previous chapter, the anisotropy field depends on particle size, due to surface effects. The samples employed in our study enable us to vary h_{d} by modifying either the anisotropy and the interparticle interactions and to investigate how the "aging" phenomena are then affected.

The chapter is organized as follows. In the next section 5.2, we describe how much the interaction strength (measured in terms of the parameter h_{d}) can be varied experimentally and the experimental measurements to estimate "aging" effects. The magnetic "aging" of the ZFC susceptibility has been measured using a method that was first applied to spin-glasses [Mathieu 2001b] and more recently applied also to ensembles of interacting nanoparticles (see e.g. references

[Jonsson 2004][Sasaki 2005][Chen 2005][Petracic 2006]). The following section 5.3 contains the results of "aging" experiments: we have performed a comparative study of the degree of "aging" as a function of particle size, between $D \simeq 1.3$ nm and 7.5 nm, and as a function of the number of layers and their separation for $t_{\mathrm{Co}} = 0.7$ nm ($D \simeq 2.6$ nm). For all these cases, we have investigated "aging" in the whole range of temperatures above and below the expected T_{g}. Section 5.4 is devoted to discuss the relationship of these phenomena with the existence of a spin-glass phase as well as other alternative explanations. The last section is devoted to list the main conclusions of this work.

5.2 Experimental method

As we have just mentioned, we shall investigate how collective magnetic phenomena change as we move from the strong anisotropy limit ($KV \gg E_{\mathrm{dip}}$) to the situation in which they become comparable. Thus, the question to be solved is: can we, modifying size or adding layers, control the strength of interactions? and can we measure physical quantities just caused by these interactions? The two following sections aim to respond to these two essential questions.

5.2.1 Samples: Can we control interactions?

Interactions vs particle's size

We have prepared several series of samples with different values of t_{Co}. It is known that the average particle's size increases with t_{Co} whereas the magnetic anisotropy constant decreases. At the same time, inside each layer the distance between nearest neighbor particles remains approximately constant. Thus, by increasing t_{Co} we expect to gradually switch from a situation in which the characteristic energy scale of dipolar interactions is much smaller than the anisotropy energy to the situation where both energy scales become comparable. The samples show superparamagnetic behavior, with a blocking temperature that increases with increasing t_{Co} as it's shown in the ZFC magnetization in Fig. 5.1. From magnetic measurements, chiefly ZFC-FC susceptibility curves and magnetization isotherms, we can obtain information on the average particle size and its distribution, as well as on the strength of dipolar interactions and how they change with t_{Co}.

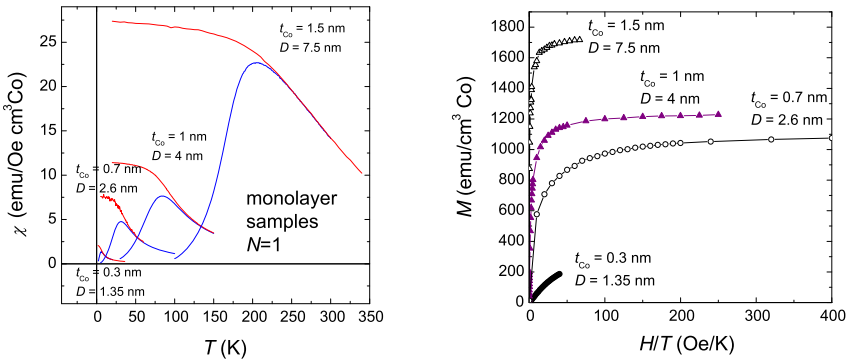

Fig. 5.1. LEFT: ZFC (blue) and FC (red) magnetization curves for monolayer samples with different diameters (different t_{Co}). RIGHT: field-dependence magnetization isotherms for the same samples.

A way to estimate how the strength of interactions depends on t_{Co} is by comparing the value of the Weiss temperature obtained by fitting a Curie-Weiss law (Eq. 3.5) to the equilibrium susceptibility data measured above T_{b}. The value of the Weiss temperature provides a measure of E_{dip} [Jonsson 2001b]. We observe that θ increases with particle's size, becoming comparable to T_{b} (that measures the activation energies required for the magnetization reversal) for the largest particles. For samples with t_{Co}=0.3 nm, θ contains large experimental uncertainties.

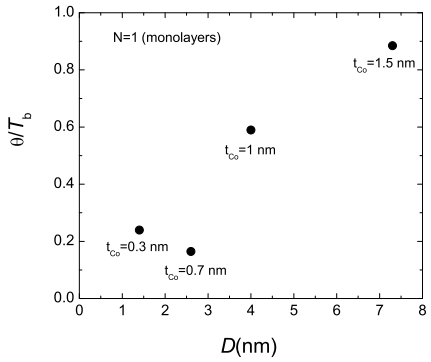

Fig. 5.2. θ/T_{b} ratio versus particle diameter for granular Co monolayers. The cobalt nominal thickness used for preparation is indicated next to each experimental point.

This behavior can be qualitatively understood if we take into account the spatial organization of the nanoparticles in the layers. From TEM, it was found that the nanoparticles cover homogeneously the substrate, maintaining a nearly constant (i.e. independent of t_{Co}) distance of about 2.2 nm. Therefore, the characteristic energy of interaction between two nearest neighbor particles is

$$E_{\mathrm{dip}} \approx \frac{\mu^2}{(D+2.2)^3} \qquad (D \,\mathrm{in\,nm}) \tag{5.2}$$

whereas the anisotropy energy of each cluster contains contributions from the inner atoms and from those located at its surface

$$U_{\mathrm{anis}} \approx K_{\mathrm{bulk}} V \left[(1-f) + f \frac{K_{\mathrm{s}}}{K_{\mathrm{bulk}}} \right] \tag{5.3}$$

with K_{bulk} being the anisotropy of bulk fcc Co, $f = 1-(1-0.4/D)^3$ the fraction of all atoms that lie at the cluster's surface, and K_{s} their anisotropy. From previous studies, if follows that $K_{\mathrm{bulk}} \approx 25 K_{\mathrm{s}}$ [Luis 2006]. It follows that $E_{\mathrm{dip}}/U_{\mathrm{anis}}$ should indeed increase with D, which qualitatively accounts for the observed increase of θ/T_{b}.

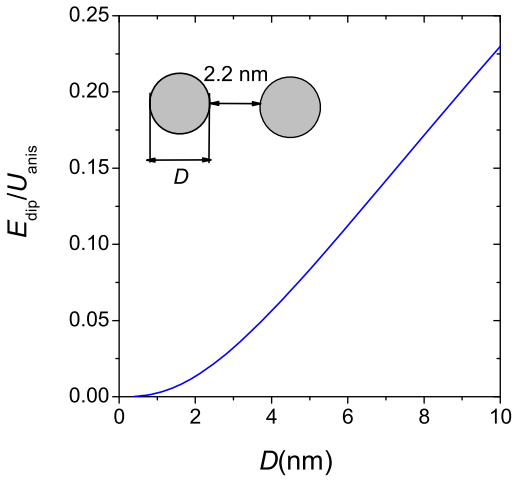

Fig. 5.3. Balance between the dipolar energy and the anisotropy barrier ($E_{\mathrm{dip}}/U_{\mathrm{anis}}$)in a monolayer (N=1) vs different nanoparticle diameter.

The conclusion is that varying t_{Co}, thus the average size of the clusters, we can indeed modify the relative strength of dipolar interactions with respect to the magnetic anisotropy.

Interactions vs number of layers

A simple way to modify just the effect of dipolar interactions is by changing the number of neighbors that each cluster has. With our preparation method, this can be achieved by increasing the number N of Co layers deposited. For t_{Co}=0.3 nm, 0.7 nm, 1 nm, and 1.5 nm we have prepared a series of samples with N varying from 1 (i.e. a single layer) to 20 (15 for t_{Co}=1.5 nm). For the last three, magnetization and susceptibility measured above T_b (see Fig. 5.4) suggest that all samples belonging to each series have approximately the same average size and distribution. Unfortunately, for the series with t_{Co}=0.3 nm, the same experiments evidence that the average diameter increases by more than 70% from the sample with N=1 to that with N=20. Therefore, we have excluded these series from the analysis that follows.

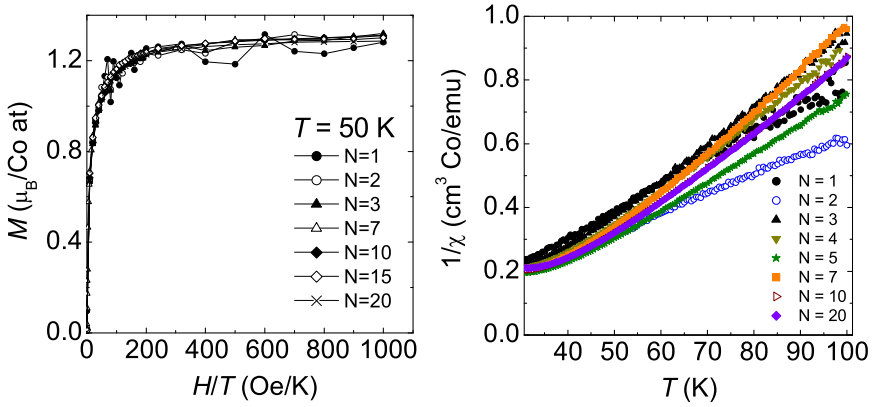

Fig. 5.4. LEFT: magnetization isotherms above blocking temperature (T=50 K) for samples with t_{Co}=0.7 nm and different number of layers. RIGHT: temperature dependence of the reciprocal equilibrium susceptibility (Eq. 3.5) for $T > 30$ K.

A remarkable fact (shown in Fig.5.5) is that for t_{Co}=0.7 nm, the addition of extra layers from N=1 to N=20 has a sizeable effect in $\theta/\theta(N=1)$ which increases by a factor 5. For t_{Co}=1 nm, it increases by about 20% only, whereas for the largest nanoparticles no change can be discerned in θ. This result seems to indicate that, for t_{Co}=0.7 nm, interactions between particles in adjacent layers are strongest, whereas for the other two series of samples, interactions within each layer become largely dominant.

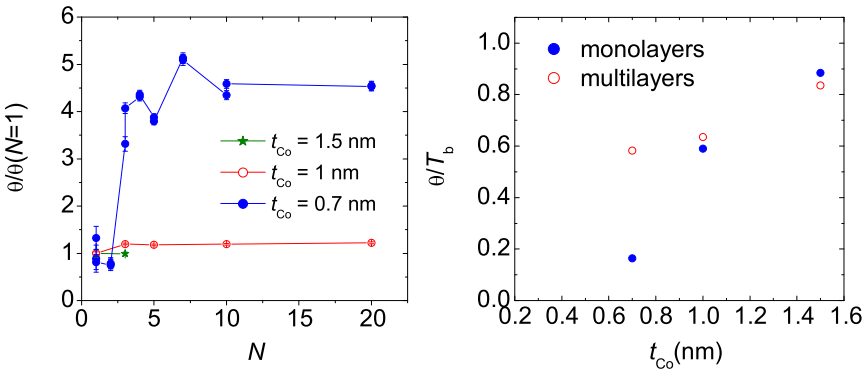

Fig. 5.5. LEFT: θ normalized by θ in the monolayer values vs N for different normal thicknesses (t_{Co}). RIGHT: θ normalized by T_{b} vs t_{Co} for monolayer and multilayer samples.

In conclusion, the answer to the question raised at this section's title is positive. By changing some of the deposition parameters, viz. t_{Co} and N, it is possible to control the strength of dipolar interactions relative to the anisotropy energy, that is, we have control over the parameter h_{d} defined in equation 5.1.

5.2.2 Magnetic measurements

In order to characterize the influence that inter-particle interactions have on the magnetization dynamics, we have performed waiting-time memory experiments on the ZFC susceptibility [Jonsson 2004] [Sasaki 2005]. This method offers some advantages:

- Memory effects are linked to the presence of interactions. By contrast, the relaxation rates and the blocking temperatures depend also on the size-dependent magnetic anisotropy.
- These effects are considered as a clear signature of magnetic correlations, i.e. the existence of collective magnetic relaxation or spin-glass behavior [Sahoo 2003] [Sasaki 2005].

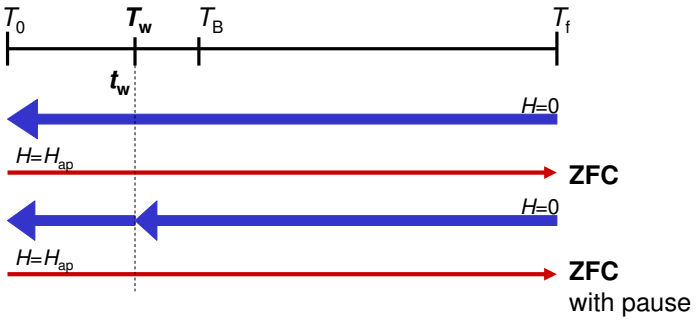

Fig. 5.6. Schematic diagram of ZFC measurement with and without pause.

The experimental method employed by us is as follows in [Mathieu 2001a]. The ZFC susceptibility of each sample was measured after performing two different cool-down protocols. In the first of these, the sample is simply cooled down from a temperature well above the superparamagnetic blocking temperature T_b at constant speed. Then, a small dc magnetic field (H=10 Oe in most of the experiments shown below) is applied and the magnetization M_{ZFC} is recorded as T increases. The second experimental procedure is the same but includes a pause in the cooling down process. The pause is performed at a fixed waiting temperature $T_w < T_b$ for a period t_w. The magnetization is denoted by $M_{ZFC,w}$. The measurement routine is shown in Fig. 5.6. The quantity of interest is the difference $\Delta M = M_{ZFC} - M_{ZFC,w}$ between the susceptibilities measured by these two protocols. An example of the results is shown in Fig. 5.7.

From the experimental point of view, these experiments are not trivial. It is crucial that all experiments are performed using exactly the same rates for cooling and warming the sample [Mathieu 2001b]. In addition, the waiting time is sometimes limited from below by the existence of unavoidable delays in the equilibration of the attempted temperatures. Last, detecting the small (of order 3-10 %) ΔM requires measuring each susceptibility curve with a very high degree of accuracy.

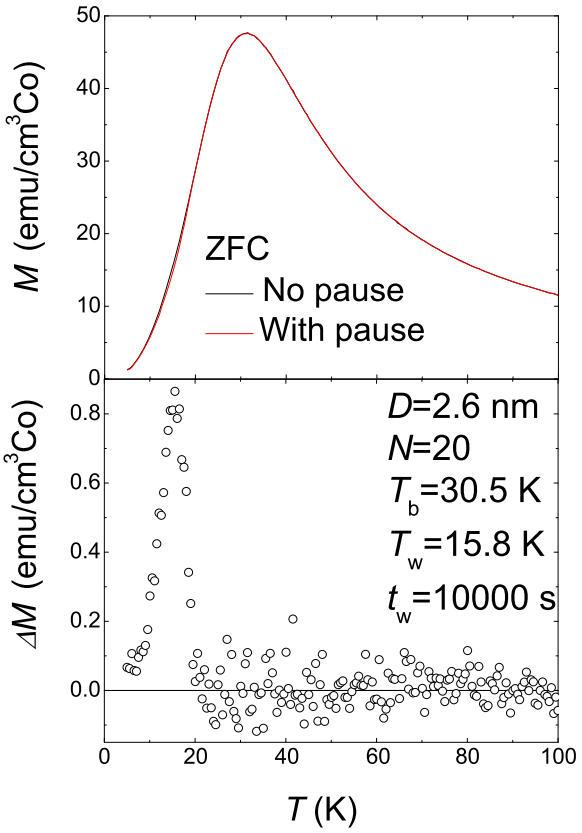

Fig. 5.7. Measurement of memory effect obtained for a multilayer with t_{Co}=0.7 nm and N=20. Black line: measurement after ZFC standard protocol. Red line: measurement after ZFC with pause protocol. In lower panel we can see the difference between the two curves.

The difference ΔM shows a peak centered near T_w. Changing T_w results in a shift of the peak (see Fig. 5.8) thus showing that this peak is associated with the pause and not to any experimental artifact.

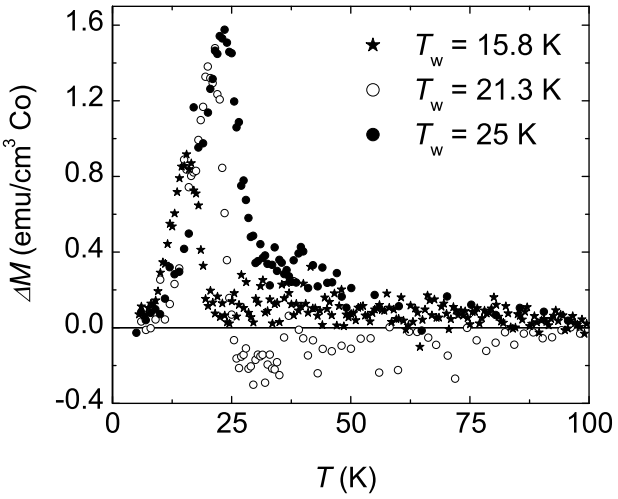

Fig. 5.8. ΔM for three different waiting temperatures. Sample with t_{Co}=0.7 nm and N=20. Waiting time (t_w) was 10000 s and applied field (H_{ap}) was 10 Oe.

We can also check the relationship between ZFC, FC and remanent magnetization measurements performed using the same waiting-time protocols. The last two measurements are performed after cooling the sample in the presence of a magnetic field (H_{ap}=10 Oe in the examples shown). They differ by the fact that FC magnetization measurements are recorded with the magnetic field on, whereas the remanent magnetization is measured after the field is switched off at $T = T_0$. The differences ΔM_{ZFC}, ΔM_{FC} and ΔM_r must fulfill the following relation

$$\Delta M_{FC} = \Delta M_r + \Delta M_{ZFC} \tag{5.4}$$

that has been shown to hold for spin-glasses [Mathieu 2001b]. As Fig. 5.9 shows, it is also fulfilled by our nanoparticle systems.

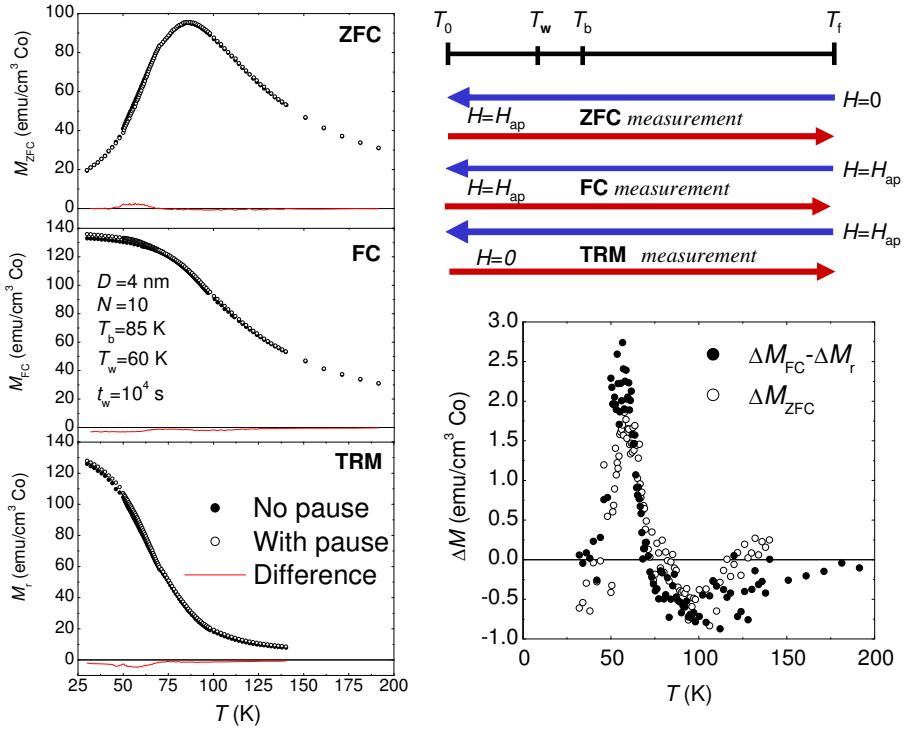

Fig. 5.9. LEFT: open symbols: different protocol measurements without pause. Solid symbols: different protocol measurements with pause at 60 K. Red lines: $\Delta M_{\rm ZFC}$, $\Delta M_{\rm FC}$ and $\Delta M_{\rm r}$. Sample with $t_{\rm Co}$=1 nm and N=10. Waiting time ($t_{\rm w}$) was 10000 s, waiting temperature ($T_{\rm w}$) was 60 K and applied field ($H_{\rm ap}$) was 10 Oe. RIGHT: representation that evidences the relation 5.4.

Understanding these phenomena, at least qualitatively, is relatively simple. Let's first consider the ZFC susceptibility. When the sample is cooled in zero field, the initial magnetic configuration at T_0 will be one of the many that correspond to a zero net magnetization for the whole sample. In the presence of inter-particle interactions, these configurations are no longer equivalent, in the sense that different mutual spin arrangements will result in different free energies F for the array. If the sample is kept at a fixed temperature $T_{\rm w}$ for some time, the spins will tend to reorient themselves to attain a new configuration with increasingly lower $F(T_{\rm w})$. Then, once the sample is cooled down to T_0, this configuration will be quenched. Since a lower energy configuration is associated with a lower susceptibility, the second method will give rise to a lower magnetic response in the neighborhood of $T_{\rm w}$, as it is indeed

observed. This process is denominated as "burning a hole" in the susceptibility. For the FC and remanent magnetization, by contrast, the magnetization increases during the pause because the sample is subject to a nonzero external magnetic field. They differ from each other by the response to the applied magnetic field, which is zero in the latter case. This response is obviously the ZFC susceptibility, which explains why equation 5.4 must hold.

5.3 Dependence of magnetic memory effects

5.3.1 Waiting time dependence

As we have discussed in the previous section, making a pause at an intermediate temperature T_w "burns a hole" in the ZFC susceptibility. The height of this "hole" is a measurement of how much the spin array has approached its equilibrium configuration or, in other words, how much correlations between neighboring spins have grown [Sasaki 2005]. It is therefore expected that the maximum ΔM (hereafter referred to as simply ΔM) increases with increasing t_w. This is indeed observed in Fig. 5.10.

Remarkably, it seems that ΔM remains finite for very short waiting times. Yet, this behavior is probably due to the fact that, as we have already mentioned, the time it takes to stabilize the temperature of the sample + thermometer at T_w exceeds 200 seconds. Therefore, it is in practice not feasible to explore the behavior at shorter times. In the accessible time window, ΔM increases approximately logarithmicaly with time.

5.3.2 Waiting temperature dependence

In Fig. 5.11, we show the dependence of ΔM on the temperature at which the pause is established. Logically, ΔM is very small at low temperatures and it increases with T_w, since the relaxation processes by which spins rearrange themselves in order to decrease $F(T_w)$ are thermally activated. However, when T_w approaches T_b, the magnetic relaxation times become comparable to the experimental time $t_{exp} \sim$ 100 s, i.e. to the time that the system stays at $T \approx T_w$ during a conventional cooling down process. Obviously, for $T_w >> T_b$, ΔM should vanish again, as it does at very low T_w, but for the opposite reason: at low T_w, $\Delta M \approx 0$ because very little correlations can be established

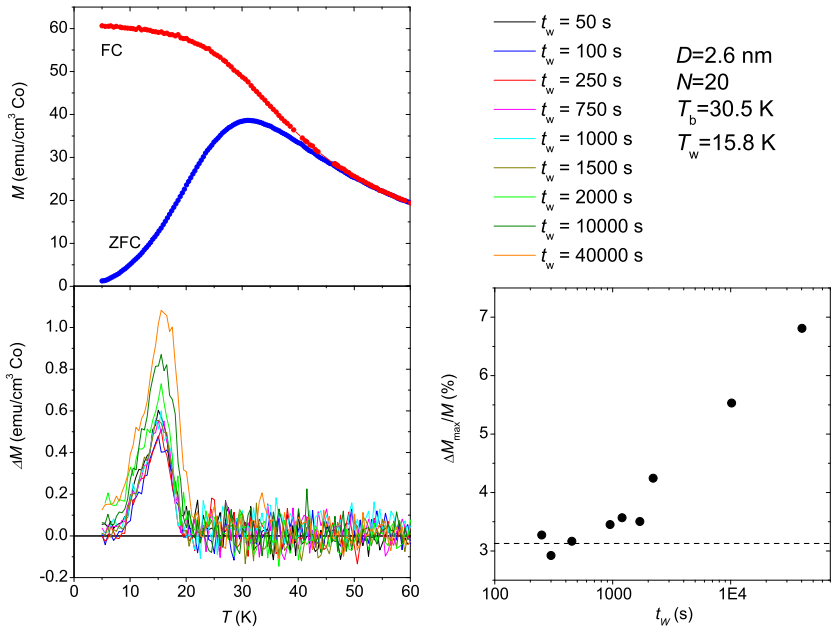

Fig. 5.10. LEFT: ΔM at different waiting times ($t_{\rm w}$) in a sample with $t_{\rm Co}$=0.7 nm and N=20. Waiting temperature ($T_{\rm w}$) was 15.8 K and applied field ($H_{\rm ap}$) was 10 Oe. RIGHT: extracted maxima ΔM normalized by the magnetization value versus the waiting time ($t_{\rm w}$). Dashed line: threshold of observation because of experimental time window.

between t_{exp} and $t_{\rm w}$. For $T_{\rm w} >> T_{\rm b}$, $\Delta M \approx 0$ for the simple fact that most correlations are already established before $t = t_{exp}$. This explains the decrease of ΔM for $T_{\rm w} > 21$ K and the existence of a maximum at a temperature 0.7-0.8 $T_{\rm b}$.

If this interpretation is correct, the maximum of the ΔM should approximately take place at the blocking temperature for an experimental time equal to $t_{\rm w}$ (10^4 s in the example shown). More explicitly, it corresponds to the condition $t_{\rm w} = \tau$, where τ is the characteristic relaxation time. Notice that the same condition applies to the maximum of the imaginary component χ'' of the ac susceptibility, but then the experimental time equals the reciprocal angular frequency $1/\omega$, and are therefore much shorter than $t_{\rm w}$. In Fig. 5.12, we show data of τ vs $1/T$ obtained from χ'' vs T data. They follow the well-known Arrhenius

law $\tau = \tau_0 \exp(U/k_B T)$, with a very short τ_0, indicative of the strong influence of inter-particle interactions. The temperature at which ΔM shows a peak agrees well with the extrapolation of this Arrhenius law when $\tau = t_w$, giving thus support to our interpretation.

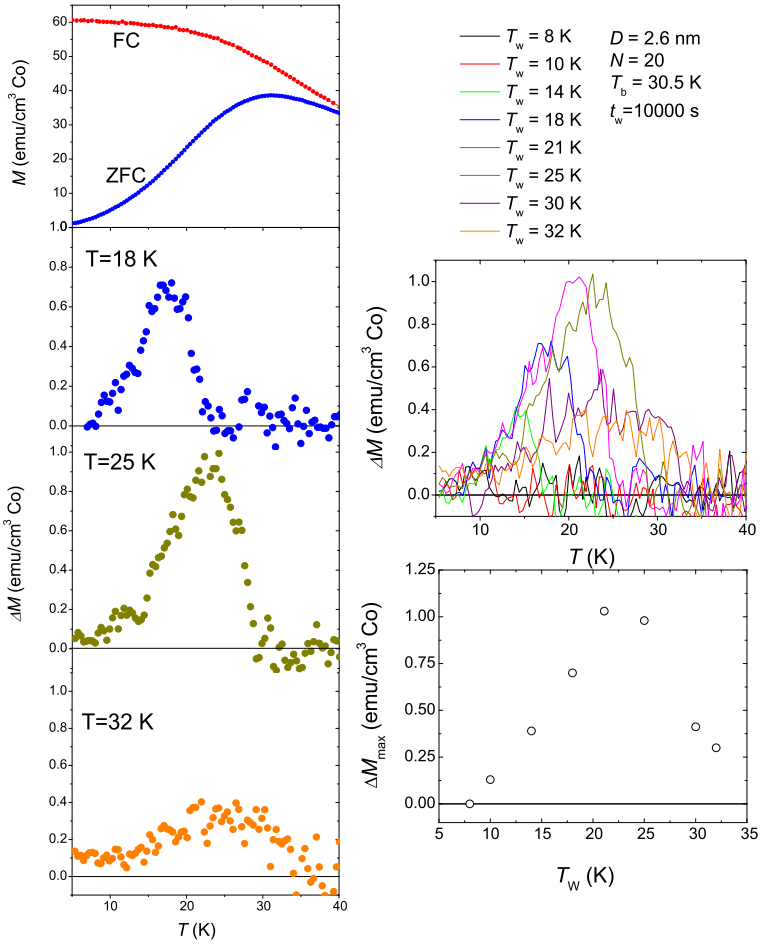

Fig. 5.11. LEFT: ΔM at different waiting temperatures (T_w) in a sample with t_{Co}=0.7 nm and N=20. Waiting time (t_w) was 10000 s and applied field (H_{ap}) was 10 Oe. RIGHT: extracted maxima ΔM versus the waiting temperature (T_w).

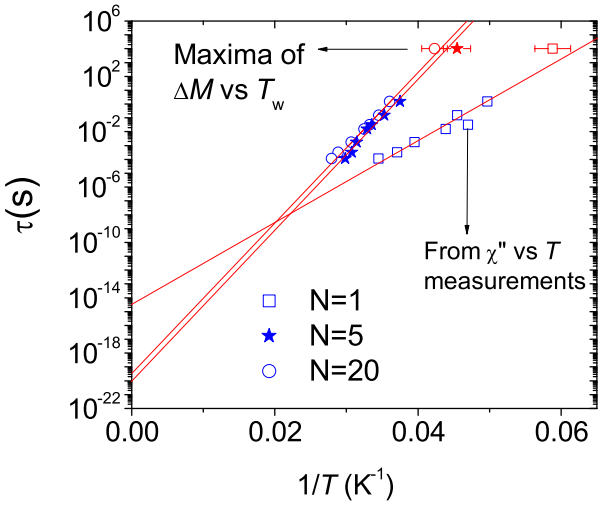

Fig. 5.12. Blue symbols are τ vs $1/T$ data obtained from ac frequency-dependent susceptibility measurements χ'' vs T. The lines are least-squares fittings using Arrhenius law. Red symbols are the blocking temperatures for an experimental time equal to t_w (10^4 s) extracted from the maximum of the ΔM vs T.

5.3.3 Particle's size dependence

We have seen that, by increasing the average particle size, the strength of interactions can be made comparable to the magnetic anisotropy. We expect then that the enhancement of interactions will reflect itself in the amplitude of the "hole" burnt into the ZFC magnetization curve. One important related question that can be investigated by these experiments is whether collective memory effects show up only above a certain threshold of the parameter h_d. To see this, we have studied memory effects in samples with diameters comprised between 1.35 nm and 7.5 nm. All samples consist of a single layer, with the exception of the sample containing the smallest samples, where a multilayer was chosen to get a measurable signal.

We have seen in the previous sections that ΔM depends on the ratio T_w/T_b. In addition, the magnetic susceptibility also increases with size. Therefore, in order to do a proper comparison, we performed, for each sample, measurements of ΔM at different temperatures. The results are shown in Fig. 5.13, where ΔM is given as the relative change of the

susceptibility. The results are rather surprising because the maximum of ΔM vs $T_{\rm w}$ does not increase with increasing particle's size, as it would be expected. Our data suggest that increasing significantly the strength of interparticle interactions with respect to the single-particle anisotropy does not significantly enhance the magnetic correlations. On the other hand, signatures of collective magnetic behavior are observed even in the limit of very small dipolar interactions.

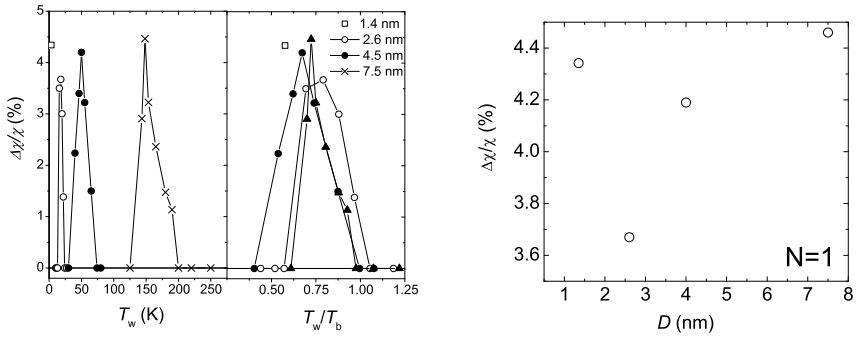

Fig. 5.13. LEFT: normalized susceptibility increment vs the waiting temperature for monolayer samples of different diameters. RIGHT: normalized susceptibility increment maxima are shown vs the particle diameter. For all samples: $t_{\rm w}$=10000 s and applied field was 10 Oe.

5.3.4 Number of layers dependence (nearest neighbors)

An even simpler way to modify the strength of interactions is by changing the number of nanoparticles surrounding a given one. As we have explained at the beginning of this chapter, the sequential sputtering of alumina and Co layers enables this, by simply controlling the number of Co layers. We have also seen that increasing N changes significantly the value of the Weiss temperature θ, which provides a way of measuring the interactions strength, for $t_{\rm Co}$=0.7 nm. In a previous work performed in our group, it was shown that increasing N leads to clear changes in the magnetization dynamics [Luis 2002c]. Indeed, as it is shown in Fig. 5.14, the blocking temperature increases by 40% as N increases from 1 to 20. Remarkably enough, the change tends to saturate to a constant value for large N, indicating that interactions with

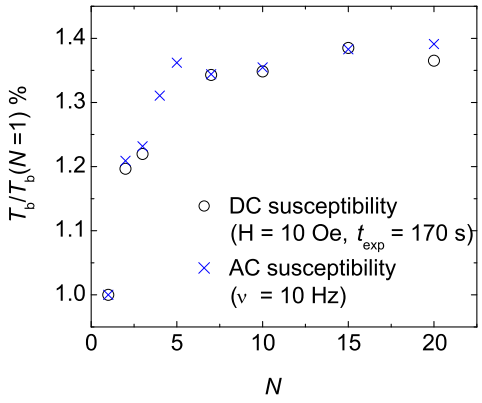

Fig. 5.14. Blocking temperature variation with the number of layers, N, for samples with t_{Co}=0.7 nm. Data precedence was imaginary susceptibility maxima from ac measurements (stars) and dc measurements (circles).

nearest neighbors play the dominant role in modifying the relaxation rates.

Varying the number of layers offers a rather unique opportunity for the study of collective phenomena in the magnetization dynamics. In a single layer, correlations can only grow along two directions in space. Therefore, by adding layers we can control the spatial confinement of correlations along the direction of growth. In this way, we aim to study the extension of such dynamical correlations or, in other words, answer the question formulated in this chapter's title on how collective these magnetization processes are. Results of waiting time experiments performed on the whole series for a fixed T_w=15.8 K are shown in the following Fig. 5.15.

We observe that ΔM decreases with increasing N, and in fact it becomes nearly constant for $N \geq 3$. This a priori surprising result can be easily understood since, for a fixed T_w, the magnetic relaxation times become longer as N increases (as revealed by the increase of T_b with N). This highlights the need, already mentioned when we discussed the study of ΔM vs particle diameter, to measure ΔM vs T_w in order to make a proper comparison between samples with different blocking temperatures.

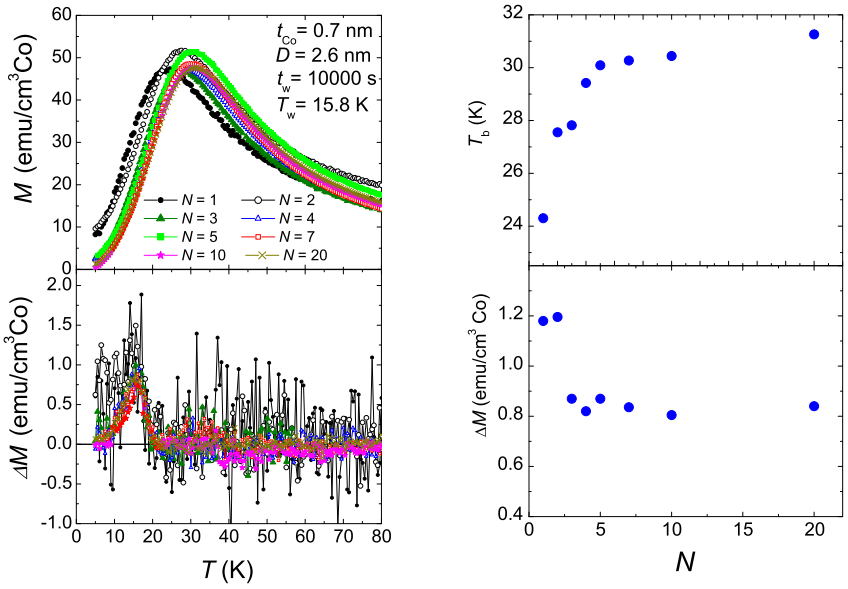

Fig. 5.15. LEFT: ΔM for samples with t_{Co}=0.7 nm and different number of layers. RIGHT: ΔM maxima is represented vs the number of layers for a fixed temperature T_{w} =15.8 K.

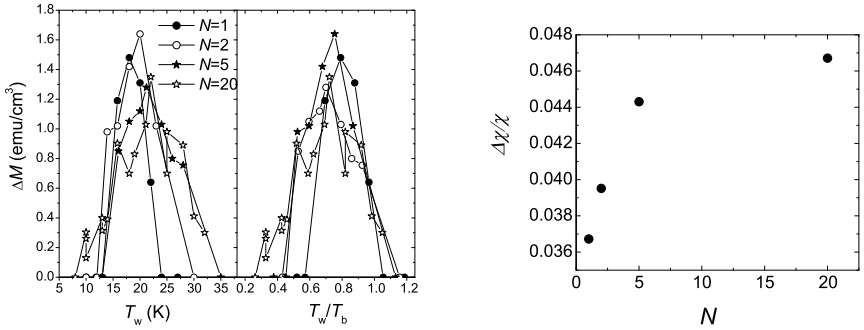

Fig. 5.16. LEFT: ΔM vs T_{w} for samples with t_{Co}=0.7 nm and different number of layers. RIGHT: ΔM temperature maxima are represented vs the number of layers.

Remarkably enough, as is shown in Fig. 5.16, the normalized values $\Delta\chi/\chi$ are approximately proportional to the number of nearest neighbors. The correlations between the particles are mainly restricted to the shell of nearest neighbors.

5.3.5 Correlation suppression by external magnetic field

We have also explored how the relative magnitude of $\Delta M/M$ depends on the field applied to perform the ZFC experiments (Fig. 5.17). We observe that $\Delta M/M$ rapidly drops as H increases. This reflects the fact that magnetic correlations and, in general, any influence that interactions have on the magnetic response of nanoparticles are suppressed when external fields stronger than the typical dipolar fields are applied to the sample. This result is in agreement with [Luis 2003], which show how the blocking temperature approaches the noninteracting behavior when a bias magnetic field is applied.

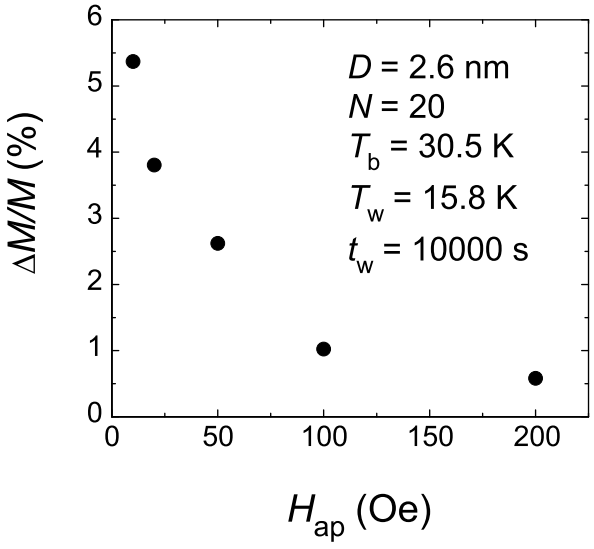

Fig. 5.17. Reduced susceptibility peak variation respect applied field in a sample with N=20 D=2.6 nm.Measurement parameters were T_{w}=15.8 K and t_{w}=10000 s.

5.4 Discussion: Is there a spin-glass phase?

The results of the preceding section show that aging phenomena are ubiquitous to a wide range of situations. In the light of these experiments, a question that we would like to address in this section is whether aging is indicative of a spin-glass phase, as has been suggested in recent times [Sasaki 2005] [Sahoo 2003]. Perhaps the most clear-cut situation to discuss the existence of a "true" spin-glass phase transition and its experimental manifestations is offered by the study of single layers of nanoparticles, i.e. the samples with $N = 1$. For two-dimensional systems, it is generally accepted that $T_g = 0$, that is, there is no spin-glass phase at finite temperatures. As we have shown in the previous section, we nevertheless observe aging phenomena in these samples. A detailed example is shown in Fig. 5.18, where the effects that making a pause during the cooling down protocol have on the ZFC and FC susceptibilities as well as on the remanent magnetization are displayed. The overall qualitative behavior is completely analogous to what we observe in multilayers of particles of the same average size (right-hand plot on the same figure) or even in samples with larger particles (compare Fig. 5.18 with Fig. 5.9 that corresponds to a sample with $N = 10$ and $t_{Co} = 1$ nm).

The same applies to single layers of larger particles as well. They all show "aging" of their magnetic response (see e.g. Fig. 5.13), and the way these phenomena depend on temperature, time and magnetic field is qualitatively the same as what is found for the three-dimensional arrays. This clearly indicates that the aging of 2D systems of interacting nanoparticles, where there is in principle no phase transition, does not differ dramatically from the aging observed in the three-dimensional limit.

Our experiments enable us to dwell a little bit further into how the lattice dimensionality modifies the growth of magnetic correlations during the aging of the system. By changing the number of layers we can in fact confine the extent of correlations along one direction, and therefore study their growth in a very controlled manner. The series of samples prepared with $t_{Co} = 0.7$ nm (average $D = 2.6$ nm) is specially well suited for this study, since the interaction between nanoparticles in adjacent layers appears to be dominant (see [Luis 2002a] and Fig. 5.14). The results have been shown in Figs. 5.15 and 5.16. They show that the maximum $\Delta M/M$ first increases when one or two layers are added to a single one, but then it saturates very rapidly to a nearly

constant value as N increases further. In fact, if we plot the same data as a function of the average number $N_\perp$ of nearest neighbors that a particle has in adjacent layers (Fig. 5.19), the result is that $\Delta M/M$ increases linearly within the experimental uncertainties.

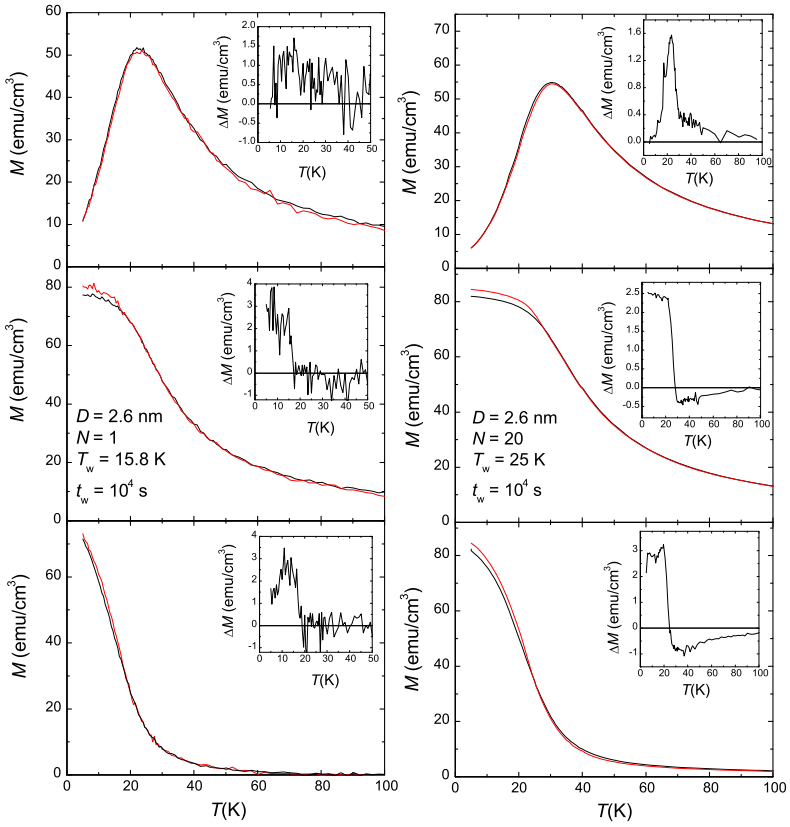

Fig. 5.18. ZFC, FC and thermoremanence curves with (red) and without (black) pause. In the inset $\Delta M_{\rm ZFC}$, $\Delta M_{\rm FC}$ and $\Delta M_{\rm r}$ are represented. LEFT: Sample with $t_{\rm Co}$=0.7 nm and N=1. $T_{\rm w}$ was 15.8 K. RIGHT: Sample with $t_{\rm Co}$=0.7 nm and N=20. $T_{\rm w}$ was 25 K. For both samples, waiting time ($t_{\rm w}$) was 10000 s and applied field ($H_{\rm ap}$) was 10 Oe.

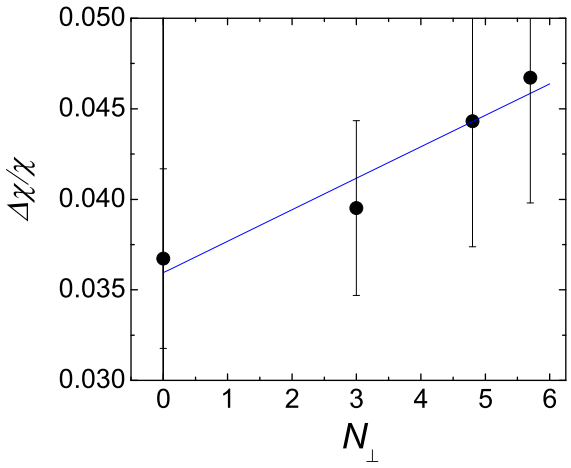

Fig. 5.19. Maximum $\Delta\chi/\chi$ as a function of the average number of nearest neighbors that a particle has in adjacent layers for samples with $t_{\mathrm{Co}} = 0.7$ nm (average $D = 2.6$ nm) and different number of layers N.

Another indication that points along the same direction is given by experiments performed on samples with well separated layers. In Fig. 5.20 , we compare data obtained from "aging" experiments for a single layer of 2.6 nm particles with those obtained for a $N = 20$ multilayer in which the interlayer separation is $t_{\mathrm{Al_2O_3}} = 10$ nm. Besides the obvious improvement in the signal to noise ratio for the latter, they agree very well. Also the blocking temperature and other parameters agree. Above all, this shows that magnetic correlations between neighboring planes are virtually suppressed when these planes are separated by a distance larger than the separation between nanoparticles in the plane. This obviously agrees with the fact that the addition of more than one or two layers contributes very little to increase the amplitude of the magnetic "aging". Apparently, correlations do not extend over very long distances but they are instead, rather, short-ranged.

These results provide therefore a strong indication that, for time scales of the order of 10^4 s, correlations are mainly established with just the first shell of nearest neighbors. A similar dependence on N was observed for the blocking (or "freezing") temperature. This experimental finding is in striking contrast with estimates, based on the theory of spin-glasses, which for similar systems of nanoparticles give correlation

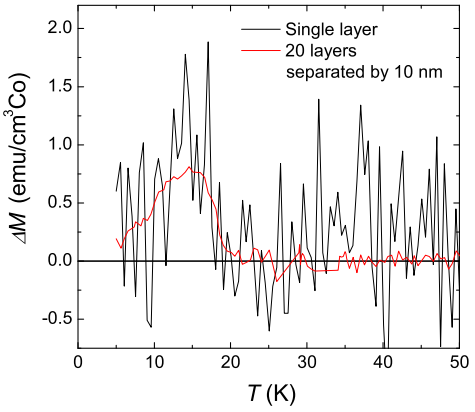

Fig. 5.20. "Aging" experiment using the with and without pause ZFC protocol for a single layer of 2.6 nm particles (black line) compared with those obtained for a $N = 20$ multilayer in which the interlayer separation is $t_{Al_2O_3} = 10$ nm (red line).

lengths extending to more than 10^3 nanoparticles [Sahoo 2003]. We can apply the same analysis to our experimental situation. The correlation length after time t_w is estimated using a simple power-law dependence:

$$\xi(t^*, T_w/D) \sim (t^*)^{\alpha(T_w)} \tag{5.5}$$

where $t^* = t_w/\tau(T_w)$ is a dimensionless timescale, the exponent $\alpha = 0.17(T_w/T_g)$, and τ is the typical relaxation time at the given temperature. For thermally activated dynamics, $\tau = \tau_0 \exp(U/k_B T_w)$. Inserting here $\tau_0 \sim 10^{-11}$ s, $T_g = 25.5$ K (see below), and $U \simeq 500$ K, this gives $\lambda \simeq 6D = 15.6$ nm, which would involve about $(\xi/D)^3 \simeq 215$ nanoparticles. By contrast, our experiments point to a much shorter (in any case much shorter than 10 nm) correlation length.

The close similarity in the time-dependent magnetic response of 2D and 3D arrays is not just restricted to aging. Most of the properties that are usually employed to ascertain the existence of a spin-glass transition look just the same. One of these is the FC susceptibility. For superparamagnets, it increases monotonically as temperature decreases, whereas the observation of saturation or even a slight decrease just below the cusp of the ZFC curve is interpreted as an indication of superspin-glass behavior [Mamiya 1998][Jonsson 2005]. In Fig. 5.21 we show the ZFC-FC curves, measured with no stops during cooling, for

a single layer and a multilayer ($N = 15$) of the largest nanoparticles [$D = 7.5(3)$ nm] that we have investigated. The two FC curves show the same degree of "flattening" at low temperatures.

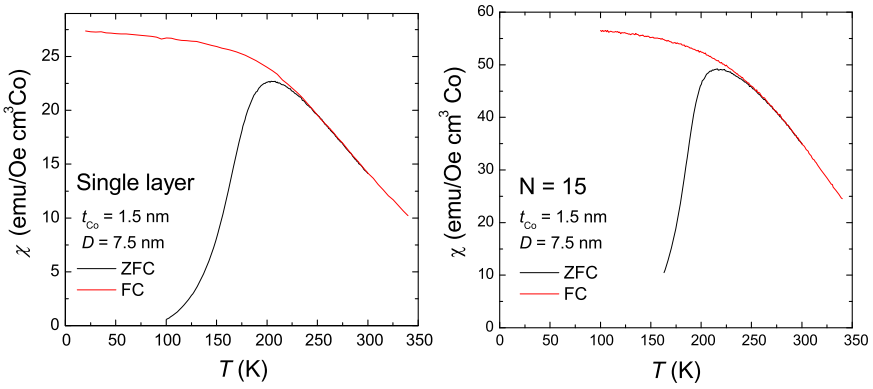

Fig. 5.21. ZFC (black line) and FC (red line) curves for a N=1 single layer (LEFT) and N=15 (RIGHT) for samples with $t_{\mathrm{Co}} = 1.5$ nm (average $D = 7.5$ nm).

The frequency-dependent susceptibility measured near the blocking temperature has also been employed as a tool to ascertain the existence of spin-glass behavior in systems of nanoparticles. In a spin-glass, the average or typical relaxation time must diverge at a finite temperature T_{g}:

$$\tau = \tau_{\mathrm{m}} |1 - T/T_{\mathrm{g}}|^{-z\nu} \tag{5.6}$$

where τ_{m} is the microscopic relaxation time, i.e. the relaxation time of the individual spins in the absence of interactions, and $z\nu$ is a critical exponent. For magnetic nanoparticles, τ_{m} would be given by the Arrhenius' law and it therefore depends on the particle's size and anisotropy.

Experimentally, the critical slowing down is usually characterized by the observation of a weak (weaker than what it is expected for superparamagnets) variation of the susceptibility cusps with frequency [Djurberg 1997]. The "blocking" temperature can then be fitted using Eq. 5.6. Figure 5.22 illustrates these ideas with experimental results obtained for a series of samples with $t_{\mathrm{Co}} = 0.7$ nm and varying N. On the left, the data are fitted with the typical Arrhenius' law whereas,

on the right, we introduce a finite transition temperature leading to a critical slowing down. The Arrhenius fits give rise to very short τ_0 in the range between 4×10^{-18} s and 4×10^{-17} s. These unphysical values are usually considered as an indication of the strong influence of interactions that requires introducing a spin-glass transition into the analysis. The spin-glass "transition temperature" has been determined for the $N = 1$ to get a linear dependence of $\tau \equiv 1/\omega$ on the reduced temperature $\epsilon \equiv (T/T_g - 1)$. For the other samples, and in order to reduce the number of free parameters, we have just rescaled T_g by the ratio between the blocking temperatures measured at 1 Hz. It is clear that the data are compatible with the existence of a finite T_g. We obtain values for the parameters $z\nu$ and τ_m that are the same, within experimental uncertainties, in the case of 2D arrays as well as in the limit of large N. In addition, these values are very close to those found for other systems of magnetic nanoparticles [Djurberg 1997]. The slight saturation effect observed at low frequencies (small reduced temperatures) has also been reported in the literature of magnetic nanoparticles and even in the case of canonical spin-glasses [Mydosh 1993] (although, in this case, it is observed for smaller values of ϵ).

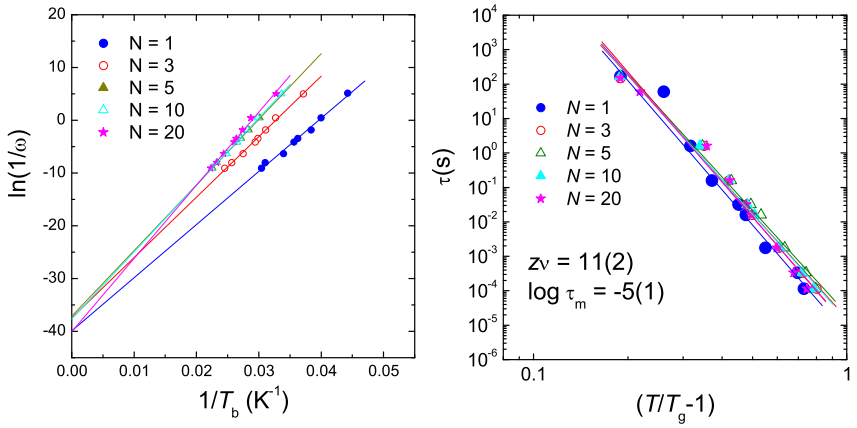

Fig. 5.22. LEFT: τ vs $1/T$ data obtained from ac frequency-dependent susceptibility measurements χ'' vs T. The data are fitted with a typical Arrhenius' law. RIGHT: Critical slowing down scaling of the relaxation time when a finite transition temperature T_g is introduced. Fits are done with Eq. 5.6. Results were performed for a series of samples with $t_{Co} = 0.7$ nm and varying N.

The frequency dependence of the susceptibility cusp is not the only experimental indication of the existence of a critical slowing down. Theoretical models of spin-glasses predict that the complex susceptibility should show a scaling behavior above T_g according to the following expression [Jonsson 2004]:

$$\frac{\chi''(T,\omega)}{\chi_{eq}} = \epsilon^{\beta}(\omega\tau_c) \tag{5.7}$$

where $\omega = 1/t$ and τ_c is the microscopic timescale given by an Arrhenius law. We have performed a scaling analysis of the data for the same series of samples with $t_{Co} = 0.7$ nm and varying N, using the parameters just obtained. The best scaling results are shown in Fig. 5.23 although similar results are obtained varying β between 0.6 and 1.2. Despite the poorer signal-to-noise ratio, the susceptibility of the single 2D layer supports the same scaling function, and with identical parameters, as the multilayers.

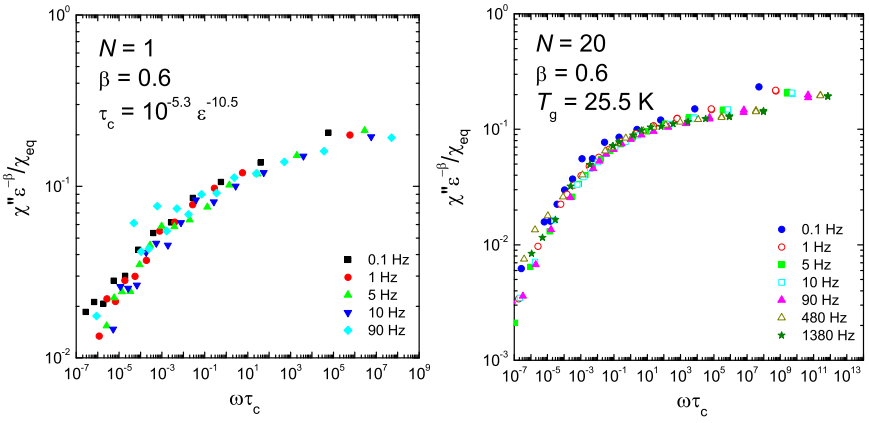

Fig. 5.23. Scaling of $\chi''(\omega)\epsilon^{-\beta}/\chi_{eq}$ data for $T > T_g$ for samples with $t_{Co} = 0.7$ nm and $N = 1$ (LEFT) and $N = 20$ (RIGHT).

Before concluding this section, we would like to briefly mention further experimental results that suggest that aging and other dynamical effects observed in systems of nanoparticles do not need to be associated with the existence of a true phase transition. We have observed aging phenomena for nanoparticles having very different sizes, from

$D \simeq 1.3$ nm up to $D \simeq 7.5$ nm. As we have argued in section 2, we expect that the relative strength of interactions with respect to the magnetic anisotropy change dramatically between these two limits. In terms of the parameter h_{d}, defined in Eq. 5.1, we estimate a variation from $h_{\mathrm{d}} \simeq 0.1$ to a value larger than 1, i.e. from a situation where interactions are expected to represent a small perturbation to another where they are dominant. And finally, we consider the temperature dependence of aging phenomena. We have observed aging at temperatures above the T_{g} obtained from the analysis of the ac susceptibility. In addition, the maximum of $\Delta\chi/\chi$ is observed at temperatures determined by the same Arrhenius law that holds above T_{g}. These two facts question again the existence of a transition to a different phase with radically different magnetic dynamics.

5.5 Conclusions

- Dipolar interactions lead to magnetic memory phenomena like "aging" that can be studied by ZFC magnetization protocols.
- Increasing the average particle size, the strength of interactions tends to be comparable to the magnetic anisotropy.
- In the accessible time window, the amplitude ΔM of the magnetization "hole" burnt by waiting time protocols increases approximately logarithmicaly with the waiting time, as is expected for an spin array that is approaching its equilibrium configuration.
- ΔM shows a dependence with the waiting temperature. The maximum of the ΔM takes place approximately at the blocking temperature for an experimental time equal to the experimental waiting time (t_{w}). A non-zero ΔM is observed even above the blocking temperature defined by the cusp of χ_{ZFC}.
- With respect to the size diameter dependence, the analysis of waiting time experiments suggests that increasing significantly the strength of interparticle interactions with respect to the single-particle anisotropy does not significantly enhance the magnetic correlations. Collective magnetic behavior is observed even in the limit of very small dipolar interactions. $\Delta M/M$ rapidly drops as H increases, i.e. the magnetic correlations are suppressed when an external field applied to the sample is stronger than the typical dipolar fields.

- The maximum of $\Delta M/M$ is approximately proportional to the number of nearest neighbors. The correlations are, therefore, mainly established with the shell of nearest neighbors.
- We observe qualitatively, and in some cases even quantitatively, the same spin dynamics (aging, critical slowing down and critical scaling) in 2D single layers as well as in multilayers.
- These results clearly question the existence of a true spin-glass phase in arrays of interacting nanoparticles.

6

General conclusions

Different nanostructured magnetic materials were studied in order to evaluate how magnetic properties change with size and to determine if quantum phenomena (like the tunnelling effect) take place. The work is also complemented by a study of the influence that interparticle interactions have on these properties. The main conclusions for the materials studied in the present thesis follow:

Mn_{12}: A nonlinear susceptibility study

It is well known that the magnetization is a nonlinear function of the magnetic field and different nonlinear components as χ_2 or χ_3 can be extracted. Though this analysis of the nonlinear response has been often done in spin-glasses, for example, this quantity has been disregarded in studies of molecular magnetic clusters. As the susceptibility is an odd function of the magnetic field, in the absence of bias field one has a null χ_2, whereas in the presence of a magnetic field, χ_2 is the leading nonlinear term.

In a conventional magnetic system, a spin reverses overcoming "classically" the energy barrier imposed by the anisotropy. A rare exception to the thermally activated spin reversal is the case of the Mn_{12} molecules, where the spin reverses via tunnelling through quasi-degenerated excited levels.

The equilibrium response (for temperatures above the blocking temperature) shows a large sensitivity to temperature-induced changes in the magnetic anisotropy, even for powdered samples with axes distributed at random. This information is absent from the linear response.

The frequency-dependent or dynamical response is found to present a genuinely *quantum* contribution due to the detuning of the energy

levels by a *longitudinal* field. The χ_2 and χ_3 vs. H_z curves neatly amplify the resonant tunnel, as this entails large $\mathrm{d}\tau/\mathrm{d}H_z$ and $\mathrm{d}^2\tau/\mathrm{d}H_z^2$ respectively. As a consequence, nonlinear susceptibility is revealed as a powerful tool to elucidate the presence of quantum tunnelling. An angular analysis reveals that a decoherence time inherent to its quantum nature, that is τ_Φ, shorter than the lifetime of the spin levels, τ_0, due to energy dissipation, is the responsible for a fast loss of coherent dynamics such as precession or tunnel oscillations. Finally, the study reveals a weaker quantum nonlinearity phenomenon on a crystal of "fast relaxing" Mn_{12} clusters, the Mn_{12} benzoate, compared with the reference Mn_{12} acetate. This species shows a magnetic behavior closer to the classically expected one, probably as a result of a stronger decoherence combined with the lower magnetic anisotropy barrier.

Cobalt nanoparticles

1) Nonlinearity study

Form the equilibrium response of the nonlinear component of the susceptibility, we can estimate the magnetic anisotropy in an independent way, without using the relaxation time, sometimes hindered as a consequence of the size distribution. Our data confirm that particles capped by a noble metal layer undergo a significative enhancement in the anisotropy due to the modification of the special conditions of the surface atoms.

The "quantum nonlinearity" is absent in dynamical measurements and measurements reveal a typically "classical" behavior. In cobalt particles, the behavior is in agreement with an "overdamped" regime. In other words, the magnetic energy relaxation takes place in a time shorter than the period of a Larmor precession around the anisotropy axis. The time associated with the energy dissipation is, therefore, $\tau_0 < 10^{-12}$ s.

2) Interactions on Cobalt particles

As was mentioned in the introduction, in a collection of structures also interactions play an important role. A hint for the influence that dipolar interactions have on the magnetic relaxation of cobalt particles was provided already by the nonlinear susceptibility data. These data reveal that metal capping of the cobalt nanoparticles does not change the energetic dissipation degree of these magnetic moments. In fact,

already for Cobalt particles in alumina, the response is characteristic of the overdamped regime. A possible source of the additional "damping" might be the dipolar interactions, which enable a way of exchanging magnetic energy between neighboring particles.

We have studied the existence of magnetic collective phenomena by measuring memory effects like "aging" in the magnetic susceptibility. These effects are usually considered to be a signature of spin-glass-like behavior, and of the presence of correlations between the magnetization flips of neighbor particles. The main conclusion, in this respect, is the experimental evidence of "aging" phenomena in the case of a 2D layer. As it is known that in a 2D system it is not expected to show a spin-glass phase at any finite temperature, we can conclude that "aging" phenomena are not peculiar of systems that show a spin-glass phase. By piling up layers, the effect tends to a saturation as the extension of magnetic correlations is restricted to a first neighbors coordination sphere. This experimental fact also questions the existence of a "true" spin-glass phase. Also, by modifying the size of the particles, we found that "aging" is present even for very small particles, for which interactions are expected to represent a small perturbation with respect to the magnetic anisotropy. In the presence of an external magnetic field, the correlations are rapidly suppressed.

Nickel nanowires

Let us grow directionally a magnetic particle using a bottom-up strategy consisting of a template-assisted method that enables us a good control over the particles aspect ratio. Porous alumina membranes have been used extensively as a template to grow nanowires. We have filled the templates with an element possessing a weak crystalline anisotropy, such as nickel, in order to minimize the effect over the characteristic shape anisotropy.

Oppositely to molecules or particles, the magnetic response of nanowires does not show any evidence of a superparamagnetic behavior, which confers to the material a potential interest for application in data storage devices. Despite their weak crystalline anisotropy, the magnetic response shows evidences of a particle-to-wire crossover above a certain aspect ratio. In the "wire-like" limit, room temperature coercive field values lower than the predicted in the Stoner-Wohlfarth "in unison" model are observed, which are in agreement with a "fanning" mode, usually neglected in the recent literature. For larger diameters, the "curling" reversal mode is in qualitatively agreement with our data.

In a range of temperatures not covered until now, the aluminium expansion produces a compression or a tensile stress (below or above the temperature of synthesis, i.e. room temperature) on the nickel wires, that are the responsible of a coercive field maximum at room temperature. In other words, decreasing the temperature gives rise to a thermally-induced magnetoelastic effect that reduces the coercivity. The effect induces a minimum in coercivity below room temperature that is only shown if aluminium is not removed from the samples. Therefore, the origin of this effect, which has been a bit controversial in recent years [Kumar 2006][Vazquez 2005][Zeng 2002], can be attributed to the presence of the aluminium layer. Also, mechanical stresses are influenced by the aspect ratio of the samples, which opens the possibility to modulate the mentioned behavior. Above room temperature, the Curie temperature T_C progressively decreases due to a finite-size effect as the wire's diameter decreases. The T_C extrapolated to infinite diameter shows an additional decrease of about 3 K with respect the bulk value. This suggests that stresses, whose presence is evidenced in the hysteresis experiments, also modify T_C.

Despite the optimistic title, the present document is far from a panoramic thesis. The author hopes that the different particular and monographic chapters will provide a good starting point to have a general idea and to constitute a challenge to elucidate the new and characteristic behavior of very small materials. To justify the title I cite Umberto Eco[1]: "It could be a trick, but it is not a cheap one as it costs a lot of work". This book will be, not only an instrument to find some answers, but a tool to continue opening questions. This thesis was realized during four years of intensive experimental work in order to be another little link in the long chain of the knowledge.

[1] *Come si fa una tesi di laurea*, Umberto Eco (1972)

References

[Agarwal 2006] R. Agarwal and C. M. Lieber. *Appl. Phys. A: Mater.Sci. Proc.* **85** 2009 (2006).

[Aharoni 1998] A. Aharoni. *IEEE Trans. Magnetics* **34** 2175 (1998).

[Aharoni 2000] A. Aharoni. *Introduction to the theory of ferromagnetism* (Oxford unicersity Press, Oxford, 2000).

[Ardavan 2007] A. A. Ardavan, O. Rival, J. J. L. Morton, S. J. Blundell, A. M. Tyryshkin, G. A. Timco and R. E. P. Winpenny. *Phys. Rev. Lett.* **98**, 057201 (2007).

[Babonneau 2000] D. Babonneau, F. Petroff, J. L. Maurice, F. Fettar, A. Vaurès and A. Naudon. *Appl. Phys. Lett.* **76**, 2892 (2000).

[Barbara 1999] B. Barbara, L. Thomas, F. Lionti, I. Chiorescu and A. Sulpice. *J. Phys.: Condens. Matter* **16**, R771 (2004).

[Barbara 2007] B. Barbara. *Phys. Rev. Lett.* **99**, 177201 (2007).

[Barra 1997] A.-L. Barra, D. Gatteschi and R. Sessoli. *Phys. Rev. B* **56**, 8192 (1997).

[Bartolomé 2004] F. Bartolomé, F. Luis, F. Petroff, L. M. García, J. Bartolomé, V. Cros and H. Haffrès. *J. Magn. Magn. Mater.* **272-276**, E1275 (2004).

[Bartolomé 2006] J. Bartolomé, F. Bartolomé, L. M. García, F. Luis, F. Petroff, V. Cros, H. Haffrès and A. Vaurés. *Smart Materials for Ranging Systems (NATO Science Series, Series II)* **226**, 1 (2006).

[Bartolomé 2007] J. Bartolomé, L. M. García, F. Bartolomé, F. Luis, R. López-Ruiz, F. Petroff, C. Deranlot, F. Wilhelm, A. Rogalev, P. Bencok, N. B. Brookes, L. Ruiz and J. M. González-Calbet. *Phys. Rev. B* **77**, 184420 (2008)

[Bartolomé 2008] J. Bartolomé, F. Luis, L. M. García, F. Bartolomé, F. Petroff, C. Deranlot, F. Wilhelm, A. Rogalev, P. Bencok and N. B. Brookes. *Materials Science Forum* **570**, 1 (2008).

[Batlle 2002] X. Batlle and A. Labarta. *J. Phys. D: Condens. Matter.* **35**, R15 (2002).

[Bitoh 1993] T. Bitoh, K. Ohba, M. Takamatsu, T. Shirane and S. Chikazawa. *J. Phys. Soc. Jpn.* **62**, 2583 (1993).

[Blundell 2004] S. J. Blundell and F. L. Pratt. *J. Phys.: Condens. Matter* **16**, R771 (2004).

[Bodker 2002] F. Bodker, S. Morup and S. Linderoth. *Phys. Rev. Lett.* **72**, 284 (1994).

[Briatico 1999] J. Briático, J. L. Maurice, J. Carrey, D. Imhoff, F. Petroff and A. Vaurès. *Eur. Phys. J. D* **9**, 517 (1999).
[Brown 1963] W. F. Brown Jr. *Phys. Rev.* **130**, 1677 (1963).
[Capasso 1990] F. Capasso and S. Datta. *Phys. Today* **2** 74 (1990).
[Carlin 1986] R. L. Carlin. *Magnetochemistry* (Springer, Berlin, 1986).
[Cavallini 2003] M. Cavallini, F. Biscarini, J. Gómez, D. Ruiz-Molina and J. Veciana. *Nano Lett.* **11**, 1527 (2003).
[Cavallini 2005] M. Cavallini, J. Gómez-Segura, D. Ruiz-Molina, M. Massi, c. Albonetti, C. Rovira, J. Veciana and F. Biscarini. *Angew. Chem., Int. Ed.* **44**, 888 (2005).
[Chaboussant 2004] G. Chaboussant, A. Sieber, S. Ochsenbein, H. U. Güdel, M. Murrie, A Honecker, N. Fukushima and B. Normand. *Phys. Rev. B* **70**, 104422 (2004).
[Chen 1995] J. P. Chen, C. M. Sorensen, K. J. Klabunde and G. C. Hadjipanayis. *Phys. Rev. B* **51**, 527 (1995).
[Chen 2005] X. Chen, S. Bendata, O. Petracic, W. Kleeman, S. Sahoo, S. Cardoso and P. P. Freitas. *Phys. Rev. B* **72**, 214436 (2005).
[Choi 2003] J. Choi, K. Nielsch, M. reiche, R. B. Wehrspohn and U. Gosele. *J. Vac. Sci. and Tech.* **21** 763 (2003).
[Clemente-León 2003] M. Clemente-León, E. Coronado, A. Forment-Aliaga, P. Amorós, J. Ramírez-Castellanos and J. M. González-Calbet. *J. Mater. Chem.* **13**, 3089 (2003).
[Cornia 2003] A. Cornia, R. Sessoli, L. Sorace, D. Gatteschi, A. L. Barra and C. Daiguebonne. *Angew. Chem. Int. Ed. Engl.* **42**, 1645 (2003).
[Christou 2000] G. Christou, D. Gatteschi, D. N. Hendrickson and R. Sessoli. *MRS Bull.* **25**, 26 (2000).
[Chudnovsky 2004] E. M. Chudnovsky. *Phys. Rev. Lett.* **92**, 120405 (2004).
[Chudnovsky 2006] E. M. Chudnovsky and J. Tejada. *Lectures on Magnetism* (Rinton Press, Princeton, 2006).
[Czokan 1980] P. Czokan. *Corrosion Science and Technology* **7** 239 (1980).
[Despic 1983] A. Despic and V. P. Parkhutic. *Modern Aspects of Electrochemistry* **7** Ch7b (1983).
[Djurberg 1997] C. Djurberg, P. Svedlindh, P. Nordblad, M. F. Hansen, F. Bodker and S. Morup. *Phys. Rev. Lett.* **79**, 5154 (1997).
[Domingo 2004] N. Domingo, B. E. Williamson, J. Gómez-Segura, Ph. Gerbier, D. Ruiz-Molina, D. B. Amabilino, J. Veciana and J. Tejada. *Phys. Rev. B* **69**, 052405 (2004).
[Dormann 1988] J. L. Dormann, L. Bessais and D. Fiorani. *J. Phys. C* **21**, 2015 (1988).
[Dormann 1996] J. L. Dormann, F. D'Orazio, F. Lucari, E. Tronc, P. Prené, J. Jolivet, D. Fiorani, R. Cherkaoui and M. Nogues. *Phys. Rev. B* **53**, 14291 (1996).
[Dormann 1999] J. L. Dormann, D. Fiorani, R. Cherkaoui, E. Tronc, F. Lucari, F. D'Orazio, L. Spinu, M. Noguès, H. Kachkachi and J. P. Jolivet. *J. Mag. Mag. Mater.* **203**, 23 (1999).
[D.P.Landau 1976] D. P. Landau. *Phys. Rev. B* **14** 255 (1976).
[Dube 2001] M. Dube and P. C. E. Stamp. *Chem. Phys.* **268**, 257 (2001).
[Ebihara 1982] K. Ebihara, H. takahashi and M. Nagayama. *J. Met. Finish. Soc. Jap* **33** 4 (1982).
[Ebihara 1983] K. Ebihara, H. takahashi and M. Nagayama. *J. Met. Finish. Soc. Jap* **34** 548 (1983).

[El Hallak 2007] F. El Hallak, J. van Slageren, J. Gómez-Segura, D. Ruiz-Molina and M. Dressel. *Phys. Rev. B* **75**, 104403 (2007).

[Evangelisti 2006] M. Evangelisti, F. Luis, L. J. de Jongh and M. Affronte. *J. Matter. Chem.* **16**, 2534 (2006).

[Fayet 1986] P. Fayet, F. Granzer, G. Hegenbart, E. Moisar, B. Pischel and L. Woste. *Z. Phys. D* **3**, 299 (1986).

[Fernandez 1998] J. F. Fernández, F. Luis and J. Bartolomé. *J. Appl. Phys.* **83**, 6940 (1998).

[Fernández 2008] J. F. Fernández. *Phys. Rev. B* (2008), in press.

[Fort 1998] A. Fort, A. Rettori, J. Villain, D. Gatteschi and R. Sessoli. *Phys. Rev. Lett.* **80**, 612 (1998).

[Frei 1957] E. H. Frei, S. Shtrikman and D. Treves. *Phys. Rev.* **106** 446 (1957).

[Friedman 1996] J. R. Friedman, M. P. Sarachik, J. Tejada and R. Ziolo. *Phys. Rev. Lett.* **76**, 3830 (1996).

[Friedman 1998] J. R. Friedman, M. P. Sarachik and R. Ziolo. *Phys. Rev. B* **58**, R14729 (1998).

[Friedman 2007] A. L. Friedman and L. Menon. *J. Electrochem. Soc.* **154** E68 (2007).

[Furneaux 1989] R. C. Furneaux, W. R. Rigby and A. P. Davidson. *Nature* **337** 147 (1989).

[Garanin 1997] D. A. Garanin and E. M. Chudnovsky. *Phys. Rev. B* **56**, 11102 (1997).

[Garanin 1999] D. A. Garanin, E. C. Kennedy, D. S. F. Crothers and W. T. Coffey. *Phys. Rev. E* **60**, 6499 (1999).

[Garcia-Palacios 2000a] J. L. García-Palacios, P. Jonsson and P. Svedlindh. *Phys. Rev. B* **61**, 6726 (2000).

[Garcia-Palacios 2000b] J. L. García-Palacios and P. Svedlindh. *Phys. Rev. Lett.* **85**, 3724 (2000).

[Garcia-Palacios 2000c] J. L. García-Palacios. *Adv. Chem. Phys.* **112**, 1 (2000).

[Garcia-Palacios 2004] J. L. Garcia-Palacios and D. A. Garanin. *Phys. Rev. B* **70**, 064415 (2004).

[Gatteschi 2003] D. Gatteschi and R. Sessoli. *Angew. Chem. Int. Ed.* **42**, 268 (2003).

[Gatteschi 2006] D. Gatteschi, R. Sessoli and J. Villain. *Molecular Nanomagnets* (Oxford University Press, Oxford, 2006).

[Hansen 2002] M. F. Hansen, P. E. Jönsson, P. Nordblad and P. Svedlindh. *J. Phys.:Condens. Matter.* **14**, 4901 (2002).

[Harris 1973] R. Harris, M. Plischke and M. J. Zuckermann. *Phys. Rev. Lett.* **31**, 160 (1973).

[He 2003] H. He and N. J. Nongjian. *Encyclopedia of Nanoscience and nanotechnology* **X** 1-18 (2003).

[Hernandez 1996] J. M. Hernández, X. X. Zhang, F. Luis, J. Bartolomé, J. Tejada and R. Ziolo. *Europhys. Lett.* **35**, 301 (1996).

[Huysmans 1988] G. T. A. Huysmans and J. C. Lodder. *J. Appl. Phys.* **64** 2016 (1988).

[Jacobs 1955] I. S. Jacobs and C. P. Bean. *Phys. Rev.* **100** 1060 (1955).

[James 1977] T. H. James. *The theory of the photographic process* (1977).

[Jessensky 1998] O. Jessensky, F. Muller and U. Gosele. *Appl. Phys. Lett.* **72** 1173 (1998).

[Jones 1982] P. S. Jones and B. J. Macfadden. *J. Exp. Biol.* **19**, 1 (1982).

[Jonsson 1995] T. Jonsson, J. Mattson, C. Djurberg, F. A. Khan, P Nordblad and P. Svedlindh. *Phys.Rev. Lett.* **75**, 4138 (1995).
[Jonsson 1998a] T. Jonsson, P. Svedlindh and M. F. Hansen. *Phys. Rev. Lett.* **80**, 177 (1998).
[Jonsson 1998b] T. Jonsson, P. Svedlindh and M. F. Hansen. *Phys.Rev. Lett.* **81**, 3976 (1998).
[Jonsson 2000] P. Jonsson, T. Jonsson, J. L. García-Palacios and P. Svedlindh. *J. Magn. Magn. Mater.* **222**, 219 (2000).
[Jonsson 2001a] P. E. Jonsson and J. L. García-Palacios. *Europhys. Lett.* **55** 418 (2001).
[Jonsson 2001b] P. E. Jonsson and J. L. García-Palacios. *Phys. Rev. B* **64** 174416 (2001).
[Jonsson 2004] P. E. Jonsson. *Adv. Chem. Phys.* **128** 191 (2004).
[Jonsson 2005] P. E. Jonsson, H. Yoshino, H. Mamiya and H. Takayama. *Phys. Rev. B* **71**, 104404 (2005).
[Jonsson 2007] P. E. Jonsson, R. Mathieu, W. Wernsdorfer, A. M. Tkachuk and B. Barbara. *Phys. Rev. Lett.* **98**, 256403 (2007).
[Kahn 1993] O. Kahn. *Molecular Magnetism* (Wiley-VCH, Weinheim, 1993).
[Keller 1952] F. Keller, M. S. Hunter and D. L. Robinson. *J. Electrochem. Soc.* **100** 411 (1952).
[Kitakami 1997] O. Kitakami, H. Sato and Y. Shimada. *Phys. Rev. B* **56**, 849 (1997).
[Kittel 1949] C. Kittel *Rev. Mod. Phys.* **21**, 541 (1949).
[Kumar 2006] A. Kumar, S. Fahler, H. Schlorb, K. Leistner and L. Schultz. *Phys. Rev. B* **73** 064421 (2006).
[Lee 2006] W. Lee, R. Ji, U. Gosele and K. Nielsch. *Nature Materials* **5** 741 (2006).
[Leggett 2002] A. J. Leggett. *J. Phys.: Condens. Matter* **14**, R415 (2002).
[Leuenberger 1999] M. N. Leuenberger and D. Loss. *Europhys. Lett.* **46**, 692 (1999).
[Leuenberger 2001] M. Leuenberger and D. Loss. *Nature* **410**, 789 (2001).
[Lewis 1993] L. N. Lewis. *Chem. Rev.* **93**, 2693 (1993).
[Li 1998] A. P. Li, F. Muller, A. Birner, K. Nielsch and U. Gosele. *J. Appl. Phys.* **84** 6023 (1998).
[Lis 1980] T. Lis. *Acta Crystallogr. Sect. B* **36**, 2042 (1980).
[Lopez-Ruiz 2005] R. López-Ruiz, F. Luis, V. Gonzalez, A. Millán and J. L. García-Palacios. *Phys. Rev. B* **72** 224433 (2005).
[Lopez-Ruiz 2007] R. López-Ruiz, F. Luis, A. Millán, C. Rillo, D. Zueco and J. L. García-Palacios. *Phys. Rev. B* **75** 012402 (2007).
[Luis 1998] F. Luis, J. Bartolomé and J. F. Fernandez. *Phys. Rev. B* **57**, 505 (1998).
[Luis 2002a] F. Luis, F. Mettes and L. J. de Jongh, *Magnetism: Molecules to Materials*, edited by J. S. Miller and M. Drillon (Wiley-VCH, Weinheim, 2002), Vol. III, pp. 169–210.
[Luis 2002b] F. Luis, J. M. Torres, L. M. García, J. Bartolomé, J. Stankiewicz, F. Petroff, F. Fettar, J. L. Maurice and A. Vaurés *Phys. Rev. B* **65**, 094409 (2002).
[Luis 2002c] F. Luis, F. Petroff, J. M. Torres, L. M. García, J. Bartolomé, J. Carrey and A. Vaurès. *Phys. Rev. Lett.* **88**, 217205 (2002).
Comment by M. F. Hansen and S. Mørup *Phys. Rev. Lett* **90** 059705 (2003).
Reply by F. Luis et al. *Phys. Rev. Lett* **90** 059706 (2003).
[Luis 2003] F. Luis, J. Bartolomé, F. Petroff, L. M. García, A. Vaurès and J. Carrey. *J. Appl. Phys.* **93** 7032 (2003).
[Luis 2004] F. Luis, V. Gonzalez, A. Millán and J. L. García-Palacios. *Phys. Rev. Lett.* **92** 107201 (2004).

[Luis 2005] F. Luis, J. Campo, J. Gómez, G. J. McIntyre, J. Luzón and D. Ruiz-Molina. *Phys. Rev. Lett.* **95** 227202 (2005).

[Luis 2006] F. Luis, F. Bartolomé, F. Petroff, J. Bartolomé, L. M. García, C. Deranlot, H. Jaffres, M. J. Martinez, P. Bencock, F. Wilhelm, A. Rogalev and N. B. Brookes. *Europhys. Lett.* **76** 142 (2006).

[Luo 1991] W. Luo, S. R. Nagel, T. F. Rosenbaum and R. E. Rosensweig. *Phys.Rev. Lett.* **67** 2721 (1991).

[MacDonald 1989] D. D. MacDonald *J. Electrochem. Soc* **140** L27 (1993).

[Mamiya 1998] H. Mamiya, I. Nakatani and T. Furubayashi. *Phys.Rev. Lett.* **80** 177 (1998).

[Mamiya 1999] H. Mamiya, I. Nakatani and T. Furubayashi. *Phys.Rev. Lett.* **82** 4332 (1999).

[Mamiya 2002] H. Mamiya, I. Nakatani and T. Furubayashi. *Phys. Rev. Lett.* **88** 067202 (2002).

[Martínez 2007] R. V. Martínez, F. García, R. García, E. Coronado, A. Forment-Aliaga, F. M. Romero and S. Tatay. *Adv. Mater.* **19**, 291 (2007).

[Masuda 1995] H. Masuda and K. Fukuda *Science* **268** 1466 (1995).

[Masuda 1997] H. Masuda, F. Hasegwa and S. Ono. *J. Electrochem. Soc.* **L127** 144 (1997).

[Masuda 1998] H. Masuda, K. Yada and A. Osaka. *Jpn. J. Appl. Phys.* **37** L1340 (1998).

[Mathieu 2001a] R. Mathieu, P. E. Jönsson, P. Nordblad, H. Aruga Katori and A. Ito. *Phys. Rev. B* **65**, 012411 (2001).

[Mathieu 2001b] R. Mathieu, P. Jönsson, D. N. H. Nam and P. Nordblad. *Phys. Rev. B* **63**, 092401 (2001).

[Mattsson 1993] J. Mattsson, C. Djuberg, P. Norblad, L. Hoines, R. Stubi and J. A. Cowen. *Phys. Rev. B* **47**, 14626 (1993).

[Maurice 1999] J. L. Maurice, J. Briático, J. Carrey, F. Petroff, L. F. Schelp and A. Vaurès. *Philos. Mag. A* **79**, 2921 (1999).

[Miller 2002] J. S. Miller and M. Drillon. *Magnetism: Molecules to Materials, vol. III*(2002).

[Morup 1994] S. Morup and E. Tronc. *Phys. Rev. Lett.* **72**, 3278 (1994).

[Morup 1995] S. Morup, F. Bodker, P. V. Hendriksen and S. Linderoth. *Phys. Rev. B* **52**, 287 (1995).

[Morrish 1965] A. H. Morrish. *The physical principles of magnetism* (John Wiley and Sons, New York, 1965).

[Mydosh 1993] J. A. Mydosh. *Spin glasses : an experimental introduction* (Taylor and Francis, London, 1993).

[Neel 1949] L. Neel. *Ann. Geophys.* **5**, 99 (1949).

[Nielsch 2000] K. Nielsch, F. Muller, A. P. Li and U. Gosele. *Adv. Mater.* **12** 582z (1989).

[Nielsch 2002] K. Nielsch, J. Choi, K. Schwirn, R. B. Wehrspohn and U. Gösele. *Nano Lett.* **2** 677 (2002).

[Ono 2004] S. Ono, M. Saito, M. Ishiguro and H. Asoh. *J. Electrochem. Soc.* **151** B473 (2004).

[O'sullivan 1970] J. P. O'sullivan and G. C. Wood. *Proc. Roy. Soc. London* **A316** 511 (1970).

[Pankhurst 1993] Q. A. Pankhurst and R. J. Pollard. *J. Phys. D: Condens. Matter* **5**, 8487 (1993).

[Parkhutik 1992] V. P. Parkhutik and V. I. Shershulsky. *J. Phys D: Appl. Phys.* **25** 1258 (1992).

[Patolsky 2006a] F. Patolsky, B. P. Timko, G. Yu, Y. Fang, A. B. Greytak, G. Zheng and C. M. Lieber. *Science* **313**, 1100 (2006).

[Patolsky 2006b] V. Patolsky, G. Zheng and C. M. Lieber. *Nature Protocols* **1** 1711 (2006).

[Patrick 1954] L. Patrick. *Phys. Rev.* **93** 384 (1954).

[Paulus 1999] P. M. Paulus, F. Luis, M. Kroll, G. Schmid and L. J. de Jongh. *J. Magn. Magn. Mater.* **224** 180 (2001).

[Pavlovic 1986] T. Pavlovic and A. Ignatiev. *Thin Solid Films* **138** 97 (1986).

[Petracic 2006] O. Petracic, X. Chen, S. Bendata, W. Kleeman, S. Sahoo, S. Cardoso and P. P. Freitas. *J. Magn. Magn. Mater.* **300**, 192 (2006).

[Respaud 1998] M. Respaud, J. M. Broto, H. rakoto, A. R. Fert, L. Thomas, B. Barbara, M. Verelst, E. Snoeck, P. Lecante, A. Mosset, J. Osuna, T. Ould Ely, C. Amiens and B. Chaudret. *Phys. Rev. B* **57**, 2925 (1998).

[Ruiz-Molina 2003] D. Ruiz-Molina, M. Más-Torrent, J. Gómez, A. Balana, N. Domingo, J. Tejada, M. T. Martínez, C. Rovira and J. Veciana. *Adv. Mater.* **15**, 42 (2003).

[Sahoo 2002] S. Sahoo, O. Petracic, Ch. Binek, W. Kleemann, J. B. Sousa, S. Cardoso and P. P. Freitas. *J. Phys.: Condens. Matter.* **14**, 6729 (2002).

[Sahoo 2003] S. Sahoo, O. Petracic, W. Kleemann, P. Nordblad, S. Cardoso and P. P. Freitas. *Phys. Rev. B* **67**, 214422 (2003).

[Samwel 1992] E. O. Samwel, P. R. Bissell and J. C. Lodder. *J. Magn. Magn. Mater.* **115** 327 (1992).

[Sasaki 2005] M. Sasaki, P. E. Jönsson, H. Takayama and H. Mamiya. *Phys. Rev. B* **71**, 104405 (2005).

[Sessoli 1993] R. Sessoli, D. Gatteschi, A. Caneschi and M. A. Novak. *Nature* **365**, 141 (1993).

[Sessoli 1998] R. Sessoli, D. Rovai, C. Sangregorio, T. Ohm, C. Paulsen and A. Caneschi. *J. Magn. Magn. Mater.* **1330**, 177 (1998).

[Schiffer 1995] P. Schiffer, A. P. Ramirez, D. A. Huse, P. L. Gammel, U. Yaron, D. J. Bishop and A. J. Valentino. *Phys. Rev. Lett.* **74**, 2379 (1995).

[Shi 1996] J. Shi, S. Gider, K. babcock and D. D. Awschalom. *Science* **271** 937 (1996).

[Skomski 2002] R. Skomski, H. Zeng and D. J. Sellmyer. *J. Magn. Magn. Mater.* **249** 175 (2002).

[Smoluchowski 1954] R. Smoluchowski. *Phys. Rev.* **93** 392 (1954).

[Stamp 1996] P. C. E. Stamp and G. Tatara. *Quantum Coherence and Decoherence (ISQM-Tokyo 95)* **77**, 3017 (1996).

[Stanley 1971] H. E. Stanley. *Introduction to phase transitions and critical phenomena* (Oxford University Press, Oxford, 1971).

[Sun 1999] Z. Sun, D. Ruiz, N. R. Dilley, M. Soler, J. Ribas, K. Folting, B. Maple, G. Christou and D. N. Hendrickson. *Chem. Commun.* **19**, 1973 (1999).

[Sun 2000] L. Sun, P. C. Searson and C. L. Chien. *Phys. Rev. B* **61** R6463 (2000).

[Takeda 2002] K. Takeda, K. Awaga, T. Inabe, A. Yamaguchi, H. Ishimoto, T. Tomita, H. Mitamura, T. Goto, N. Môri and H. Nojiri. *Phys. Rev. B* **65**, 094424 (2002).

[Tasiopoulos 2004] A. J. Tasiopoulos, A. Vinslava, W. Wernsdorfer, K. A. Abboud and G. Christou. *Angew. Chem.* **43**, 2117 (2004).

[Tejada 2001] J. Tejada, E. Chudnovsky, E. del Barco, J. M. Hernández and T. Spiller. *Nanotechnology* **12**, 181 (2001).

[Torres 2002] J. M. Torres, F. Luis, L. M. García, J. Bartolomé, J. Stankiewicz, F. Petroff, F. Fettar and A. Vaurés. *J. Magn. Magn. Mater.* **242**, 575 (2002).

[Thomas 1996] L. Thomas, F. Lionti, R. Ballou, D. Gatteschi, R. Sessoli and B. Barbara. *Nature* **383**, 145 (1996).

[Thompson 1978] G. E. Thompson, R. C. Furneaux, G. C. Wood, J. A. Richardson and J. S. Goode. *Nature* **272** 433 (1978).

[Thompson 1983] G. E. Thompson and G. C. Wood. *Teatrise on materials Science and Technology* **23** 205 (1983).

[Tupitsyn 2002] I. Tupitsyn and B. Barbara. *Magnetism: molecules to materials*, edited by J. S. Miller and M. Drillon (Wiley-VCH, Weinheim, 2002), Vol. III, pp. 109–168.

[Vazquez 2005] M. Vazquez, K. Pirota, J. Torrejon, D. Navas and M. Hernandez-Velez. *J. Magn. Magn. Mater.* **14** 715 (2005).

[Weiss 1993] U. Weiss. *Quantum Dissipative Systems* (World Scientific, Singapore, 1993).

[Wernsdorfer 1997] W. Wernsdorfer, E. Bonet-Orozco, K. Hasselbach, A. Benoit, D. Mailly, O. Kubo, H. Nakano and B. Barbara. *Phys. Rev. Lett.* **79**, 4014 (1997).

[Wernsdorfer 1999] W. Wernsdorfer, R. Sessoli and D. Gatteschi. *Europhys. Lett.* **47**, 254 (1999).

[White 2000] R. L. White. *J. Magn. Magn. Mater.* **209** 1 (2000).

[Wu 1993] W. Wu, D. Bitko, T. F. Rosenbaum and G. Aeppli. *Phys. Rev. Lett.* **71**, 1919 (1993).

[Würger 1998] A. Würger. *J. Phys.: Condens. Matter.* **10**, 10075 (1998).

[Zeng 2002] H. Zeng, S. Michalski, R. D. Kirby, D. J. Sellmeyer, L. Menon and S. Bandyopadhyay. *J. Phys: Condens. Mat.* **14** 715 (2002).

[Zobbi 2005] L. Zobbi, M. Mannini, M. Pacchioni, G. Chastanet, D. Bonacchi, C. Zanardi, R. Biagi, U. del Pennino, D. Gatteschi, A. Cornia and R. Sessoli. *Chem. Commun.* **12**, 1640 (2005).

[Zurek 2003] W. H. Zurek. *Rev. Mod. Phys.* **75**, 715 (2003).

Resumen

Objetivos

El tema general de esta tesis es el estudio experimental de distintos materiales magnéticos nanoestructurados. Se trata de estudiar como sus propiedades magnéticas cambian con el tamaño y, en especial, determinar si se observan fenómenos cuánticos, como el efecto túnel, típicos de la escala atómica. Concretamente, la tesis se centró en el estudio magnético de tres tipos de muestras: monocristales de clústeres de Mn_{12}, nanopartículas de Cobalto y nanohilos de Níquel.

Los clústeres de Mn_{12} y de Cobalto son sistemas modelo para la experimentación de fenómenos cuánticos en magnetismo. La susceptibilidad magnética no-lineal es una magnitud sensible a la existencia de dichos fenómenos. Además, es sensible a como los momentos magnéticos interactúan con su entorno, pudiéndose evaluar el nivel de amortiguamiento que el medio externo ejerce sobre éstos. Pese a ello, apenas se había realizado trabajo experimental relacionado con sus propiedades no lineales. Uno de los temas de esta tesis es el estudio de la susceptibilidad magnética no lineal de estos materiales.

En los clústeres de Cobalto, se observó asimismo que las muestras exhiben un comportamiento de memoria magnética similar al de vidrio de espín, posiblemente debido a la acción de interacciones dipolares entre ellos. Nuestro objetivo será estudiar como afectan las interacciones a la relajación magnética y la posible existencia de fase vidrio de espín.

En cuanto al estudio del magnetismo en nanohilos, requirió optimizar los métodos de preparación de este tipo de materiales. La

preparación de nanohilos de Níquel a partir de la electrodeposición de metales ferromagnéticos en matrices porosas de alúmina producidas por anodización controlada de láminas de aluminio será otro de los temas de esta tesis. A parte de su caracterización magnética, se estudirán los mecanismos de relajación magnética y los efectos de tamaño finito a través del cambio de la temperatura de Curie con el diámetro del hilo.

Interés de la investigación

Las nanopartículas magnéticas atraen considerable interés por su posible aplicación en tecnologías de almacenamiento de información de alta densidad y en biomedicina. La mayor parte de estas aplicaciones se basan en dos propiedades, asociadas a su vez con el tamaño nanométrico: la ausencia de dominios magnéticos presentes en imanes macroscópicos (se llaman por eso partículas monodominio) y la anisotropía magnética, que favorece ciertas orientaciones del momento magnético neto estabilizándolas frente a fluctuaciones térmicas. Además de su interés práctico, estos materiales permiten también investigar como evolucionan las propiedades magnéticas (por ejemplo la imanación) entre los límites micro- y macroscópico, así como la posibilidad de que fenómenos cuánticos contrarios a nuestra intuición, como el efecto túnel, pervivan más allá del mundo de los átomos, electrones, etc. La existencia de fenómenos cuánticos en sistemas de tamaño mayor al atómico se ve limitada físicamente por la perturbación que el entorno ejerce sobre el sistema, o decoherencia, que tiende a destruir estos efectos cuánticos y favorecer que el comportamiento se aproxime al clásico.

El Mn_{12} forma parte de las denominadas moléculas-imán. El acetato de Mn_{12} se sintetiza mediante una estrategia "Bottom-Up" siguiendo la reacción descrita por T. Lis en 1980, mientras que el benzoato de Mn_{12} se obtiene a partir de éste por sustitución de ligando en exceso de ácido benzoico. Su importancia radica en que el momento magnético de la molécula con alto espín S=10 se invierte por efecto túnel a través de la barrera de energía de anisotropía. Este descubrimiento es interesante porque constituye un ejemplo de un efecto cuántico que aparece en una escala de tamaño intermedia entre el átomo y el mundo macroscópico clásico. El efecto túnel tiene lugar por estados excitados, al menos para temperaturas por encima de 2 K. A pesar de haber sido objeto de intenso trabajo científico durante más de una decada, quedan todavía

muchas cuestiones relacionadas con la influencia que las interacciones que los fonones (decoherencia) ejercen sobre el mecanismo de relajación cuántica de las moléculas. Es un sistema modelo tanto para el estudio de espines con anisotropía magnética, como para el estudio de dinámica de sistemas mesoscópicos cuánticos sujetos a efectos de interacciones con el medio.

Las nanopartículas de Co se preparan siguiendo una estrategia "Top-Down", por sputtering secuencial de capas de Co y Al_2O_3. El proceso da lugar a una estructura de nanoesferas de Co ordenadas espacialmente. Su tamaño se puede controlar entre 1 y 5 nm de diámetro. Cada nanopartícula de Cobalto se comporta como un monodominio magnético con espín gigante. Su elevada anisotropía le permitiría presentarse, en principio, como un firme candidato a poseer efecto de inversión de la imanación por efecto túnel, al igual que en el $Mn_{12}Ac$. Su importancia radica en el hecho de que se puede variar el entorno de interacción de estas nanopartículas simplemente depositando una capa de metal (por ejemplo cobre) tras el Cobalto, pasando el material magnético de una matriz aislante a conductora. Además, las interacciones dipolares modifican su respuesta magnética permitiéndonos estudiar la competición entre la relajación por anisotropía magnética intrínseca de la nanopartícula y fenómenos colectivos tipo super-vidrio de espín. Muchos de los estudios experimentales se ven dificultados por la falta de control sobre los parámetros de la muestra de estudio, como tamaño de partícula o distribución espacial. Sin embargo, en el caso de estas muestras se pueden estudiar estos efectos de manera cuantitativa y controlada con respecto al número de capas, tamaño de partícula y tipo de medio.

Los nanohilos son materiales con aplicaciones muy variadas, pueden formar parte de dispositivos electrónicos, en almacenamiento magnético e incluso en chips-sensores biológicos. El uso de alúmina porosa como molde, permite preparar por electrodeposición nanohilos de diferentes metales magnéticos con un diámetro comprendido entre 6 y 200 nm y cuya longitud puede llegar a 20 micras. Los hilos son paralelos entre sí y se organizan en una red bidimensional casi ordenada en panal de abeja. En cuanto a las propiedades magnéticas, los nanohilos ya se pueden considerar como un objeto macroscópico, pudiéndose estudiar la dinámica de paredes de dominio en su interior. Cuando el diámetro de un nanohilo de un metal como el Ni es del orden de la anchura de su pared de dominio (45 nm) y, además, mucho más pequeño que su

longitud (del orden de micras) el nanohilo se comporta magnéticamente como un sistema casi unidimensional donde la pared de dominio se propaga a lo largo del hilo. El hecho de que sea un sistema restringido en dos de sus tres dimensiones hace interesante el estudio de como influye dicha constricción de tamaño en sus propiedades magnéticas.

Metodología y principales resultados

1) Estudio magnético mediante susceptibilidad no lineal en moléculas-imán y nanopartículas magnéticas.

Para determinar si existen contribuciones de origen cuántico al comportamiento magnético, así como obtener parámetros que controlan la dinámica del espín como el amortiguamiento o el tiempo de vida medio (tiempo de decoherencia) de los niveles magnéticos excitados, se midió la susceptibilidad no lineal (χ_3). Ésta se determinó mediante un ajuste cuadrático con el campo de la susceptibilidad lineal. A campos distintos de cero se utilizó la técnica inductiva convencional para medir las componentes de la respuesta AC que varían como los armónicos (2ω, 3ω,...) de la frecuencia ω principal. En los estudios sobre Mn_{12} el tiempo de decoherencia de un estado magnético excitado se obtuvo estudiando la variación de $\chi_3(\omega)$ con el ángulo de aplicación del campo, utilizando un portamuestras rotatorio que permitió rotar el eje de anisotropía de las moléculas de Mn_{12} un cierto ángulo con respecto al campo magnético aplicado. Usando la misma técnica de medida de la χ_3 para los clústeres de Co, estudiamos la influencia que sobre la anisotropía y la disipación energética tienen la matriz externa (alúmina, cobre u oro) y el tamaño de partícula.

Los principales resultados obtenidos fueron:

- Se confirma por medidas de susceptibilidad magnética no lineal el mecanismo de inversión de la imanación por efecto túnel en moléculas de Mn_{12}.
- La susceptibilidad magnética no lineal se puede utilizar para estimar constantes de anisotropía incluso en muestras en polvo donde la susceptibilidad lineal pierde esta información.
- Existe una importante contribución de origen cuántico a la susceptibilidad no lineal, siendo la contribución clásica despreciable.

- Es posible la estimación de tiempos de decoherencia a partir de la susceptibilidad magnética no lineal. Así, se ha determinado experimentalmente, por primera vez, un tiempo de decoherencia que resulta ser mucho más corto que el tiempo de vida de un nivel excitado.
- Se confirma, mediante medidas de χ_2 con campo aplicado, los distintos campos de cruce, alrededor de los cuales el mecanismo de inversión de la imanación cambia entre el modo cuántico y clásico. La no linealidad cuántica puede "encenderse" o "apagarse" mediante la aplicación de un campo magnético externo.
- El estudio de la susceptibilidad magnética no lineal sobre monocristales de Mn_{12} benzoato, donde los centros magnéticos de Mn_{12} son en su mayoría de especie "rápida" (menor temperatura de bloqueo) indican un cambio en la anisotropía y en la interacción con el entorno (amortiguamiento) respecto al Mn_{12} acetato con centros magnéticos de especie "lenta". Se pone de manifiesto un comportamiento más cercano al clásico.
- Estudios de susceptibilidad no lineal en condiciones de equilibrio sobre nanopartículas de Co embebidas en alúmina, cobre u oro, ponen de manifiesto el efecto de la matriz sobre la anisotropía de superficie. Podemos observar, así, mediante una magnitud de equilibrio, sin necesidad de estudiar su tiempo de relajación, el aumento de anisotropía debido al recubrimiento metálico de las nanopartículas.
- La susceptibilidad no lineal revela que la dinámica de los espines de nanopartículas de Co está ya en el régimen sobreamortiguado incluso en el caso de matrices de alúmina aislante. Aparentemente, el recubrimiento metálico no cambia apreciablemente el grado de disipación energética de estos momentos magnéticos. El estudio revela una dinámica de espín en régimen sobreamortiguado que se comporta de un modo clásico.

2) Estudio de interacciones dipolares en clústeres de Cobalto.

Las interacciones dipolares dan lugar a propiedades de memoria magnética como el envejecimiento, que hemos estudiado mediante curvas de susceptibilidad tras enfriar la muestra a campo cero (ZFC). Comparamos curvas de susceptibilidad DC obtenidas mediante dos protocolos de enfriamiento distintos. En el primero, la muestra se enfría

directamente a la temperatura en la que aplicamos el campo magnético. En el segundo se lleva a cabo una pausa controlada a una temperatura intermedia, T_{W}, inferior a la de bloqueo. La diferencia de estas dos curvas es una medida del nivel de interacción de las partículas. Para el estudio se varió el diámetro de las partículas, el número de vecinos de coordinación (midiendo muestras con distinto número de capas), temperaturas de espera, tiempos de espera y campos aplicados.

Los principales resultados obtenidos fueron:

- Las interacciones dipolares dan lugar a propiedades de memoria magnética como el "aging" que pueden ser estudiados a través de protocolos ZFC.
- Las correlaciones no aumentan significativamente al aumentar el tamaño del cluster, donde la contribución de las interacciones entre partículas aumentan considerablemente respecto a la anisotropía magnética, sino que están presentes incluso en los clústeres más pequeños, donde las interacciones dipolares son muy pequeñas.
- Se observan fenómenos de "aging" incluso para el caso de muestras con una sola capa. A este respecto, es interesante mencionar que en sistemas 2D no se espera fase de vidrio de espín a ninguna temperatura.
- Las correlaciones permanecen prácticamente contantes al aumentar el número de capas, en relación directa con el número de primeros vecinos, dentro de la cota de error experimental.
- Las correlaciones se suprimen rápidamente por aplicación de un campo magnético externo.
- En la ventana de tiempos que nos es accesible experimentalmente, las correlaciones aumentan aproximadamente de forma logarítmica con el tiempo de espera, como se espera para una red de espines que está alcanzando su configuración de equilibrio.
- Las correlaciones muestran dependencia con la temperatura de espera. El máximo de ΔM aparece a la temperatura de bloqueo para un tiempo experimental igual al tiempo de espera experimental (t_{w}).
- Estos resultados indican que el efecto de "aging" no es unívocamente característico de un comportamiento de vidrio de espín.

3) Síntesis y caracterización de nanohilos magnéticos.

Se instaló en nuestro laboratorio de Zaragoza un dispositivo experimental automatizado para síntesis de nanohilos con baño refrigerado externo. Además se ha elaborado una celda electrolítica isoterma de teflón con capacidad de acción sobre zonas específicas del metal y que permite variar el tamaño de las muestras entre 1 y 15 milímetros.

Los principales resultados obtenidos fueron:

- Controlando diferentes parametros en la síntesis, como el voltaje y el tiempo de anodización o tiempo de deposición, se han sintetizado nanohilos con un buen control de tamaño, longitud y morfología.
- Se investigó la respuesta magnética de nanohilos de Ni en función de su longitud L y diámetro D. Se observa una transición entre el comportamiento magnético característico de una partícula (0D) el de un hilo (1D) cuando la ratio $L/D \simeq 4.6$.
- La histéresis magnética de los nanohilos está determinada por la anisotropía de forma que compite por debajo de la temperatura ambiente con la anisotropía magnetoelástica inducida térmicamente. La compresión debida a los diferentes coeficientes de expansión térmica entre el aluminio y el níquel induce efectos magnetoelásticos que reducen la coercitividad. Este comportamiento se observa sólo si el aluminio sobre el que se asienta la alúmina porosa no es eliminado de la muestra. En efecto, es la contracción del aluminio de soporte la que domina los efectos magnetoelásticos. Esta influencia del aluminio permite explicar la controversia sobre el origen de este efecto magnetostrictivo.
- El efecto de la tensión sobre el campo coercitivo está influenciado por la razón L/D de los hilos, como se observa en la diferente dependencia del campo coercitivo con la temperatura.
- A temperatura ambiente, el campo coercitivo da valores menores que los esperados para el modelo de "rotación al unisono" de Stoner-Wohlfarth. Para diferentes diámetros, se observó que los valores están de acuerdo con modelos de inversión de la imanación por "nucleación y propagación" como el modo "fanning" para diámetros menores que 43 nm (Curiosamente, éste modo no se había tenido en cuenta en la literatura reciente). Para diámetros mayores, el modo

"curling" está cualitativamente de acuerdo con nuestros datos experimentales.

- Por encima de la temperatura ambiente, en un rango de temperaturas no cubierto hasta ahora, la expansión del aluminio produce una tracción que es la responsable de un máximo en el campo coercitivo a temperatura ambiente.
- La variación de la imanación con la temperatura no muestra ninguna evidencia de bloqueo superparamagnético, lo que confiere al material una importante aplicación en dispositivos de memoria magnética.
- La temperatura de Curie decrece progresivamente conforme disminuye el diámetro. De acuerdo con los modelos, esta reducción de la temperatura de Curie es debida a efectos de tamaño finito.
- La temperatura de Curie extrapolada a diámetro infinito muestra una reducción de 3 K con respecto al valor del material masivo. Esto sugiere que las tensiones, cuya presencia e influencia sobre las propiedades magnéticas han sido puestas en evidencia en la histéresis, también modifican T_C. Este efecto no está presente en nanohilos de níquel en matrices de mica, donde las tensiones son muy débiles.

List of articles

- **Nonlinear response of single-molecule nanomagnets: Equilibrum and dynamical**; R. López-Ruiz, F. Luis, V. Gonzalez, A. Millán and J. L. García-Palacios. ***Phys. Rev. B* 72** 224433 (2005).
- **Nonlinear response of single-molecule magnets: Field-tuned quantum-to-classical crossover**; R. López-Ruiz, F. Luis, A. Millán, C. Rillo, D. Zueco and J. L. García-Palacios. ***Phys. Rev. B* 75** 012402 (2007).
- **Magnetic polarization of noble metals by Co nanoparticles in M-capped granular multilayers (M= Cu, Ag and Au): A XMCD study**; J. Bartolomé, L. M. García, F. Bartolomé, F. Luis, R. López-Ruiz, F. Petroff, C. Deranlot, F. Wilhelm, A. Rogalev, P. Bencok, N. B. Brookes, L. Ruiz and J. M. González-Calbet. ***Phys. Rev. B* 77**, 184420 (2008)
- **Classical and quantum non-linear phenomena in molecular magnetic clusters: A review**; F. Luis, R. López-Ruiz, A. Millán and J. L. García-Palacios. ***Comptes Rendus Chimie*** (Invited paper).

Acknowledgements

Obviously, the work described in this book was performed with the implication of many people and institutions:

Fist of all, my doctorate supervisors Fernando Luis and Juan Bartolomé. The financial support from Spanish Science and Education Ministry (MEC) trough the project MAT2002/166 and the European Network MagmaNet. The laboratory facilities of the *Departamento de Física de la Materia Condensada* and the *Instituto de Ciencia de Materiales de Aragón* (CSIC-Universidad de Zaragoza).

Also, the supporting research services of the University of Zaragoza, in particular:

- Servicio de Mecanizado Técnico.
- Servicio de Instrumentación y Medidas Físicas.
- Servicio de Microscopía Electrónica.

The external collaboration of the Trinity College Dublin and the Unité Mixte de Physique (Thales Corp./CNRS/Université Paris Sud XI). Also, the FE-SEM facility from *Serveis Cientificotècnics* (Universitat de Barcelona).

Finally, the personal assistance: María Jose Pastor for electrochemical laboratory work, Jose Luis García-Palacios for theoretical discussions and Fernando López-Tejeira for FORTRAN programming help.

ISBN 978-84-92521-78-4

Prensas Universitarias de Zaragoza